Design of a Battery State Estimator Using a Dual Extended Kalman Filter

by

Michael Wahlstrom

A thesis
presented to the University of Waterloo
in fulfillment of the
thesis requirement for the degree of
Master of Applied Science
in
Mechanical Engineering

Waterloo, Ontario, Canada, 2010

Author’s Declaration

I hereby declare that I am the sole author of this thesis. This is a true copy of the thesis, including any required final revisions, as accepted by my examiners.

I understand that my thesis may be made electronically available to the public.

Abstract

Today's automotive industry is undergoing significant changes in technology due to economic, political and environmental pressures. The shift from conventional internal combustion vehicles to hybrid and plug in hybrid electric vehicles brings with it a new host of technical challenges. As the vehicles become more electrified, and the batteries become larger, there are many difficulties facing the battery integration including both embedded control and supervisory control. A very important aspect of Li-Ion battery integration is the state estimation of the battery. State estimation can include multiple states, however the two most important are the state of charge and state of health of the battery. Determining an accurate state of charge estimation of a battery has been an important part of consumer electronics for years now [1]. In small portable electronics, the state of charge of the battery is used to determine the time remaining on the current battery charge. Although difficult, the estimation is simplified by the relatively low charge and discharge currents (approximately $\pm$ 3C) of the devices and the non-dynamic duty cycle. Hybrid vehicle battery packs can reach much higher charge and discharge currents ($\pm$ 20C) [2]. This higher current combined with a very dynamic duty cycle, large changes in temperature, longer periods without usage and long life requirements make state of charge estimation in Hybrid Electric Vehicles (HEV) much more difficult. There have been a host of methods employed by various previous authors. One of the most important factors in state of charge estimation is having an accurate estimation of the actual capacity (depending on state of health) of the battery at any time [3]. Without having an understanding of the state of health of the battery, the state of charge estimation can vary greatly.

This paper proposes a state of charge and state of health estimation based on a dual Extended Kalman Filter (EKF). Employing an EKF for the state estimation of the battery pack not only allows for enhanced accuracy of the estimation but allows the control engineer to develop vehicle performance criteria based not only on the state of charge estimation, but also the state of health.

Acknowledgments

First I would like to acknowledge Dr Roydon Fraser and Dr Michael Fowler. The dedication to the development of their students is incredible. Their guidance through both my undergraduate and graduate academic careers will undoubtedly be the building blocks for my continued learning in the pursuit of success. The student projects they supervise are the cornerstone to my education and have started me on the path to success. The University of Waterloo Alternative Fuels Team is the reason my passion for engineering exists. The quality of the people I have been able to work with through the team has been incredible. In particular, my good friend Matt Stevens has always encouraged me and motivated me to push further and persevere when it seemed difficult to do so. Other teammates that have greatly impacted my learning include Dan Sellan, Chris Mendes, Erik Wilhelm, Chris Lawrence, Jen Bauman and Chris Haliburton. I would also like to thank Dr Steven Waslander for his contribution and review of my research.

I'd also like to thank my family for their support over my university career. My sister and parents have provided me extensive support throughout.

Finally I'd like to thank Kim for her support during my graduate career. Her encouragement has never wavered despite all the late nights and sacrificed weekends.

Dedication

I dedicate this work to Kim who makes all this work worthwhile.

Table of Contents

List of Figures

List of Tables

1 Introduction

There are environmental, political and automotive market forces that are leading to a much greater electrification of passenger cars in today's society. Coupled with some recent developments in high power, high energy automotive battery systems, automotive manufacturers have begun extensive development of testing of highly electrified cars [4]. There are no more prevalent examples than the soon to be released Chevrolet Volt extended range electric vehicle and the Nissan Leaf full function electric vehicle. Both vehicles use a version of Lithium Ion battery technology to power its wheels for the majority of the vehicle's operational time.

Hybrid electric vehicles have already made their way into the market. Specifically the Toyota Prius, Honda Insight and General Motors 2-Mode Hybrid vehicles have been on the market for years now. These vehicles all utilize Nickel Metal Hydride (NiMH) batteries as on-board electrical energy storage. Furthering the step toward electrification, newer vehicles will begin to utilize electricity from the common electrical grid to displace petroleum in an attempt to increase efficiency and lower the demand on petroleum energy [5]. These Plug-in Hybrid Electric Vehicles (PHEV) will be utilized in both a blended manner and an all electric manner, depending on the intent and cost. Lithium Ion batteries have been considered the main contender for use in PHEVs [6].

Now that PHEVs have become an inevitable part of the automotive landscape in the nearer term, battery technology has become increasingly important. For years now consumer electronics have been utilizing some form of Lithium Ion battery technology, allowing electronics manufacturers to downsize batteries for energy and increase available power. The benefits of Lithium Ion batteries are that they have the potential for higher specific energy and energy density as well as higher power density and specific power [7].

One of the disadvantages of lithium ion batteries is the cost of materials and manufacturing [8]. Therefore, battery lifetime becomes increasingly important. Targets for OEMs are in the

300,000 cycle range for HEVs [9]. Current targets show lithium ion battery systems costing between $200 and $700 per kWh [10,11]. As a vehicle's battery energy utilization increases, the battery lifetime is decreased depending highly on the battery's Depth of Discharge (DOD). It's of paramount importance to manufacturers that the amount of electrical energy storage on board be weighed with the benefit to longer charge depleting range. It is important to understand the advantages and disadvantages of battery utilization in the vehicle in order to make educated decisions regarding vehicle operation.

1.1.1 Project Objective

This project's objective is to generate a battery state estimator for the University of Waterloo's battery test station. The work focuses on the specifics of the battery and chemistry that are currently utilized by the University of Waterloo, and discusses extensions and tuning capabilities for other chemistries.

The battery test station has been used recently for lifetime testing of $LiFePO_4$ battery cells. Prior to the completion of this research, the test stand cycle testing has been limited to constant current cycles based on voltage limits and not on State of Charge (SOC). The goal of this project is to enable real time estimation of SOC and battery capacity to enable further lifetime testing of battery cells based on real world scenarios and drive cycles.

This thesis will explore some of the pressures that are forcing Original Equipment Manufacturers (OEMs) to increase the depth of discharge of battery packs at the expense of the battery's life that is requiring accurate battery state estimation. Accurate battery state estimation will reduce the required battery pack capacity and increase the ability to adjust to changing battery characteristics.

The Battery State Estimator has three main goals:

Provide Accurate SOC estimation over a degradation cycle
Be simple enough for future students to understand the philosophy and theory
Provide an estimation of the error of the SOC

The estimator was rigorously tested with both real data and simulation showing good accuracy and precision. Several SOC algorithms were developed in Simulink and tested against each other as well as two capacity estimation algorithms. The most accurate algorithm was chosen.

2 Background

2.1.1 Vehicle Technologies and Fuel Consumption

Electrification of the automobile continues to bring with it a new powertrain design space for engineers. With the increased level of system integration the combinations of possible energy optimization techniques seems endless. In order to understand the optimization landscape, the efficiency of the vehicle must be split into the vehicle itself and the drive cycle of operation. First, the drive cycles that the vehicles will be tested upon will be reviewed and then some possible methods to improve a conventional vehicles powertrain will be discussed.

2.1.2 Drive Cycles

Since so much of the vehicle force requirement (and therefore energy) is driven by the vehicle speed, it is important to consider the vehicle drive cycle when discussing the effects on fuel consumption. It is clear that drive cycles that have lower speeds will require less energy to overcome aerodynamic drag as the road load on a vehicle is proportional to the speed squared. However, drive cycles with lower speed will also have more dynamic behaviour, leading to more changes in vehicle speed and increasing the acceleration changes needed to achieve the cycle. The tradeoff of these is the purpose for testing vehicles on both a city or urban cycle and a highway cycle. The United States Environmental Protection Agency (EPA) regulates every vehicles urban and highway fuel economy over various drive cycles, the two most famous being the Urban Dynamometer Drive Schedule (UDDS) and Highway Fuel Economy Test (HWFET). Figure 1 shows the Federal Test Procedure (FTP) which is a UDDS followed by the first 505 seconds of the UDDS repeated. From these two tests, the EPA determines the vehicles sticker fuel economy. There is also a combined fuel economy that comes from a weighted average of 55% urban and 45% highway fuel economy.

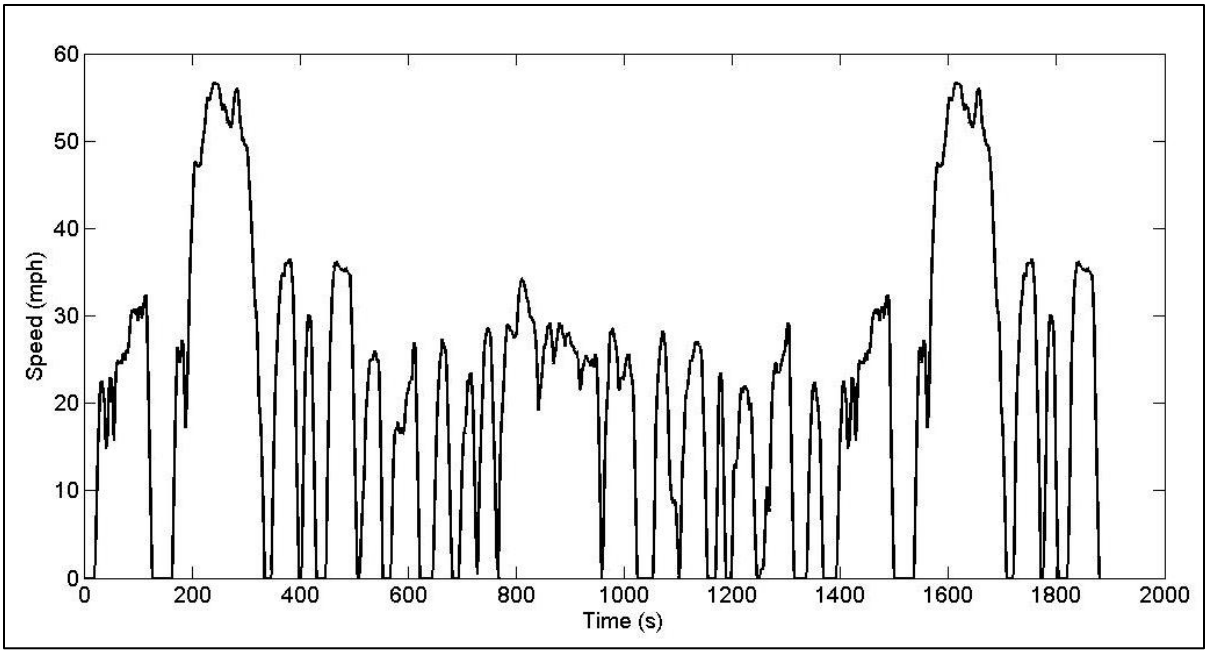

Figure 1: Federal Test Procedure Speed Trace [12]

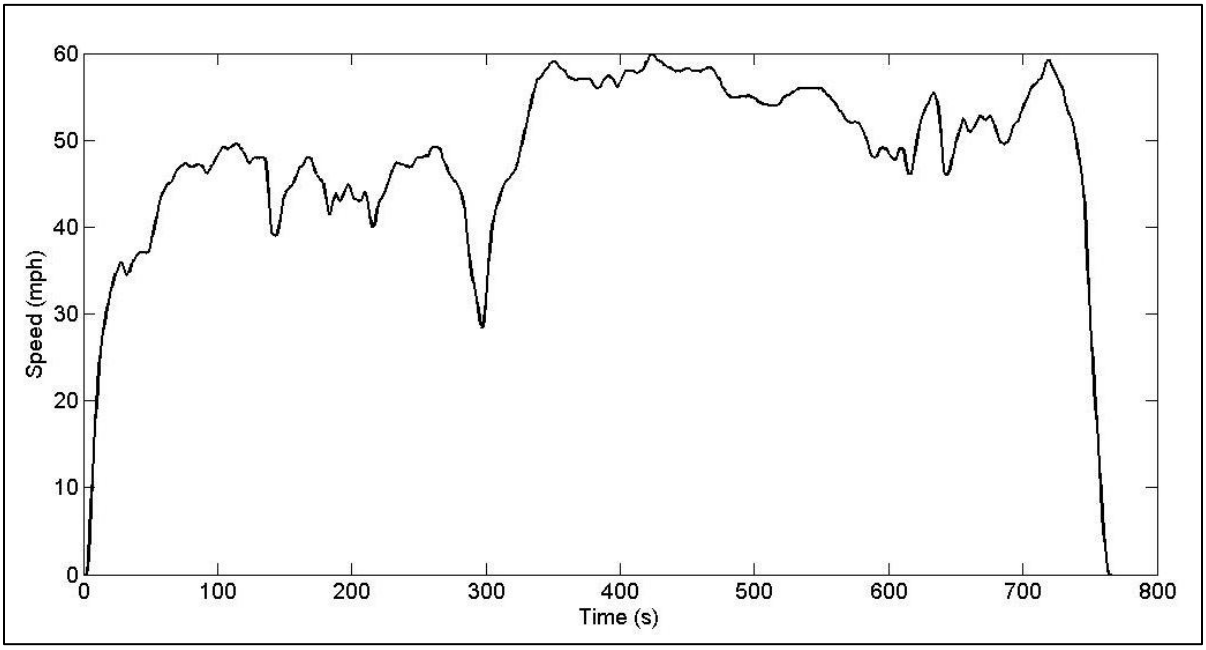

Figure 2: Highway Federal Emission Test Speed Trace [12**]**

As can be seen from the figures, the FTP has much lower speeds, leading to a much lower effect to overcome aerodynamic drag, but much more speed dynamics leading to more required

energy to overcome inertial forces. The HWFET has a lot fewer speed dynamics; however a lot of energy is required to overcome the aerodynamic drag.

Figure 3 shows a plot of amount of time at each acceleration and speed on the FTP (cruising neglected to show a reasonable scale). Theoretically, any drive cycle that matches this exact surface should give the same fuel economy results for conventional vehicles. Acceleration at a certain speed is tied directly back to engine loading in a conventional vehicle, assuming a static transmission shift schedule.

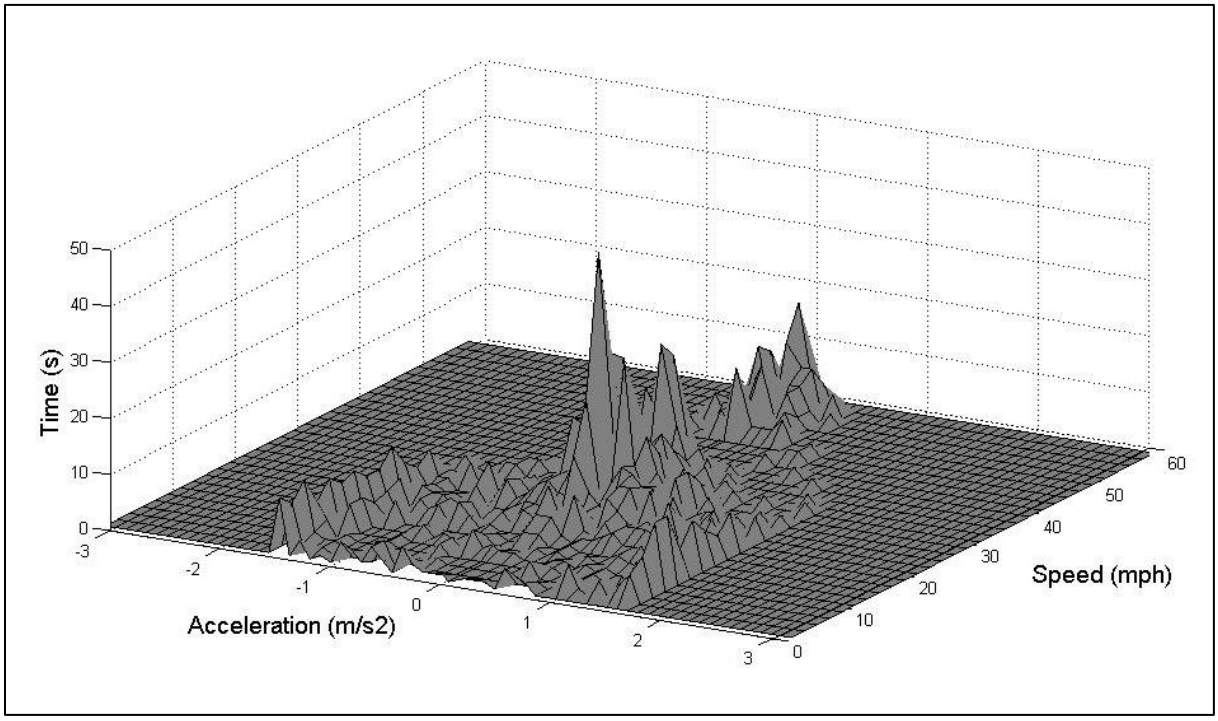

Figure 3: FTP Speed, Acceleration, Time Surface

Drive cycle parameterization has been a topic of concern for years now. The FTP was developed in the early 1970s to simulate combined city and highway driving in Los Angeles [13]. The top speed of the FTP is 57 mph and the maximum acceleration is 3.3 mph per second. Both the top speed characteristic and the maximum acceleration were set due to the

limitations of dynamometers at the time [13]. To date there has been no accepted, systematic characterization of drive cycles for either criteria tailpipe emissions or fuel efficiency despite numerous attempts [14].

El-Shawarby [15] utilized a method of splitting the drive cycle into vehicle cruise speed and acceleration, analyzing the affects of each constituent. Holmen extended this philosophy and analyzed the proportion of the drive cycles high cruise, low cruise, medium cruise, acceleration, deceleration, and idle [16]. Ericsson developed a system of determining a fuel consumption factor based on the street's function, type of environment (neighborhood, highway, etc), speed limit, density of traffic lights, traffic-calming measures, and traffic flow [17]. The analysis deconstructed the drive cycle and summed the fuel consumption factor for each segment. Later, Brundell-Freji and Ericsson expanded on the same concept expanding to seventeen parameters [18]. Fuzzy logic has also been used to create drive cycle parameters Langari for use in hybrid vehicle control strategies [19].

2.1.3 Vehicle Road Load

Based on the drive cycle chosen, the road load of a vehicle quantifies the forces required to propel the vehicle down the road and are shown in the following free body diagram:

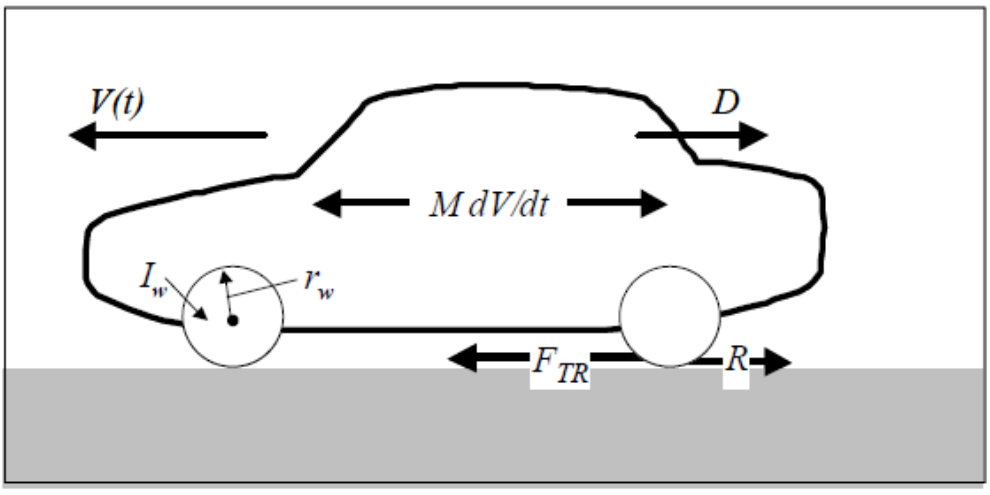

Figure 4: Vehicle Forces Free Body Diagram [20]

The road load is broken up into four main parts including the aerodynamic drag, the rolling resistance, the inertial vehicle force and the rotational force required to spin the tires. For the purposes of this analysis, the rotational forces are neglected in order to simplify the scenario. Essentially the road load equation is as follows:

$$F_{TR} = R + D + F_{inertial} \quad \text{equation 1}$$

where:

R is the force due to rolling resistance

D is the force due to aerodynamic drag

$F_{inertial}$ is the force due to acceleration of the vehicle

The rolling resistance is a function of the vehicle mass and tire resistance as in equation 2.

$$R = r_0 Mg \quad \text{equation 2}$$

where:

r_0 is the coefficient of rolling resistance for the tire

M is the vehicle mass

g is acceleration due to gravity

It is important to note that the vehicle speed does not have an effect on the rolling resistance of the vehicle. Aerodynamic drag, however, is dependent on vehicle speed squared as can be seen in equation 3.

$$D = C_D A \frac{V^2 \rho}{2}$$ equation 3

where:

C_d is the coefficient of drag

A is the effective frontal area of the vehicle

V is the vehicle speed

ρ is the air density

The Inertial force is simply the force required to accelerate or decelerate the vehicle (with rotational forces neglected) based on the vehicle mass and current speed as shown in equation 4.

$$F_{inertial} = M\left(\frac{dV}{dt}\right)$$ equation 4

Therefore, the forces due to rolling resistance and aerodynamic drag are never negative, however the intertial forces can be either negative or positive.

2.1.4 Powertrain Losses

The rest of the fuel consumption equation for a vehicle come from inefficiencies of turning the liquid fuel into the forces required to propel the vehicle. In general, the major inefficiency comes from the primary fuel converter, typically a gasoline engine. A gasoline engine efficiency is generally accepted to be approximately 30% on average, however is highly variable based upon engine loading and engine speed as shown in Figure 5.

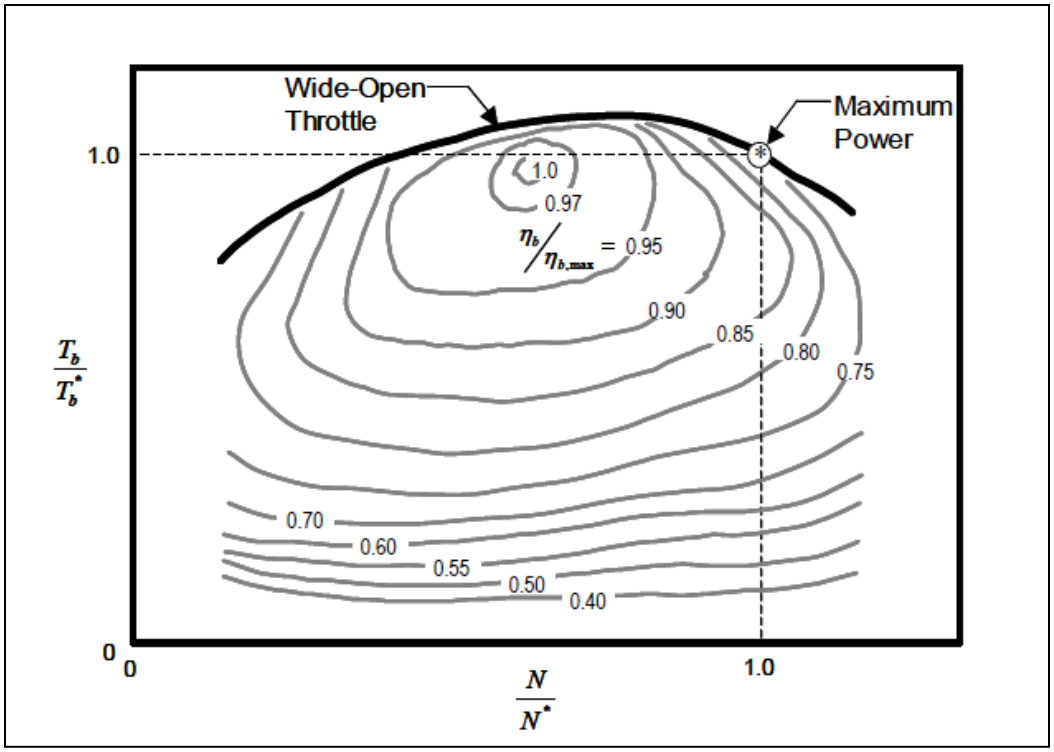

Figure 5: Representative Operating Map for Contemporary Gas Engines [21]

Engine efficiencies can vary based upon fuel selection and combustion strategy (ie. Diesel, compression ignition or gasoline/ethanol spark ignition), however the above graph is a typical pattern for most engines.

The other losses in a vehicle come from drivetrain losses and parasitic losses. Drivetrain losses are relatively similar for most vehicles as are parasitic losses, depending on things such as air conditioning and are less powertrain dependent.

2.1.5 Hybrid Electric Vehicles

2.1.5.1 Hybrid Electric Vehicle Philosophy

Hybrid electric vehicles take advantage of three main theories:

- The energy converted to heat during braking (when $F_{inertial} < 0$) can be captured and stored on-board the vehicle.
- The supplemental power capability of an electric motor can enable the primary energy converter to operate in more efficient areas of the efficiency map
- Downsizing of the main energy converter can take place since the motor can provide supplemental power to meet the demands of the drive cycle[22].

Essentially, hybrid vehicles recover energy utilizing regenerative braking; a technique in which an electric motor is used as a generator to slow the vehicle and convert the mechanical energy of the vehicle into electrical energy. Then, when excess power is required to propel the vehicle, the electric motor utilizes energy from the battery to provide torque to the wheels.

2.1.5.1.1 Series Hybrid Electric Vehicles

A series vehicle is an HEV that utilizes a primary fuel converter to charge a battery that powers an electric motor. Figure 6 shows the power flow of a series hybrid electric vehicle.

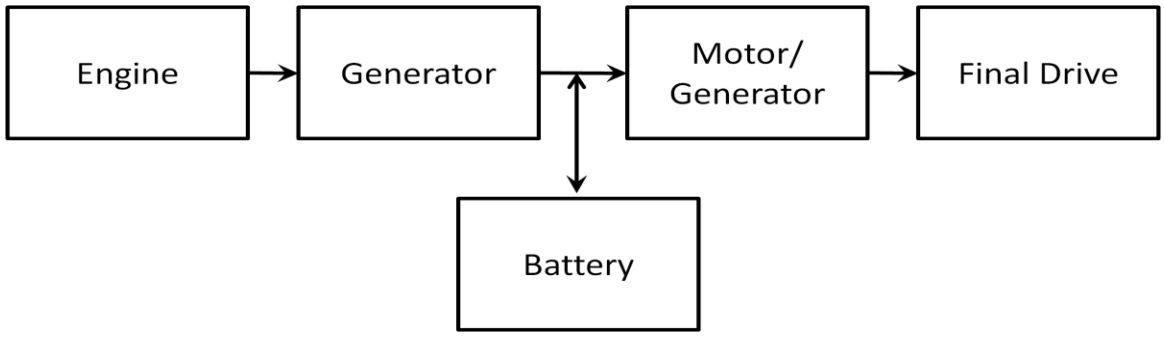

Figure 6: Series HEV Architecture

The main advantage of a series hybrid vehicle is the ability to run the primary energy converter at a very constant rate. The main disadvantage of a series hybrid vehicle is that the motor must

be powerful enough to meet the entire power demand of the drive cycle. As one would expect, as motor power increases, so does cost.

2.1.5.1.2 Parallel Hybrid Electric Vehicles

Parallel HEVs have the ability to power the wheels with either the engine or motor or both. Although they come in different configurations (Parallel through the road, pre-transmission parallel, post-transmission parallel), a lot of the benefit remains the same. Figure 7 shows the power flow of a parallel HEV.

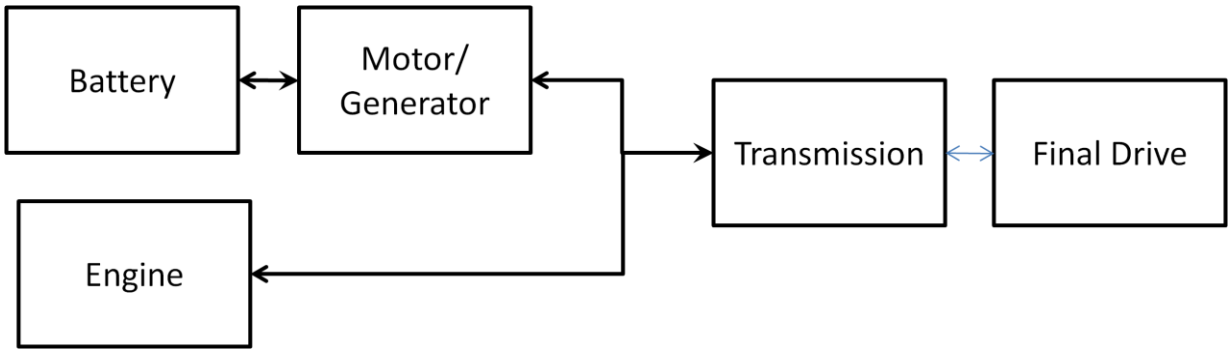

Figure 7: Parallel HEV Architecture

The advantage of a parallel HEV is that the either the motor or engine can provide power to the wheels, depending on which will give the vehicle the most efficient power moding. It gives the control engineer more degrees of freedom for optimization of the hybrid control strategy. Also, the motor and engine can both be relatively small since peak power can come from a combination of the two, rather than a single source. The downside of the parallel is that often the electric only operation of the motor is limited due to power limitations.

2.1.5.1.3 Powersplit Hybrid Electric Vehicles

Powersplit vehicles are vehicles that can operate in a series mode or parallel mode depending on the hybrid control strategy. They are very advantages in that they can operate as an electrically variable transmission giving the vehicle the ability to operate at nearly any speed ratio through the transmission [23]. The main disadvantage of powersplit vehicles is the cost and packaging room required. However, Toyota's Prius has been able to package the one-mode transmission and market it for a reasonable cost. Recently General Motor's 2-Mode transmission has integrated a more complex system into the size of a standard automatic transmission. The 1-Mode and the 2-Mode have different advantages, the main disadvantage between the two being cost.

1 Mode (Input Split)

The 1 mode system is utilized by Toyota and Ford in their hybrid vehicles. This is the most common hybrid transmission on the market. The philosophy of the transmission is that the engine is operated at an efficient point on the map, the power is transmitted to the final drive through the planetary gearset. Any additional power, unneeded for vehicle propulsion is used by the first motor/generator to charge the battery or power the second motor/generator. It should be noted that there will be one point when the speed of the engine is equal to the speed of the output shaft times the planetary gear reduction. This is called the transmissions "mechanical point" [23] and is the fundamental difference between the 1-mode and 2-mode transmission. Operating at the mechanical point is very efficient since none of the power needs to be converted to electricity and back into mechanical power.

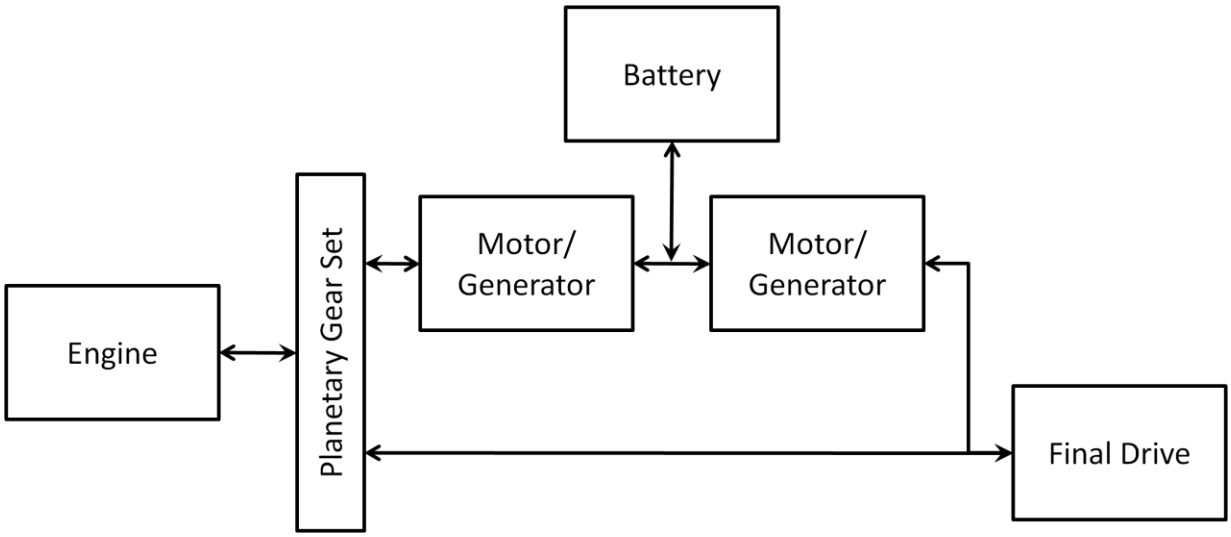

Figure 8: 1-Mode Powerspilt Architecture

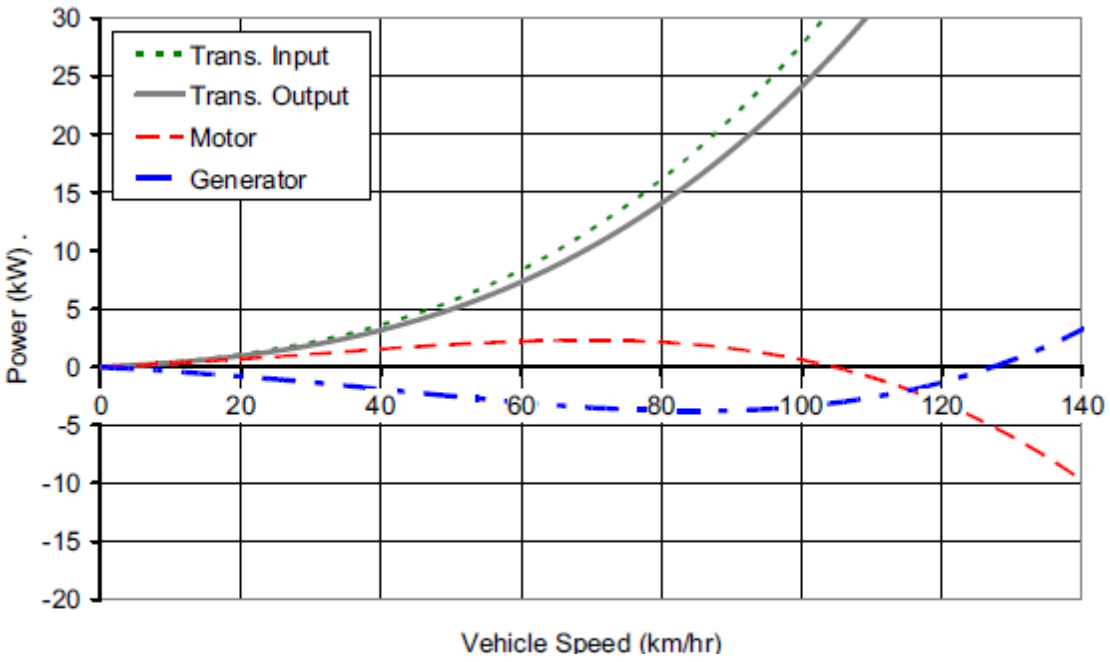

Figure 9: 1-Mode EVT Light Power Chart [23]

2-Mode (Compound Split)

The compound split transmission employs two planetary gearsets, on the output of the engine and the input to the final drive. The advantage of this transmission is that it can operate as a 1-

mode input split transmission or a compound split transmission. This gives the 2-Mode three distinct mechanical points [23].

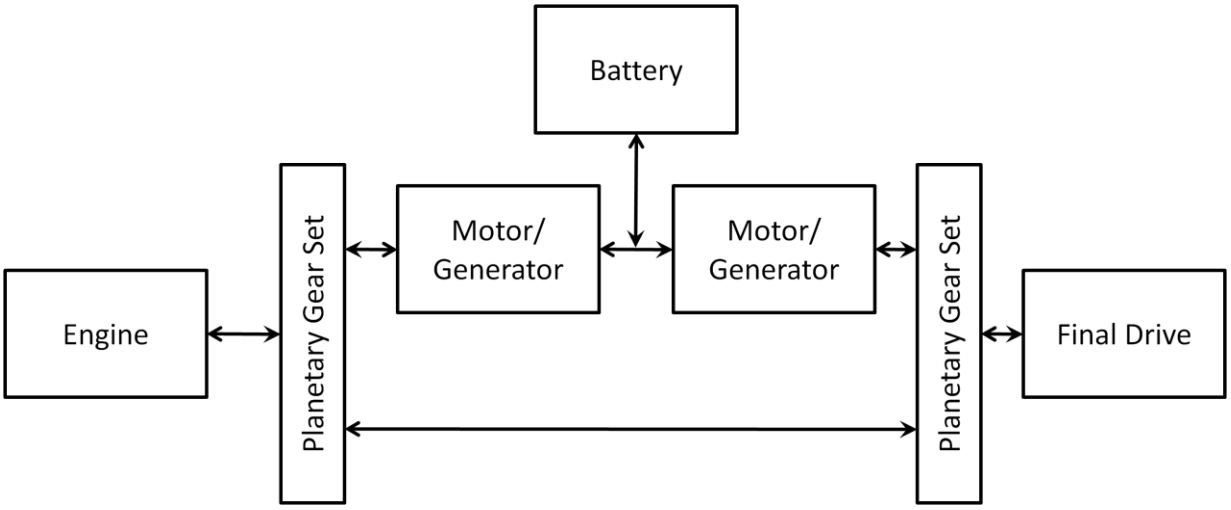

Figure 10: 2-Mode Powersplit Architecture

Figure 10 shows the light power chart of a 2-Mode vehicle and how it has two EVT modes based on the states of the two planetary gearsets.

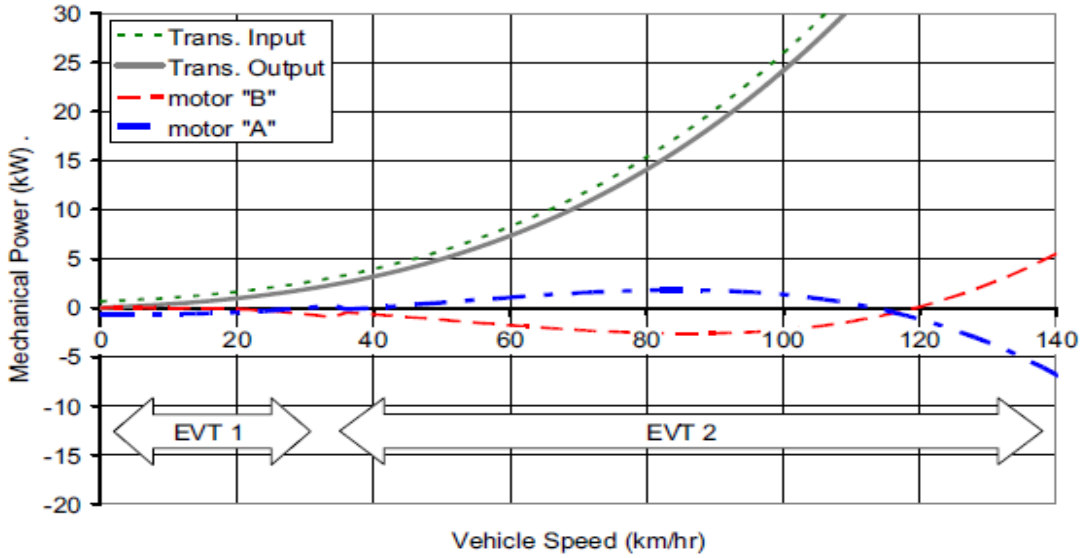

Figure 11: 2-Mode EVT Light Power Chart [23]

2.1.6 Plug-In Hybrid Electric Vehicles (PHEV)

PHEVs are vehicles that utilize energy from the electricity grid to propel the vehicle and can also operate like a hybrid vehicle once the vehicle battery is depleted. There are various levels of PHEVs differentiated by charge depleting operation strategy and charge depleting range. For example, a vehicle may drive all electrically for the charge depleting portion of the vehicle operation and then switch to charge sustaining mode. An example of the SOC tracked over the drive cycle is shown in Figure 12.

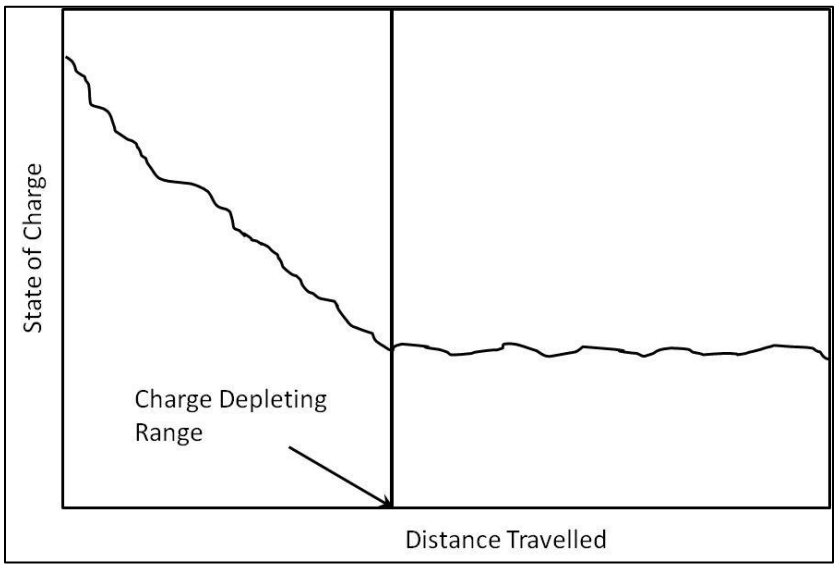

Figure 12: All Electric Charge Depleting Range

A different vehicle may continually blend electrical and fuel energy while charge depleting prior to charge sustaining mode in order to extend the charge depleting range of the vehicle. An example of a blended vehicle showing how SOC tracks as a function of distance travelled on a certain drive cycle is shown in Figure 13.

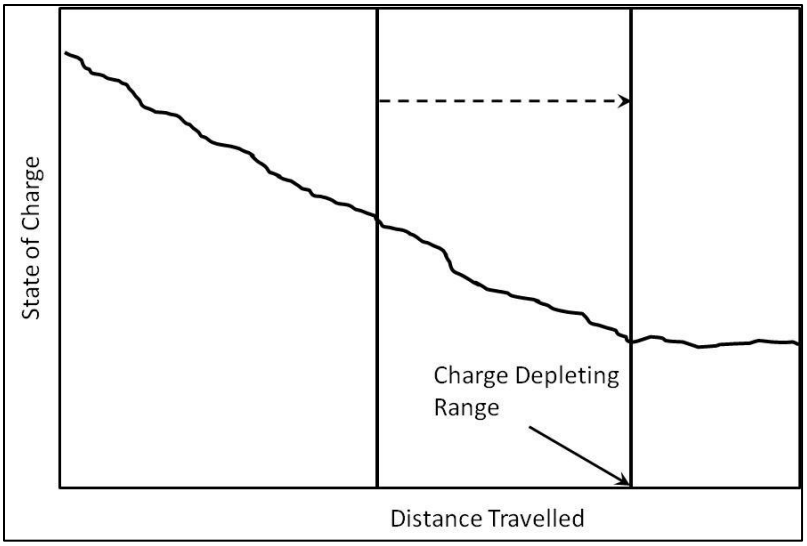

Figure 13: Blended Charge Depleting Range

The question that a manufacturer needs to answer is what the optimal charge depleting range for a specific vehicle is.

2.1.7 Extended Range Electric Vehicles (EREV)

An EREV is a version of a PHEV that can operate all-electrically over a specific drive cycle [24]. The EREV must be able to meet the power demands of the drive schedule with its electrical powertrain, much like a series vehicle, however does not necessarily need to be a series vehicle. The Chevrolet Volt is the only example of an EREV being developed by an OEM.

2.2 Fuel Efficiency Considerations

The fuel consumption characteristics of a vehicle have become an increasingly important topic over recent years due to the increased focus on the environment, specifically, global climate change. A reduction in fuel consumed is generally tied to a reduction in greenhouse gas emissions, for conventional gasoline vehicles and also a reduction in petroleum usage. It is

important to understand the constraints on reducing fuel consumption in vehicles prior to understanding the benefits of electrified vehicles.

2.2.1 Fuel Consumption Considerations for HEVs

Hybrid vehicles present unique challenges for fuel consumption certification compared to conventional vehicles. The biggest differentiator is that a hybrid vehicle is more time or sequence dependent than a conventional vehicle since the battery's state of charge (SOC) can vary in the duration of a drive. For example during a trip starting with high SOC, the vehicle first drives on electricity and does not require any engine use. At some point the SOC drops and the engine kicks on. After returning home and the HEVs SOC has likely dropped during the drive. The next trip may be identical however it starts with a lower SOC. During the first drive, some fuel energy was replaced with electrical energy. However, during the second drive the fuel was used to recharge your battery instead of propelling the vehicle. In short, the first drive yielded significantly better fuel economy than the second. This is unique to hybrids over conventional vehicles.

Theoretically, identical trips should yield identical fuel economy in a conventional vehicle. This range of operation makes it difficult to determine what the average vehicle would do when sold to the fleet of Americans with just one test. Therefore, the fuel economy is corrected based on the electrical energy used and an estimated efficiency of what it takes for the vehicle to recharge itself.

2.2.2 Fuel Consumption Considerations for Charge Depleting Vehicles

PHEVs and EREVs continue to complicate things. The core obstacle is their two discrete modes of operation. The first mode is referred to as charge depleting, which is when the battery is being depleted to propel the vehicle, and the second mode is when the vehicle is charge sustaining, like a regular hybrid. Depending on how long it has been since the vehicle has been charged, the vehicle may either be in charge depleting or charge sustaining mode. At the end of the day, we want to determine what the fleet of vehicles will do in the hands of the

public so we take new things into consideration, like the range that the vehicle can deplete for and the length of any driver's trip, not just the type of driving they are doing. The process to determine fuel consumption for charge depleting vehicles has been proposed by the Society of Automotive Engineers (SAE) J1711 standard [25]. The philosophy of the standard is outlined below.

The National Household Transportation Survey (NHTS) is periodically taken in the U.S., which tracks many things including how many highway miles and how many city miles each vehicle travels in a day. This information helps determine how a vehicle would be operated by the fleet, so the next step is to calculate the percentage of the more than 3 million daily miles travelled would be travelled in each mode. This ratio is called the Fleet's Utility Factor and by using it the fuel consumption during charge depleting can be weighted with the fuel consumed while charge sustaining. Mathematically, it breaks down as follows:

$$FC = UF \times FC_D + (1 - UF)FC_S \qquad \text{equation 5}$$

where:

UF is utility factor

FC_D is charge depleting fuel consumption

FC_S is charge sustaining fuel consumption

This is what the average fuel consumption will be among the public. Note that the above equation is using fuel consumption, not fuel economy. Fuel economy is defined as the distance you can travel for a fixed volume of fuel (e.g. miles per gallon). Fuel consumption is the amount of fuel it takes to go a fixed distance (e.g. liters per 100 kilometers). The main reason fuel consumption is used here is because the vehicle may run 100% electric during the charge depleting range. Therefore, zero liters of fuel are consumed. Inversely, during charge depleting range, drivers do not use any fuel and are still going places, so they travel an infinite number of miles per gallon used. Anything added to infinity is still infinity, so your fuel economy would be infinite if calculated that way. Certification tests are also computed using fuel consumption

and then converted for the American public. Since the upcoming certification tests are likely to be based on J1711, the vehicle manufacturer's charge depleting strategy is of upmost importance.

The vehicle manufacturer's decision on charge depleting strategy is mainly based on a three factors:

- Cost to manufacture the vehicle
- Consumer Appeal
- Corporate Average Fuel Economy (CAFE)

Of utmost importance is CAFE. In the United States every manufacturer must conform to CAFE, which is a law upheld by the National Highway Traffic Safety Administration (NHTSA) under the Department of Transportation (DOT). CAFE is important because it is a driver for what kind of vehicles a manufacturer can sell. CAFE is the regulation that has the intention of improving fuel economy, on average, across the US. Vehicles are tested on the UDDS and HWFET and their fuel economy is certified by the EPA. The average fuel economy of the manufacturer must be above the CAFE required fuel economy or the manufacturer is fined.

Currently, vehicles are tested based on the results from the UDDS and HWFET. However, PHEVs must be tested differently. Basically, when testing a conventional vehicle, the important drive cycle characteristics are accelerations at speed. These points in general tie back directly to engine loading points on the efficiency map. Theoretically, a completely new drive cycle could be constructed of the same accelerations at speed and the fuel consumption results should be very close. When HEVs are tested, the order of these points makes a big difference based on the battery's SOC at the time. When considering PHEVs it makes an even bigger difference because it is dependent on whether the vehicle is charge depleting or charge sustaining. Therefore a new test method had to be developed to certify vehicles that need to be considered under CAFE. At the time of this writing, the EPA had not finalized the test

specifics to be utilized for charge depleting vehicles. However, SAE J1711 offers some insights into what may be enacted.

To adequately evaluate the fleet average fuel consumption and electrical energy usage of charge depleting hybrids, the utility factor method is used. The following UF equation is taken from J1711. UF results are valid from 0-400 miles and were found using a modified least squares approach which ensures the fits are monotonic and minimize the relative errors in the fit to the raw data. The allowable error was made to be less than 0.5%, providing a UF certainty with rounding errors within 0.01 throughout the equation range (the normalized distance).

$$UF = 1 - \exp\{-[C1 * (x/\text{norm\_dist}) + C2 * (x/\text{norm\_dist})^2 + \ldots + C6 * (x/\text{norm\_dist})^6]\} \quad \text{equation 6}$$

Table 1: 2001 NHTS Utility Factor Equation Terms [26]

Term	Fleet UF
norm_dist	399.9
C1	10.52
C2	-7.282
C3	-26.37
C4	79.08
C5	-77.36
C6	26.07

It should be noted that this Utility Factor is for a combined city and highway driving cycle.

The final utility factor curve up to 400 miles is shown in Figure 14.

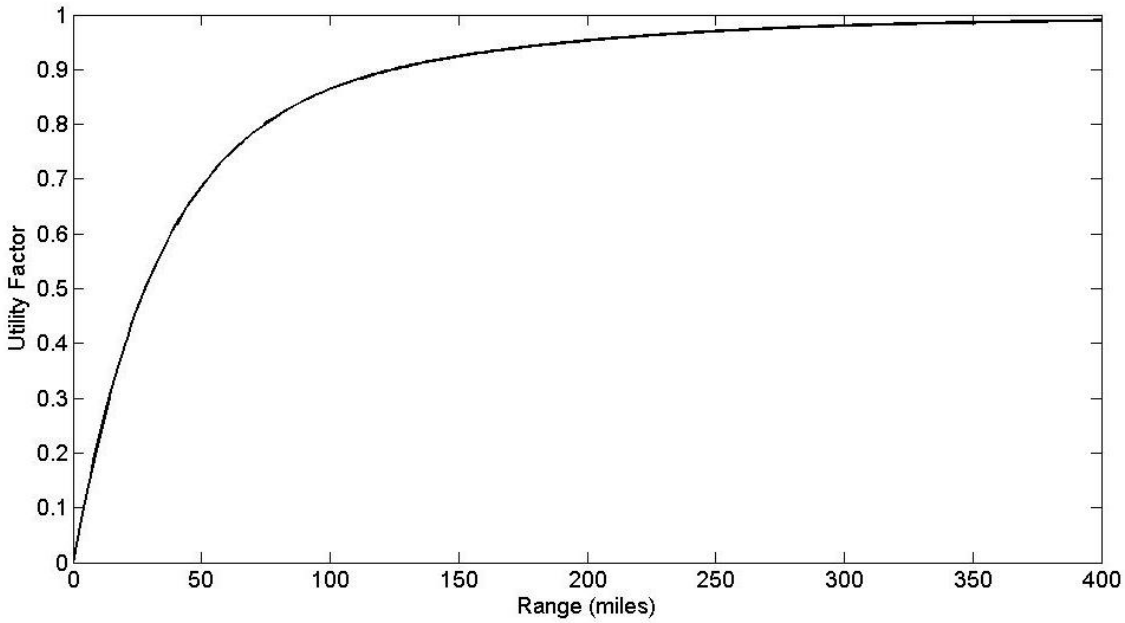

Figure 14: Fleet Utility Factor Curve

2.2.3 Optimizing Fuel Economy Based on J1711

The reason it is important for OEMs to understand J1711 is because the manufacturer will want to maximize a PHEVs impact on CAFE. As CAFE regulations are increasing, the manufacturer must respond. Therefore, an analysis on the optimum fuel economy per vehicle will be carried out by the manufacturers and a similar analysis is carried out here.

The first thing to consider is that every hybrid vehicle has an operating efficiency line for a drive cycle due to road load and powertrain efficiencies. An example efficiency line is presented in Figure 15.

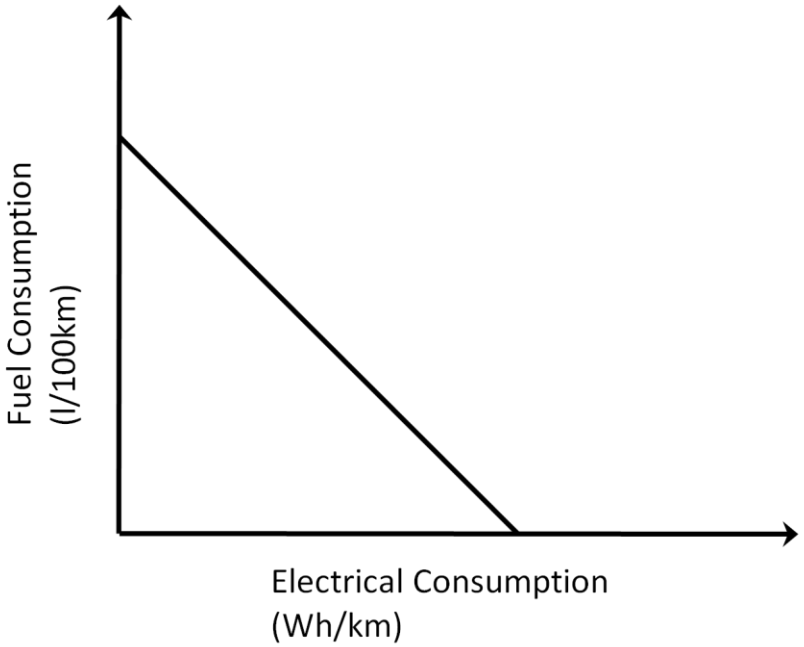

Figure 15: PHEV Efficiency Curve

During charge depleting the vehicle will operate with some net electrical consumption. If the vehicle is operating all electrically, the results of that particular drive cycle will be at the intersection of the x-axis. Once charge sustaining, the vehicle will operate at the intersection of the y-axis. All blended operation will happen somewhere along the line depending on the blending strategy (neglecting cold start effects). At a minimum, as cycles are repeated, each vehicle will have at least one point on the line that is the transition cycle between charge depleting and charge sustaining.

The vehicle efficiency can be altered by two factors other than the drive cycle that it was tested on. The first factor is the vehicle road load. The road load of the vehicle will affect how far the curve is away from the origin, but will not affect the slope of the line itself, as shown in Figure 16.

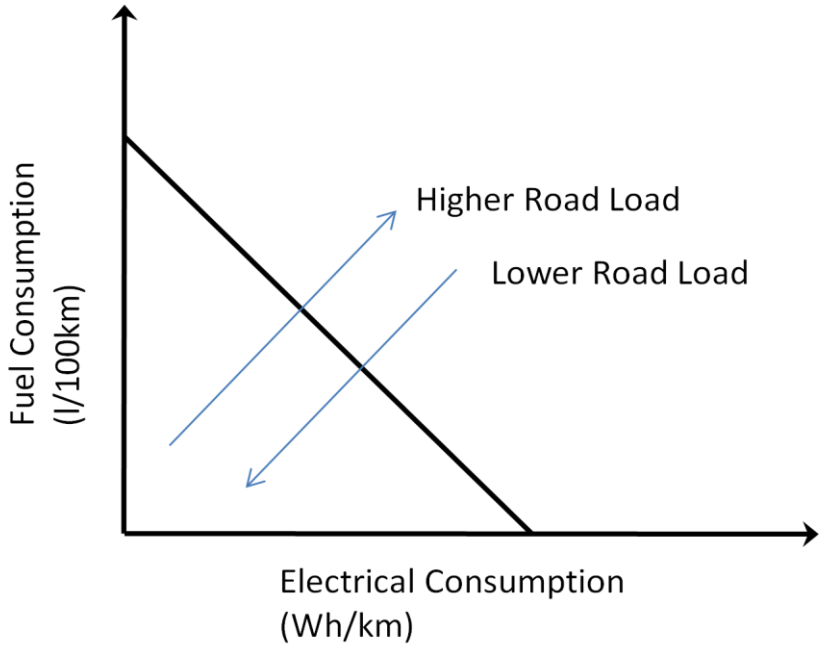

Figure 16: PHEV Efficiency Curve Road Load Factors

The slope of the curve can only be changed by changing efficiency of the fuelled powertrain (engine/transmission) relative to the electrical powertrain. For example a diesel engine will likely be more efficient than a spark ignite engine, causing the y-intercept to move down the y-axis.

In order to maximize the fuel economy of a certain vehicle, the control strategy can be tuned to utilize more or less of the battery pack. The more the vehicle utilizes, the lower the fuel economy of the vehicle will be, since it will directly be replacing fuel that would have been used. Mathematically, the intent is to minimize the utility factor weighted fuel consumption. Therefore, taking the derivative of equation 5 gives:

$$\frac{dFC}{dCD_R} = \frac{dFC_D}{dCD_R} + \frac{dUF}{dCD_R}(FC_D - FC_S) = 0 \; for \; minimum \qquad \text{equation 7}$$

where CD_R is charge depleting range

Charge depleting range is merely a function of the charge depleting fuel consumption and the battery energy available. Energy available is a function of the battery energy stored on-board and the desired depth of discharge the OEM decides to utilize. The intent is to determine what depth of discharge and charge depleting fuel consumption will yield the smallest net fuel consumption rating. Assuming a constant battery capacity and a constant charge sustaining fuel consumption, an example of the resulting surface is shown in Figure 17.

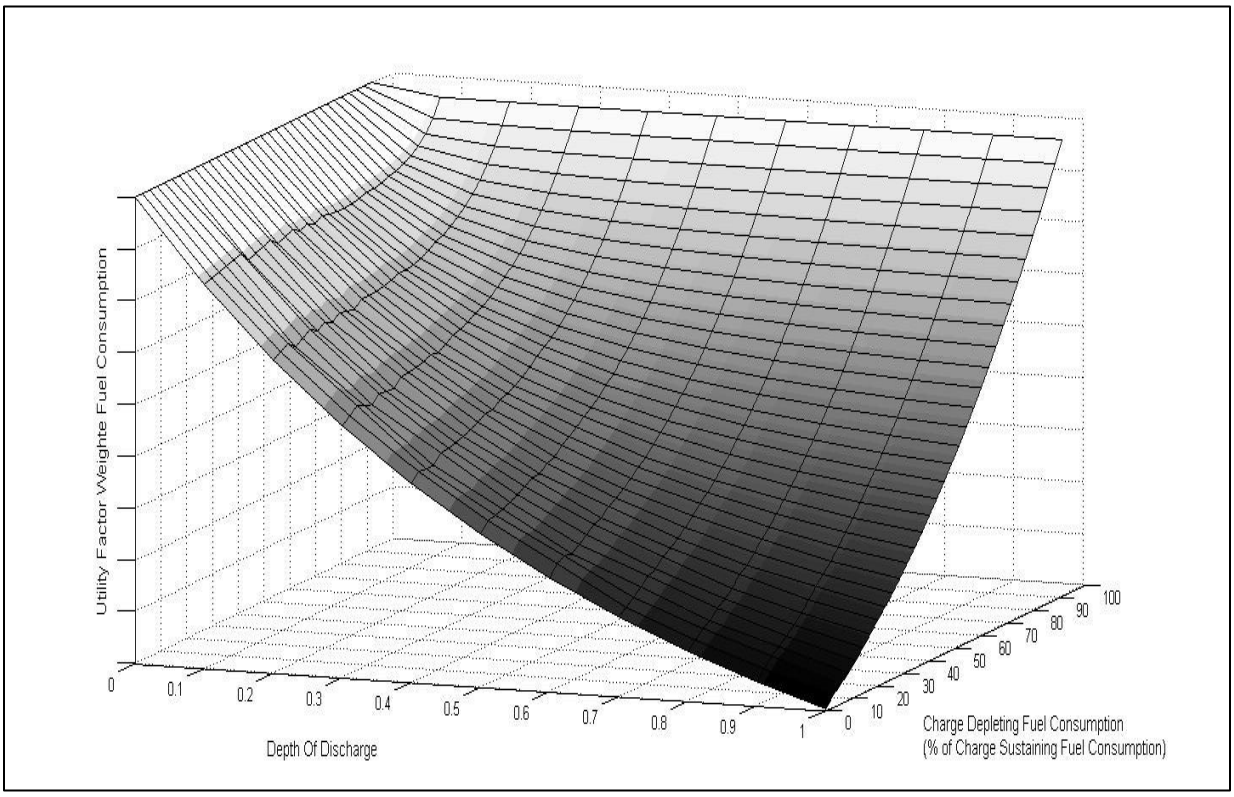

Figure 17: Utility Factor Weighted Fuel Economy Optimization Surface

Clearly, from Figure 17 it is obvious that the most beneficial fuel consumption metric would be at the point of 100% depth of discharge (DOD) and 0 charge sustaining fuel consumption. There is a possibility that the same fuel consumption will be realized by utilizing some fuel consumption and increasing the depth of discharge. For example, there is a possibility that 50% DOD and 0 charge sustaining fuel consumption could give the same net fuel consumption as

100% DOD and 2.4 l/100km, depending on the efficiency curve of the vehicle. In this case, a manufacturer will likely utilize the reduced depth of discharge and run all-electrically to begin, since the reduction in DOD will yield longer battery life and shorter charge times for the consumer. The decision for the OEM then becomes mainly based on the lifetime of the battery pack, to receive the best possible fuel consumption rating.

2.2.4 Battery Technology

2.2.5 Battery Materials

There are several battery chemistries that have been investigated for use in HEVs and PHEVs. Historically lead acid batteries have been used due to their inherent robustness, high power density, ease of manufacturing and relatively low cost. However, their low specific energy, low energy density and short cycle life have lead to their ultimate demise for use in higher energy applications.

2.2.5.1 Ni Cd

Nickel cadmium batteries were briefly investigated due to their improved specific energy and energy density over lead acid batteries. Ultimately there were several reasons why NiCd batteries are not utilized in HEV or PHEV applications. Specifically, the memory effect was the biggest reason. Essentially the NiCd memory effect is a phenomenon where the battery capacity is artificially reduced due to a change in the crystalline structure of the battery creating large crystals as opposed to the desired small crystals [27]. The memory effect along with the dangers associated with cadmium and only a marginal improvement in specific energy and energy density make NiCd impractical for the applications in HEVs and PHEVs [10].

2.2.5.2 NiMH

Nickel Metal Hydride batteries are currently the most prevalent battery in HEVs. Their improved specific energy and relatively high energy density make them a more attractive option than either Pb-Acid or NiCd. In hybrid applications, their low manufacturing cost, high

level of safety and high power density make them a plausible chemistry [28]. Appearing in most of today's hybrids including the Toyota Prius, the Ford Escape and Fusion, and the General Motors 2Mode Hybrids they are clearly the current choice of the industry for hybrid applications. Where NiMH batteries weaknesses come in to play is in charge depleting applications such as PHEVs and EREVs. In these applications, NiMH cycle life is a serious detriment. The mechanism of degradation in the NiMH cell is mainly the corrosion of the MH particles during the absorption and release of hydrogen atoms [29, 30]. Finally, SOC determination is difficult in NiMH packs due to a flat Open Circuit Voltage (OCV) curve and a large hysteresis voltage [31].

2.2.5.3 Li Ion

Often Lithium Ion batteries are grouped into one big group; however, it is important when reviewing chemistries to investigate the pros and cons of each lithium ion chemistry. Although there are several common characteristics, they vary greatly on issues of safety, specific energy, energy density and cycle life. The most common characteristic is the intercalation of lithium in a carbon based anode material. Also, the electrolyte material is most commonly lithium hexaphosphoflourate ($LiPF_6$) combined with a cyclic alkyl carbonate and a linear alkyl carbonate [32]. A common separator is a polypropylene and/or polyethylene membrane structure. The most common difference is the cathode chemistry makeup. The cathode material is the most influential part of the battery when it comes to the characteristics of the cell. Since the energy capacity of the battery is limited to the capacity of the cathode, the material is extremely important [7]. Also the cathode composition typically dictates the cycle life and abuse tolerance of the cell. Until the last few decades, Lithium batteries had not been practical despite the fact that lithium is the lightest and most electronegative metal. It is reactivity with water as well as the reactivity with common solvents in battery electrolytes made lithium batteries prohibitively unsafe. The realization that the lithium intercalates with carbon based anodes was one major breakthrough. The other breakthrough is the development of the solid-electrolyte interface (SEI) that forms on the anode the first time the battery is charged.

Finally, another main advantage of Lithium based batteries is the higher voltage. Typical Lithium-Ion cells with a graphitic anode have a nominal voltage of about 3.7 V, three times that of NiMH cells (1.2 V) [7]. This higher voltage has many inherent advantages. The first advantage is that a higher cell voltage leads to fewer batteries in series in order to get the voltage up to the potential operating voltages of the rest of a vehicle powertrain. Battery pack designers can now integrate shorter strings of cells in parallel which each share the current load of the system. This sharing leads to lower currents in each cell and the battery pack is not nearly as power limited. Also, the higher voltage can be a major advantage to power converters on the vehicle. Power converter sizing and mass increases with current commands, therefore having a higher voltage reduces the size of all of the power electronics on the vehicles high voltage bus. These advantages have already been realized in consumer electronics.

Figure 18 is a Ragone Plot showing the benefits of Lithium Ion batteries over other chemistries.

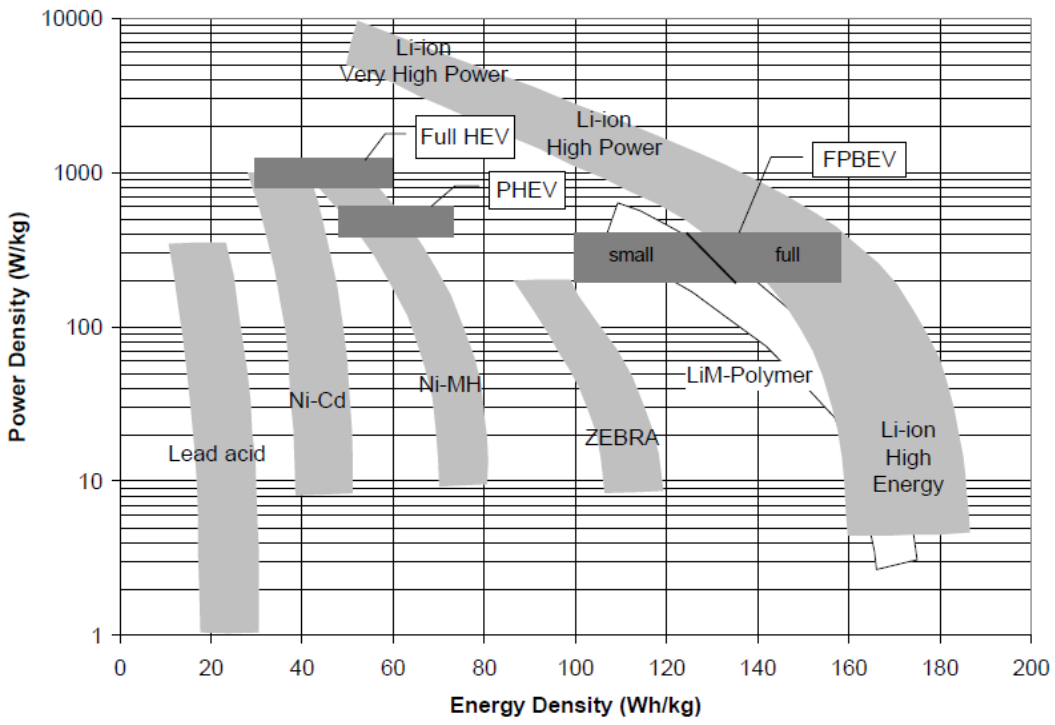

Figure 18: Ragonne Plot [22]

2.2.5.4 Lithium Ion Mechanisms

In the early 1970's research began to show the ability to place an electrochemically active species into an electrically conductive host. The process, known as intercalation, is practical assuming the conductive host structure does not change as lithium is added and removed, which leads to the reversibility of the reaction. The intercalation process is very important on both the anode and cathode side. The anode is typically a graphitic carbon; however more research has been done recently with lithium titanate oxides, the benefits of which will be discussed later. The cathode material has received the most attention of late. There are essentially two groups of cathode materials available today:

Layered compounds

In the layered compounds, the structure is an anion close-packed lattice in which layers alternate between basically empty layers and redox-active transition metals. Lithium intercalates between the metal layers.

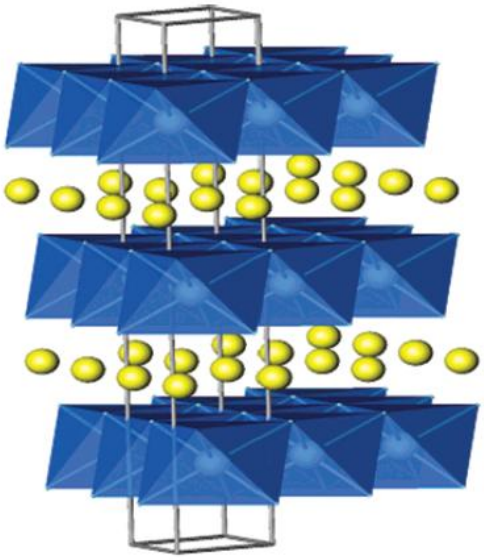

Figure 19: Layered Electrode Structure [33]

Open structures

The second group has more open structures that, when properly ordered, create tunnels between the transition metals. The lithium inserts itself into the tunnels.

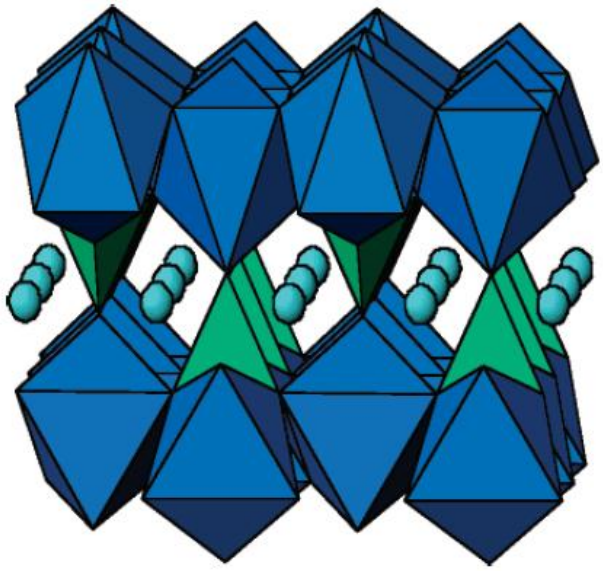

Figure 20: Open Electrode Structure [33]

The layered cathode has an inherently higher volumetric energy density since it is able to pack more lithium per unit volume. The second group has the potential to be much lower cost materials and could possibly have a power density advantage depending on the material.

No matter which group the cathode is part of, it is desirable for the material to have a high free energy of reaction when combined with the lithium. The higher the free energy, the higher the voltage of the cell (up to approximately 4 V before it is limited by the stability of the electrolyte) which benefits the battery once arranged in a battery pack as described earlier.

2.2.5.5 Lithiated Cobalt - $LiCoO_2$

Lithiated cobalt oxide cells are the main cells utilized in consumer electronics. First introduced in 1991 by Sony, they are the first lithium ion cells developed with the graphitic anode material, replacing the metallic Li anode and providing a safer lithium cell structure. $LiCoO_2$ is a layered anion lattice structure that is highly conductive which benefits both the energy and

power capabilities on a volume basis. A $LiCoO_2$ cathode has decent storage capacity of lithium ions with adequate chemical stability. The main problems with this cathode are the expense of cobalt ($30-$40/kg) and the safety issues associated with tolerating over charge and internal shorting leading to fires. $LiCoO_2$ cells are still widely used in consumer electronics that have very predictive and constant charge and discharge characteristics, but their safety and expense issues make them impractical for automotive use.

2.2.5.6 Lithium Manganese Spinel - LMS

Lithium manganese spinel (LiMn2O4) addresses the cost issue of the $LiCoO_2$ cells by replacing with the manganese crystalline structure. This structure is also much safer due to the crystalline structure and requires very little excess lithium for full charge. The lower energy capacity of the LMS over the $LiCoO_2$ is countered by the higher specific power. Although initially thought to have a low calendar life, some literature indicates that new additives have helped in this area. Finally, the LMS battery has good low temperature power capabilities which have been making it a major choice for some automotive manufacturers. LMS is currently offered by the LG Chem / Compact Power packs and is being used in the Chevrolet Volt program.

2.2.5.7 Li NCA

This cathode material Li(Ni0.85Co0.1Al0.05)2, approaches the benefits of the LiCoO2 cell, however reduces the cost due to the reduced concentration of cobalt. NCA cells tend to have significant cycle life issues that are currently under development for improvement [34]. However, the same safety issues are present and therefore must be very well controlled. Currently Johnson Control Systems (JCS) and GAIA (a division of Lithium Technology) are exploring its use in automotive applications.

2.2.5.8 Li NCM

This cathode material (eg. Li(Ni1/3Co1/3Mn1/3)O2) has similar characteristics to NCA however is less expensive. A main advantage is that it can be manufactured to be charged to two different voltages (either 4.1V or 4.7V). Voltages up to 5 V have been observed, however, capacity fade becomes a major factor at the higher voltage. Although other cells have shown the potential to be charged to various voltages, the NCM cathode material has stable products at full discharge for these voltages. The two voltages lead to a high power variant and a high energy variant of the cell. Mainly manufactured by Kokam and Lamillion, this cathode has shown recent promise for use in automotive applications, due to its relatively good safety on overcharge. Li NCM cathodes can have other formulae and concentrations of Ni Co or Mn, but this "333" compound appears to be the compound most under consideration. Cost is a major drawback for this chemistry, despite the fact that it is lower cost than NCA, as well as uncertainty of cycle life based on various sources.

2.2.5.9 $LiFePO_4$ Lithium Iron Phosphate

This cathode material has been very attractive of late. Initially thought that the Fe would block Lithium sites in the cathode intercalaction tunnels [33], A123's nano architected materials have improved conductivity in the cathode, increasing power capability. The inherent stability during charge and discharge make the cell very safe and highly tolerant to abuse. Of upmost interest is the possible change of structure when the orthorhombic LiFePO4 phase changes to a more quartz like tetrahedral FePO4 during charge. Although the FePO4 tetrahedral structure can lead to a safe over charge condition since it is electrochemically inactive, it also leads to irreversible capacity fade. The FePO4 can have either a tetrahedral or orthorhombic structure depending on synthesis and temperature. On discharge, the LiFePO4 shows great thermal stability increasing the ability to safely charge the battery to 100% state of charge. Since the tunnel structure of the LiFePO4 is inherently of lower volumetric density that the close-pack anion structures, the ability to utilize 100% of the lithium on discharge is attractive to decrease

the volume for the same cylcable lithium. Another safety benefit of the tunnel based structure is that there is no loss of oxygen during charge like there can be during the charge of the layered anions in the other chemistries. The trade-off between the safe over discharge and lower cycle life are a main consideration during LiFePO4 batteries. The thermal stability of LiFePO4 is very high which also protects the cells during over discharge. Of note, other metals with a higher potential compared to pure lithium have been investigated (specifically LiMnPO4) but do not have the benefits of tolerance abuse and low cost observed with the LiFePO4 cathodes.

2.2.6 Battery Degradation Mechanisms

The SEI limits the reactivity of the lithium with the organic electrolyte, however it lets lithium ions pass through during charge/discharge cycling. Limiting the reactivity made lithium batteries able to be utilized in consumer applications, increasing the safety by decreasing the dendritic nature of lithium. However, the safety comes at a cost; as the cell is cycled, the SEI layer builds up and cracks and more lithium is used to fill in the cracks. This building of the SEI layer leads to an increase in resistance of the cell [35], resulting in power fade, and a decrease in cyclable lithium, resulting in capacity fade. To compensate for the initial building of the SEI, the cathode is manufactured with an excess of lithium. Another major mechanism of degradation is characterized by a fracturing of intercalation sites due to stresses on the lattice during charging to high SOCs, resulting in a loss of activation sites leading to capacity and power fade [36].

In general, the initial capacity fade is attributed to the loss of cyclable lithium due to SEI film growth predominantly on the anode, although the cathode has a relatively thin build up of SEI as well [37]. As the cell ages a bigger factor than SEI growth becomes the fracturing of the intercalation sites on the anode [38]. Jin reported that the change in degradation mechanisms occurs around 200 cycles [39]. In general it is quite difficult to model the degradation mechanisms in Li-Ion cells. Ning presented a 1-D model of degradation methods and Tang expanded it to a 2-D model to understand the deposition of lithium during charge[40,41]. Both

models require extensive time and computing power for simulation and neither are good applicants for real time determination of battery capacity.

Although cycling is the main degradation mechanism, many papers also correlate battery degradation directly to temperature as well [42, 43]. Battery capacity will also be function of temperature as shown in the figure below. The capacity varies because at colder temperatures the low voltage point will be reached more quickly than at warmer temperatures as shown in Figure 22: Capacity as a Function of Temperature Due to Changes in Reaching Max and Min Voltages

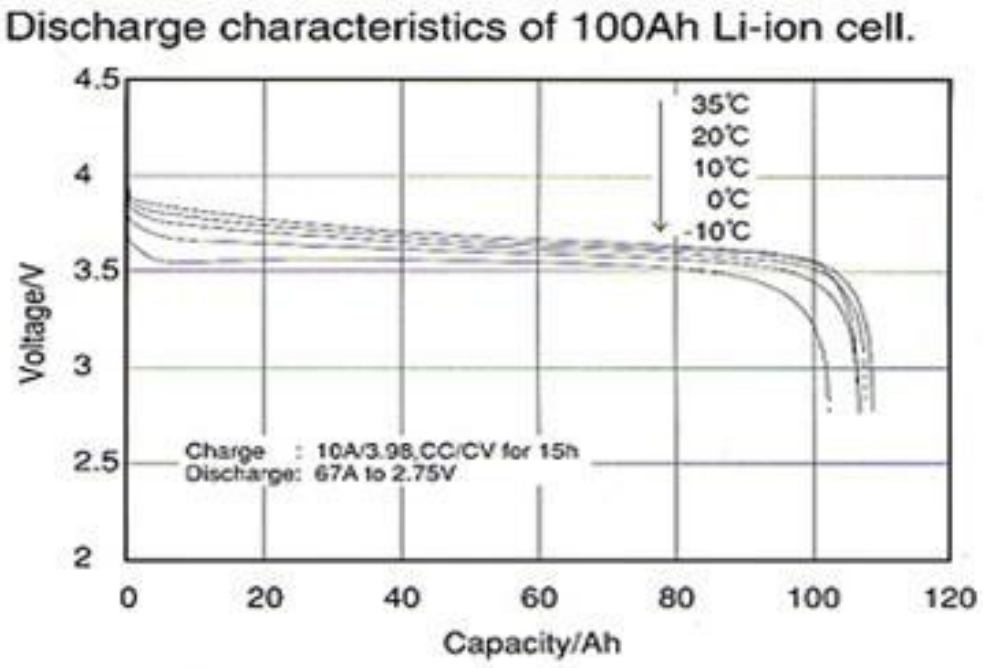

Figure 21: Capacity as a Function of Temperature [27]

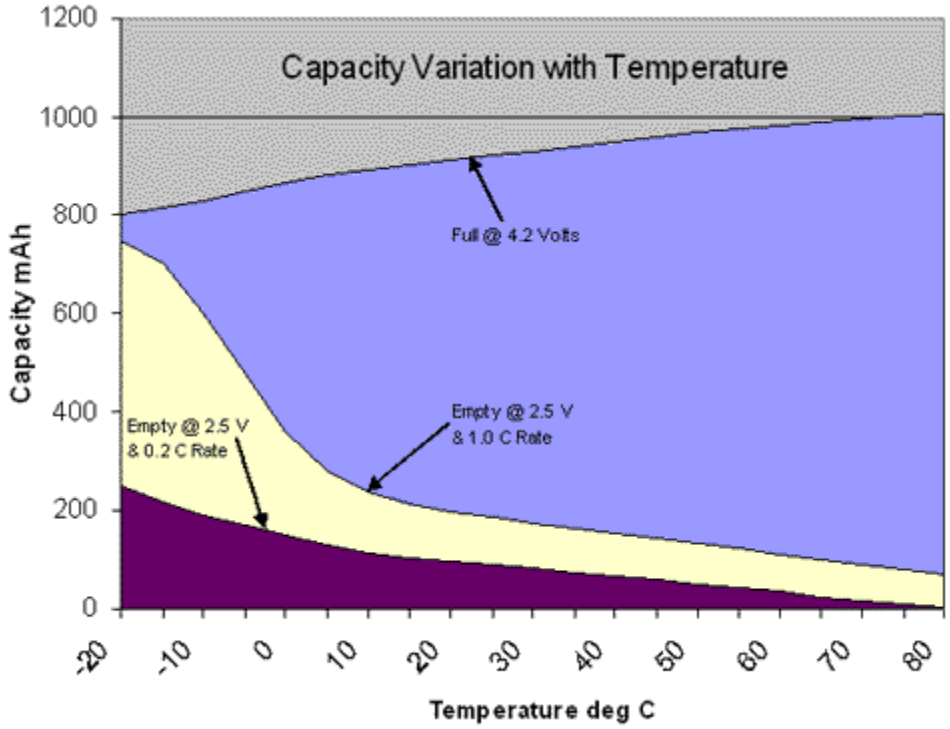

Figure 22: Capacity as a Function of Temperature Due to Changes in Reaching Max and Min Voltages [27]

2.2.7 Designing for End of Life

In order to design and size the battery properly for automotive applications, OEMs use a process called "Backward Facing Component Sizing." This method predicts what the battery capacity will be at End of Life (EOL) and estimates what the capacity must be at the Beginning of Life (BOL) to meet that metric. Figure 23 demonstrates the Backward Facing strategy.

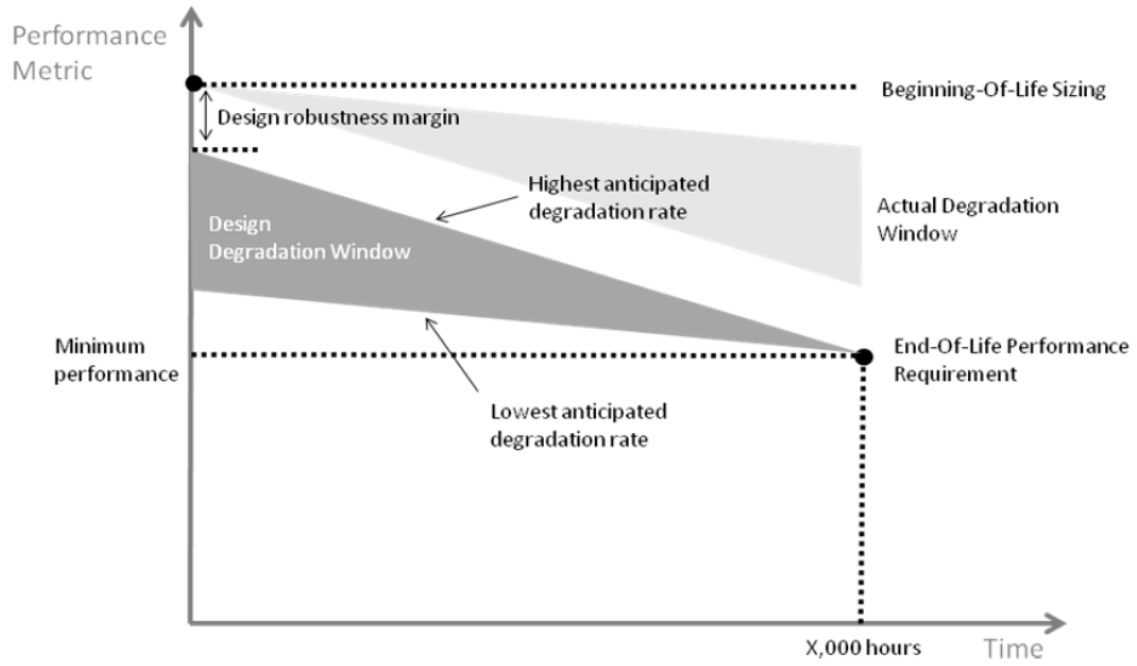

Figure 23: Backward Facing Component Sizing [44]

2.2.8 Hybrid Powertrain Degradation Test Stand

How vehicle control algorithms affect battery degradation is not generally understood. Therefore, the University of Waterloo utilizes a Hybrid Powertrain Degradation Test Stand to better understand the interactions. The goal of the stand is to cycle advanced hybrid components and log their characteristics as they degrade. It provides a means of testing components and control strategies on a bench scale. This makes testing more efficient, cheaper, and much safer for researchers.

The test stand is scaled-down version of a real hybrid fuel cell powertrain. It contains all of the components of a real vehicle, including a hydrogen fuel cell, battery, DC/DC converter, regenerative source (for simulating regenerative braking), and a load box to simulate an electric motor. It also uses a controller that reads a drive cycle and then directs each of the components accordingly. Each of the components can be easily removed and replaced by a

different model, in order that researchers can efficiently test different components. For example, the batteries currently on the APTS can be removed and replaced by a different type. Furthermore, the controller is programmable so that researchers can test a variety of hybrid control strategies.

The test stand architecture is shown in Figure 24. The test stand is a tool that researchers and graduate students at the University of Waterloo can use to safely and efficiently investigate hybrid fuel cell vehicles on a bench scale. With component 'plug and play' and an easily programmable controller, researchers can test a wide range of configurations and hybrid control strategies.

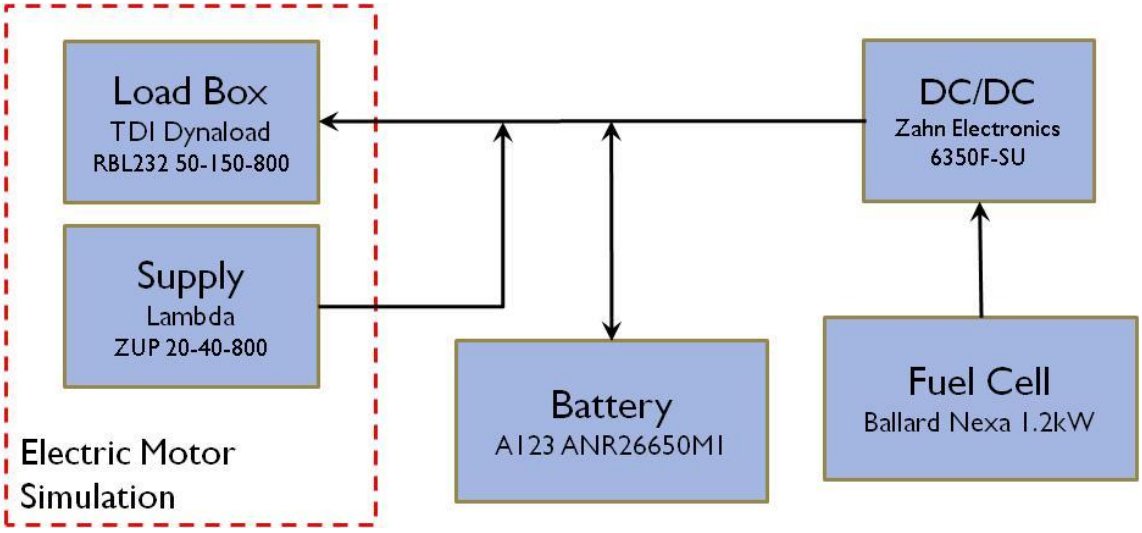

Figure 24: Battery Test Stand Architecture

DC/DC Converter:

The DC/DC converter used on the test stand is a Zahn Electronics model DC6350F-SU. Its purpose it to convert the fuel cell voltage to match the battery voltage. The controller sends a signal to the DC/DC converter, indicating the desired output voltage, so that it matches that of the battery.

Battery:

The second power source of a hybrid fuel cell is a rechargeable battery. The batteries chosen for the test stand were lithium ion batteries produced by A123. These batteries were obtained from A123 Systems at no charge to the design group. They were selected based on availability and relevance to the current industry. Each battery cell has 3.3V nominal and a maximum continuous current of 60A (although they can supply up to 120A for peak current for 10 seconds).

Regenerative Source:

A Lambda ZUP 20-40-800 model AC/DC power source was integrated. This AC/DC power source plugs into the wall and uses the inlet AC current to produce a DC current output.

Its purpose is to mimic the regenerative braking in a real hybrid fuel cell vehicle. In a real vehicle, the electric motor is used for braking. This model was selected based on its compatibility with the recharge requirements of the A123 lithium ion batteries.

Load Box:

The load box on the test stand is a TDI Dynaload RBL232 50-150-800. Its purpose is to mimic the load of the electric motor in the hybrid vehicle.

2.3 SOC Estimation Methods

Recently, there have been many papers written on determining state of charge of Li-Ion batteries for vehicle applications. SOC has become a critical control metric in hybrid vehicle control and therefore accurate estimates of SOC are extremely important [45, 46, 47]. Also, there have been many techniques utilized for SOC estimation on both a cell and pack level. It is extremely important to note the difference between cell level and pack level state of charge for a couple of reasons:

SOC for a battery pack is limited by the lowest capacity cell in the pack. Due to cycle life differences and manufacturing tolerances, cells can be utilized slightly differently in the pack relative to their own capacity. The cell with the smallest capacity dictates the capacity of the entire series string of batteries. Therefore, for system utilization, it is extremely important for the cells to be balanced properly, and manufactured at extremely tight tolerances. Cell balancing is typically accomplished with printed boards that distribute small amounts of current from one cell to another based on a voltage reading with millivolt resolution. Also of importance in this respect is the cooling system design. As stated, temperature swings can cause fracturing of the SEI layer which will eventually cause a loss of cyclable lithium and an increased resistance. If the cooling strategy allows for "hotspots" in the pack, some cells will degrade earlier than others, causing those cells to limit the other cell's ability to fully cycle. It is outside the scope of the research to develop adequate balancing techniques and hardware.

Determining SOC on a single cell, the system is typically setup to monitor one cell, with one current sensor and one voltage sensor. As the cells are developed into a battery pack, the ability to monitor each cell to that level is limited, specifically in current sensing. Generally battery packs are limited to one current sensor and precision of the current sensors are generally limited by cost both on a sensor level and a control input level. For example, a highly precise current sensor is wasted if the controller input has a low bit resolution. A typical automotive embedded controller has 10-bit resolution

on its analog to digital converter. A 10 bit resolution on a system that cycles between -360A and 360 A, would have a reading resolution of approximately 0.7 A. As the bit resolution increases, so does the cost of the controller. Both current shunts and Hall Effect sensors have been used in the past (current shunts much more widely). Generally, the embedded controller must have at least 12-bit resolution (+/- 0.17 A in the previous example), which creates a very expensive addition to the battery's embedded controller and still barely provides adequate resolution to do adequate state estimation on a single cell. A main point of the work on SOC estimation in this research deals with a noisy, imprecise current and voltage measurement.

The main techniques utilized in past works have been:

OCV estimation
Coulomb counting
Electro-Impedance Spectroscopy (EIS)
State Estimation Using Filters

2.3.1 Open Circuit Voltage Estimation

OCV estimation has been utilized extensively as an estimation technique for SOC. It relies on the basic principle that with no load applied to a battery, voltage and SOC are related based on a predictable relationship [48]. This relationship is highly dependent on the battery's chemistry. It is also dependent on two other parameters; temperature, and more importantly state of health as can be seen in Figure 25.

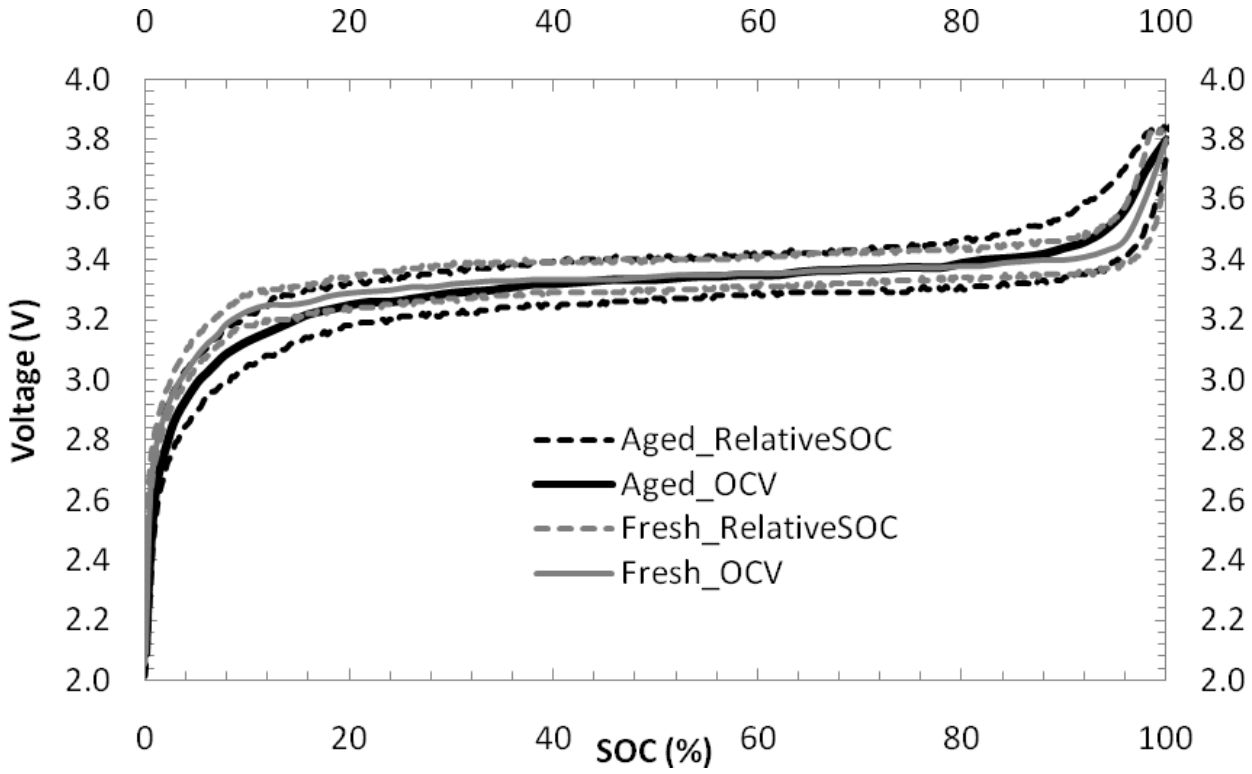

Figure 25: OCV of Fresh and Aged Battery Cells [44]

OCV estimation is often very difficult due to the hysteresis of the voltage profile during charge and discharge [49]. Although hysteresis is not well understood, it can be thought of as a charge momentum that creates a condition wherein the battery voltage will not trace back along the same voltage profile upon reversal of current. Also, there is a rest period that must take place before the battery's voltage will return to open circuit.

Typically, the battery's open OCV is estimated utilizing a simple equivalent circuit model. The simple circuit model is shown in Figure 26.

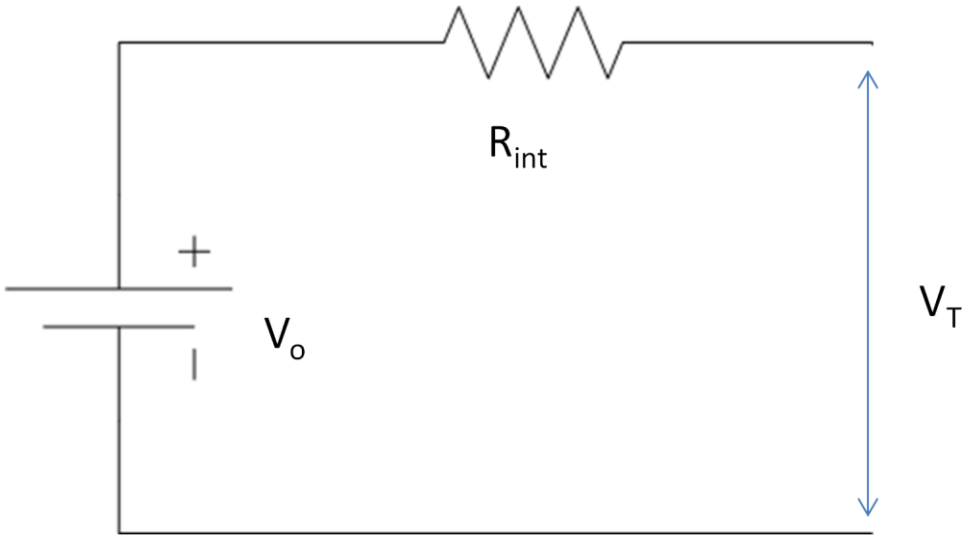

Figure 26: Simple Thevenin Battery Model

where:

Vt is the terminal voltage

Rint is the battery's internal resistance

Vo is the battery's open circuit voltage

This simple Thevenin equivalence model gives decent representation of the battery however there are some obvious omissions.

The simplest model of open circuit voltage, then, is the following

$$y_k = OCV(SOC_k) - Ri_k \qquad \text{equation 8}$$

where:

k is the time step

y_k is terminal voltage

The internal resistance of the battery is dependent on whether the battery is being charged or discharged. Adding two resistors in parallel with diodes in each direction give a more accurate

depiction. Including the two resistances help in addressing the hysteresis issues with indentifying OCV. However, adding a capacitor and internal diffusion resistances address the rest period effects and hysteresis of the voltage. The final circuit is shown in Figure 27.

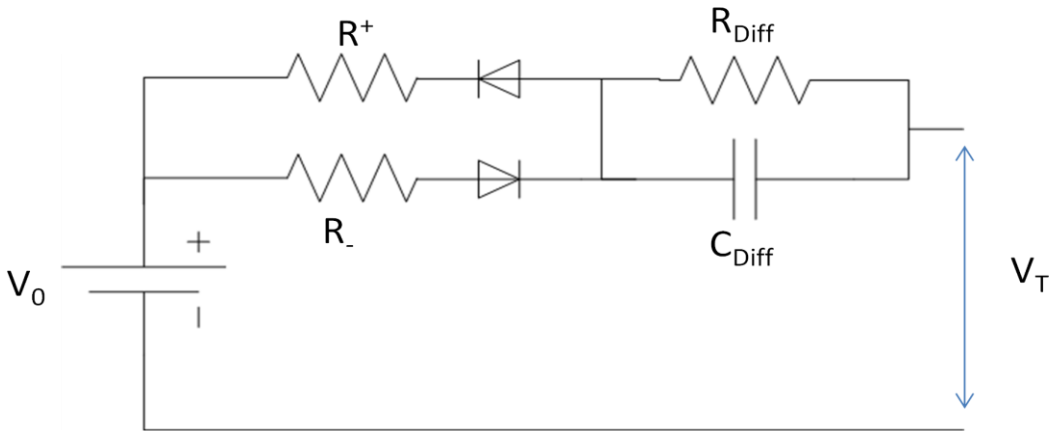

Figure 27: Variable Resistance and Relaxation Battery Model

where

R_{Diff} is the resistance of mass diffusion through the electrolyte

C_{Diff} is the capacitance of diffusion

R^+ is the discharge resistance

R^- is the charge resistance

Due to the fact that R_{Diff} is relatively small compared to the charge and discharge resistance, and the C_{Diff} is nearly negligible for $LiFePO_4$ cells, the R_{Diff} will be included in the charge and discharge resistance term.

Equation 7 can be modified to include the hysteresis effect as follows:

$$y_k = OCV(SOC_k) - Ri_k + s_k M(SOC_k) \quad \text{equation 9}$$

where:

$M(SOC_k)$ is the maximum hysteresis loop

s_k is dependent on the direction of the current with memory during resting and is defined as

$$s_k = \begin{cases} 1, & i_k > \varepsilon \\ -1, & i_k < \varepsilon \\ s_{k-1}, & |i_k| \leq \varepsilon \end{cases} \quad \text{equation 10}$$

for some sufficiently small, positive value of ε

$M(SOC_k)$ is half of the difference between the charge and discharge curves minus the effect of resistance.

Resistance can be a constant, a different constant for discharge and charge, a function of temperature and a function of SOC, depending on the accuracy required and the data available for system identification.

Utilizing OCV Estimation is made difficult with many battery chemistries that have a very flat OCV vs SOC curve as shown. Between 10% and 90% SOC, the voltage change is very small (approx 0.2 V for LiFePO4) and therefore it is difficult to utilize OCV in that area of operation. Also, it requires a very accurate voltage measurement to utilize this technique.

2.3.2 Coulomb Counting

Coulomb counting is the most common method of SOC estimation for consumer applications. The simple principle used in coulomb counting is that the number of electrons transferred to charge the battery pack is equal to the number of electrons transferred to discharge the battery [49]. Therefore the maximum number of electrons that are transferrable around the load is equal to the nominal capacity in Ampere-seconds.

$$SOC = SOC_0 + \frac{1}{C_n}\int I_{batt} - I_{loss}dt$$ equation 11

SOC is essentially the percentage of available coulombs that have moved around the load from the anode to the cathode. A current sensor is inserted into the loop and the current is integrated over time. The current sensor is generally either a Hall Effect sensor or a current shunt. A Hall Effect sensor measures the magnetic flux around a conductor and correlates the flux to a current flowing through the wire since magnetic flux is proportional to the current. A current shunt places a very small resistance in series with the load loop and measures the voltage across the resistor. The voltage is directly proportional to the current due to Ohm's law. There are tradeoffs between each sensor. Typically Hall Effect sensors are lower cost than the current shunts. They are easier to integrate and do not require a controller to have a high voltage sensor reference like the current shunt. The current shunt, however, can be much more accurate and precise.

Coulomb counting works well with extremely precise, very accurate, high frequency measurements. Generally measurements of this accuracy are impossible or near impossible to achieve and therefore a more robust method is needed for the required accuracy in SOC estimation.

2.3.3 Impedance Spectroscopy

Impedance spectroscopy is often used in chemical processes for determination of concentrations of chemical compounds. There have been many papers relating the low frequency a.c. impedance of a cell with the cell's SOC. A Nyquist plot is shown in Figure 28.

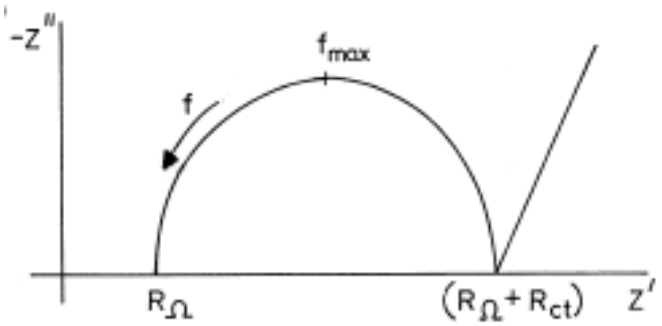

Figure 28: Nyquist Plot [50]

Essentially the theory is that at high SOCs, the main resistance of the electrochemical reaction is charge transfer resistance as opposed to diffusion resistance. As the SOC drops, the charge transfer resistance contributions lessens and diffusion resistance controls the reactions. Therefore the Nyquist plot becomes more and more linear as the SOC lowers as shown in Figure 29.

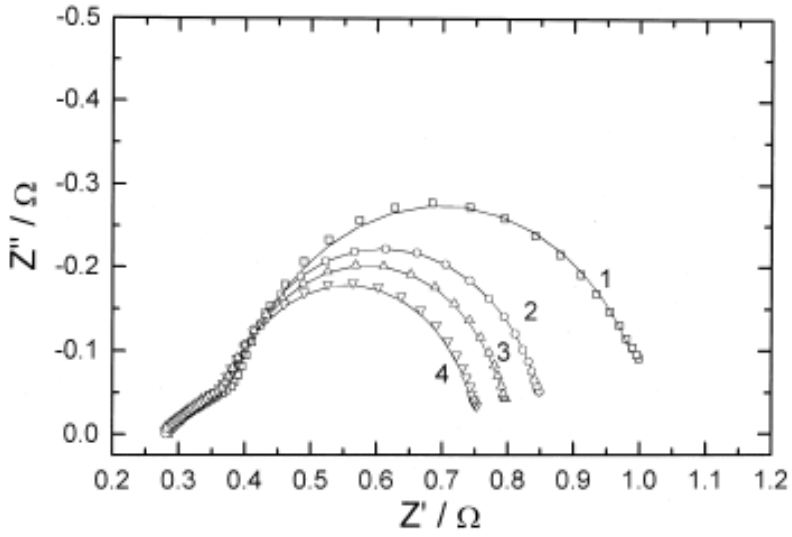

Figure 29: Nyquist Plot for Varying SOCs (Inductive Data Omitted) [50]

The main disadvantages of Impedance spectroscopy for SOC estimations are that it is very temperature sensitive and it can be quite expensive. Also, there is a strong influence of cell

aging on the measurement of the impedance which could be strongly correlated as shown in Figure 30.

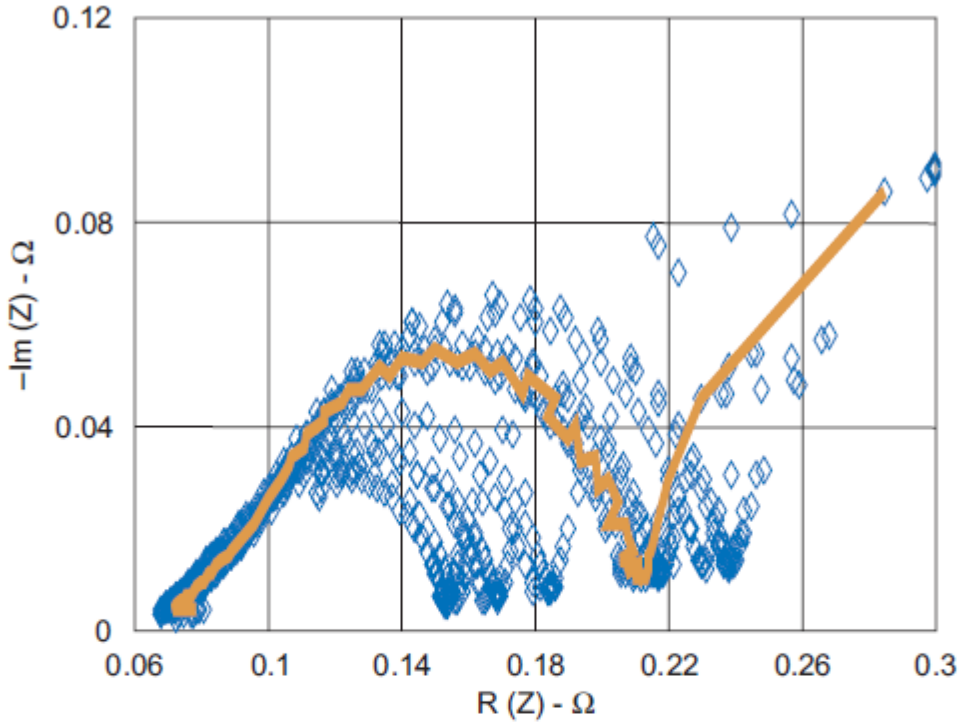

Figure 30: Nyquist Plots for Various States of Health [1]

The difficulty of this correlation is to split out the effect of SOC from the effect of SOH. Therefore, many papers have started exploring using impedance spectroscopy as an indicator of SOH given another form of SOC estimation [51].

2.3.4 Adaptive Methods

More recently, adaptive methods of SOC estimation have been explored. The adaptive methods explored most frequently include neural networks, fuzzy logic, adaptive observers, vector machines and Kalman filtering. These methods are often expensive to develop and require significant processing capabilities.

Very promising work has been done in the area of Extended Kalman Filtering since it enables the estimator to adapt to a cells changing characteristics over the life of the cell [52].

2.3.5 Kalman Filtering

Kalman filtering is an example of optimal state estimation. The state of a system is defined as variables that are not directly measurable that provide a complete representation of the internal condition of the system [53]. Kalman filtering is used to estimate the state of the system given a process model of the system and a measurement model of the system. It relies on the Markov assumption that the state is entirely defined by the previous belief of the state of the system and the current control inputs and measurement outputs.

Although it is beyond the scope of this thesis to fully derive the equations utilized for Kalman filtering, the following will provide a step by step explanation of how the filter works. Initially, the Kalman filter will be described, which is an optimal state estimation of a linear time varying (LTV) system. In reality battery systems are highly non-linear, and therefore will require the use of an Extended Kalman Filter, describe later. It should also be noted that there are many forms of Kalman filtering available depending on the system under investigation and this work will use just one of those forms. Also, there are other state estimation filters that can be utilized each of which have advantages and disadvantages such as particle filtering, H-infinity filtering and Unscented Kalman Filtering. Kalman filtering, however is the most common filter applied in other areas of control including target tracking and signal processing.

A Kalman filter is a recursive least squares filter that uses a system or process model, a measurement model and a series of noisy measurements to formulate a belief about a system's state [2]. Since it is a recursive filter, the Kalman filter assumes that only the current measurements and the belief of the previous state are required to estimate the current state of the system.

To begin, consider an LTV system as described in Figure 31.

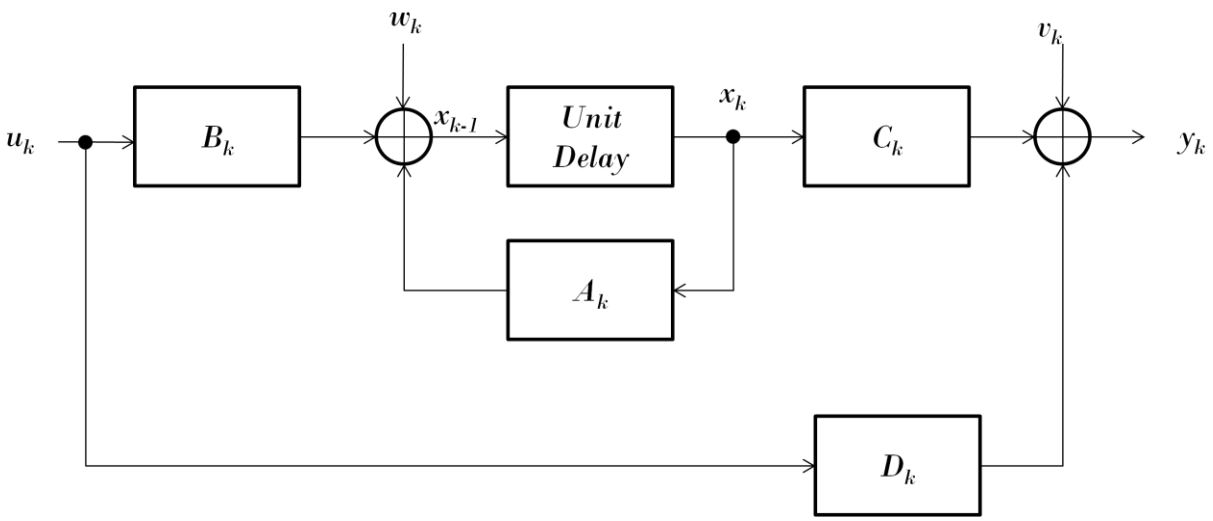

Figure 31: Linear Time Varying System

The system is described by the state space model for discrete time systems:

$$x_{k+1} = A_k x_k + B_k u_k + w_k \qquad \text{equation 12}$$

$$y_k = C_k x_k + D_k u_k + v_k \qquad \text{equation 13}$$

where:

x_k is the state vector

u_k is the control input

y_k is the measurement vector

Equation 11 is known as the process model (or state equation) of the system and equation 12 is known as the measurement model. The process model is setup to capture the system dynamics of the system. All controllability and stability are determined by the process model.

In the process model, w_k is white process noise and is assumed to be zero-mean and Gaussian with covariance Q_k as in:

$$w_k \sim (0, Q_k) \qquad \text{equation 14}$$

Similarly, v_k is the measurement noise, generally from a noisy sensor input and is also assumed to be zero-mean and Gaussian with covariance R_k as in:

$$v_k \sim (0, R_k) \qquad \text{equation 15}$$

Given these equations and some measurement data, the goal of the Kalman filter is to estimate the unmeasured state of a system. For instance, in the case of the battery, it may be state of charge or state of health. Since the Kalman filter is recursively minimizing the mean squared error between the two models, and assuming Gaussian distribution of any noise, the Kalman filter is considered optimal.

The Kalman filter has two stages, a prediction stage and an update stage. The process model is used to predict the belief of the state and the measurement model is used to update the belief.

During the prediction stage, an estimate of the state based on the process model is calculated given the control input and a prediction of the covariance is calculated. In the following equations $\tilde{x}$ denotes the belief of the state. Prior to the update, the state belief is denoted $\tilde{x}_k^-$, after the measurement update, the state belief is denoted $\tilde{x}_k^+$.

Prediction Stage:

State estimate update $\tilde{x}_k^- = A_{k-1}\tilde{x}_{k-1}^+ + B_{k-1}u_{k-1}$ equation 16

Error covariance time update $\Sigma_{\tilde{\mathrm{x}},\mathrm{k}}^- = A_{k-1}\Sigma_{\mathrm{x},\mathrm{k}-1}^+ A_{k-1}^T + \Sigma_{\mathrm{w}}$ equation 17

Update Stage:

Kalman Gain calculation $L_k = \Sigma_{\tilde{x},k}^- C_k^T \left[C_k \Sigma_{\tilde{x},k}^- C_k^T + \Sigma_v\right]^{-1}$ equation 18

State estimate measurement update $\tilde{x}_k^+ = \tilde{x}_k^- + L_k\left[y_k - C_k\tilde{x}_k^- - D_k u_k\right]$ equation 19

Error covariance measurement update $\Sigma_{\tilde{x},k}^+ = (I - L_k C_k)\Sigma_{\tilde{x},k}^-$ equation 20

This is a widely known solution to minimizing the mean squared error. For more derivation of the above review [53].

2.3.6 Extended Kalman Filter

The Kalman filter described the optimal solution for linear systems. In reality, battery systems are non-linear and therefore the Extended Kalman Filter (EKF) must be used. The EKF utilizes many of the same principles as the Kalman filter, however it linearizes the system at each time step allowing the system to be solved as a linear time varying (LTV) system. It is important to understand that the EKF is no longer necessarily optimal.

Consider the non-linear system:

$$x_{k+1} = f(x_k, u_k) + w_k \qquad \text{equation 21}$$

$$y_k = g(x_k, u_k) + v_k \qquad \text{equation 22}$$

At each time step the $f(x_k, u_k)$ and $g(x_k, u_k)$ are linearized using a first order Taylor series expansion around the point $x_k = \tilde{x}_{k-1}^{+}$ for the process model and $x_k = \tilde{x}_k^{-}$ for the measurement model.

$$f(x_k, u_k) \approx f(\tilde{x}_{k-1}, u_k) + \left.\frac{\partial f(x_k, u_k)}{\partial x_k}\right|_{x_k = \tilde{x}_{k-1}} (x_k - \tilde{x}_{k-1}) \qquad \text{equation 23}$$

$$g(x_k, u_k) \approx g(\tilde{x}_k^{-}, u_k) + \left.\frac{\partial g(x_k, u_k)}{\partial x_k}\right|_{x_k = \tilde{x}_k^{-}} (x_k - \tilde{x}_k) \qquad \text{equation 24}$$

Substituting equation 23 and 24 into equation 21 and 22, and defining A_k and C_k as follows:

$$\hat{A}_k = \left.\frac{\partial f(x_k, u_k)}{\partial x_k}\right|_{x_k = \tilde{x}_{k-1}} \quad \text{equation 25}$$

$$\hat{C}_k = \left.\frac{\partial g(x_k, u_k)}{\partial x_k}\right|_{x_k = \tilde{x}_k^-} \quad \text{equation 26}$$

The linearized process and measurement models become:

$$x_{k+1} \approx \hat{A}_k x_k + f(\tilde{x}_k, u_k) - \hat{A}_k \tilde{x}_k + w_k \quad \text{equation 27}$$

$$y_k = \hat{C}_k x_k + g(\tilde{x}_k, u_k) - \hat{C}_k \tilde{x}_k + v_k \quad \text{equation 28}$$

To define the EKF iteration process, replace the B_k from the Kalman filter with the middle two terms of the process model and replace D_k with the middle two terms of the measurement model. The final process is much the same as the standard Kalman Filter and becomes:'

Prediction Stage:

State estimate time update $\tilde{x}_k^- = f(\tilde{x}_{k-1}^+, u_{k-1})$ equation 29

Error covariance time update $\Sigma_{\tilde{x},k}^- = \hat{A}_{k-1}\Sigma_{x,k-1}^+\hat{A}_{k-1}^T + \Sigma_w$ equation 30

Update Stage:

Kalman Gain calculation $L_k = \Sigma_{\tilde{x},k}^-\hat{C}_k^T\left[C_k\Sigma_{\tilde{x},k}^-\hat{C}_k^T + \Sigma_v\right]^{-1}$ equation 31

State estimate measurement update $\tilde{x}_k^+ = \tilde{x}_k^- + L_k[y_k - g(\tilde{x}_k^-, u_k)]$ equation 32

Error covariance measurement update $\Sigma_{\tilde{x},k}^+ = \left(I - L_k\hat{C}_k\right)\Sigma_{\tilde{x},k}^-$ equation 33

There are other non-linear versions of the Kalman Filter including the unscented Kalman Filter that may provide similar results.

3 Model Development

3.1 SOC Extended Kalman Filter Design

Since the EKF is specifically designed to handle 'noisy' measurements, it is the ideal process for estimating SOC on the battery test stand and onboard system. In designing the SOC EKF algorithm there are a few goals to consider:

1. Provide accurate SOC estimation over degradation test cycles;
2. Provide reasonable error bounds on the SOC estimation;
3. The philosophy and theory should be understandable, and the algorithm simple enough for processing speed and ease of implementation;

3.1.1 Battery EKF Model

The battery process model must be a function of the control input, which in this case is current. Recall that the state that is being estimated is 'State of Charge' (SOC). Therefore, the ideal model is the same model described above, the coulomb counting model.

Recall:

$$SOC = SOC_0 + \frac{1}{C_n}\int I_{batt} - I_{loss}dt \qquad \text{equation 34}$$

Discretizing equation 33 yields the following equation:

$$SOC_k = SOC_{k-1} + \frac{\eta i_k \Delta t}{C_n} + w_k \qquad \text{equation 35}$$

Where:

C_n is the nominal capacity of the battery in Ampere-seconds

η is the coulombic efficiency of the battery for either charge or discharge.

Coulombic efficiency is assumed to be 1 for discharge and 0.992 for charge [49]. The Coulombic efficiency of battery the ratio of the number of 'charged electrons' that enter the battery during charging compared to the number that can be effectively used during discharge. The losses that reduce Coulombic efficiency are primarily due to secondary reactions, such as the electrolysis of water, plating of Li, or other electrochemical reactions in the battery. Thus overall cell Coulombic efficiency or charge acceptance is a measure of how much usable energy is available during discharging compared with the energy used to charge the cell and is expressed as the ratio between the discharge energy and the charging energy. This model of simple dynamics of the battery system will serve as a basis for the EKF model.

The measurement model for the battery must be a function of the state and inputs. Currently the measured inputs available on the battery test stand are voltage and temperature. Although resistance is a function of temperature, the most benefit for the model comes from including open circuit voltage to correct the coulomb counting model around the ends of the state of charge vs voltage curve. Therefore, the basis for the measurement model will be the simple OCV model from above.

Recall the simple model equation:

$$y_k = OCV(SOC_k) - Ri_k \qquad \text{equation 36}$$

It is assumed that the resistance is only a function of current direction (ie. there is a constant charge resistance and a constant discharge resistance, not dependent on temperature). Inclusion of impact of temperatures changes is left to future work. Once the charge and discharge resistances have been determined, the hysteresis loop can be added to the model to form what Plett calls the *"Zero State"* model [49]:

$$y_k = OCV(SOC_k) - Ri_k + s_k M(SOC_k)$$ equation 37

The zero state model utilizes the resistance term from the simple model and allows for identification of the hysteresis term. Plett also proposes two other models for utilization on vehicles, the one state hysteresis model and the enhanced self correcting model. For the purpose of keeping the model as simple as possible, the zero state model was chosen, limiting the states in the process model to one.

3.1.2 System Identification for the Zero State Model

3.1.2.1 Charge/Discharge Curve for Open Circuit Voltage

The first requirement for the model is to determine the open circuit voltage as a function of state of charge. The easiest way to determine the relationship is to slowly charge and discharge a battery cell to the voltage limits prescribed by the cell manufacturer. The open circuit voltage curve is then the difference between the charge and discharge curves. Note, this is not practical in actual application because of the impact on the durability of the cells, the time required, equipment required, and the desire not to completely drain the battery pack.

Figure 32 shows the charge and discharge curves at ±0.2C as well as the calculated open circuit voltage curve.

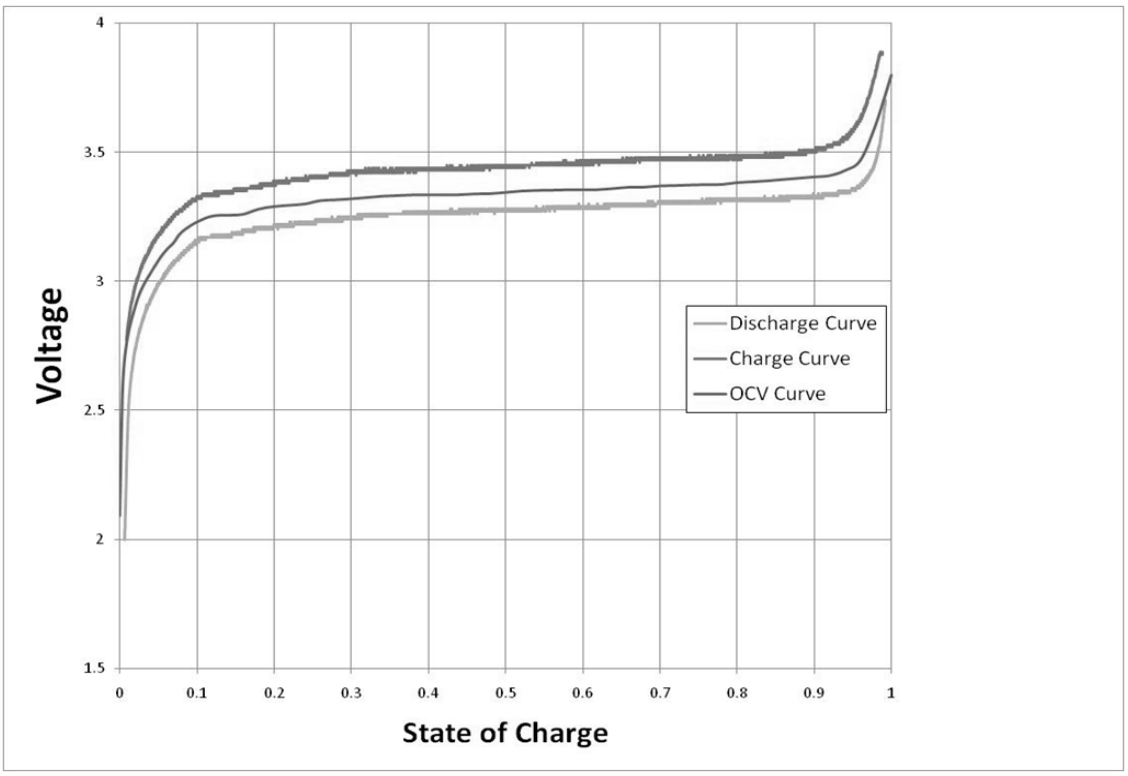

Figure 32: Charge and Discharge Curves at 0.2 C for the A123 M26650 cell tested at Waterloo.

3.1.2.2 Generating the Parameters for the Simple Model

The first step in identifying the system parameters is to identify the resistance term in the simple model. The simple model overvoltage vector is setup as follows

$$Y = \begin{bmatrix} y_1 - OCV(SOC_1) \\ y_2 - OCV(SOC_2) \\ y_3 - OCV(SOC_3) \\ \vdots \\ y_n - OCV(SOC_n) \end{bmatrix} \quad \text{equation 38}$$

And the matrix H is defined as:

$$H = \begin{bmatrix} i_1^+ & i_1^- \\ i_2^+ & i_2^- \\ i_3^+ & i_3^- \\ \vdots & \vdots \\ i_n^+ & i_n^- \end{bmatrix}$$ equation 39

Then the equality derived from the measurement model is

$$Y = H\hat{R}$$ equation 40

Where $\hat{R}$ is the matrix of resistances:

$$\hat{R} = \begin{bmatrix} R^+ \\ R^- \end{bmatrix}$$ equation 41

Utilizing the known Y and H matrices from the OCV curve calculation from above, the $\hat{R}$ vector can be determined by the equation:

$$\hat{R} = (H^T H)^{-1} H^T Y$$ equation 42

For the cells utilized in this work the resistance values are (in Ohms):

$$\hat{R} = \begin{bmatrix} 0.0332 \\ 0.0488 \end{bmatrix}$$ equation 43

Knowing the value of $\hat{R}$, the simple model is completely defined with a lookup table being used for OCV as a function of SOC.

3.1.2.3 Generating Parameters for the Zero State Model

A similar process is used to determine the parameters in the zero state model. The major hysteresis term in the zero state model is defined as half the distance between the charge and discharge curves minus the resistance overpotential. M(SOC) is plotted in Figure 33. The top curve is for the discharge hysteresis, the bottom curve is the charge hysteresis.

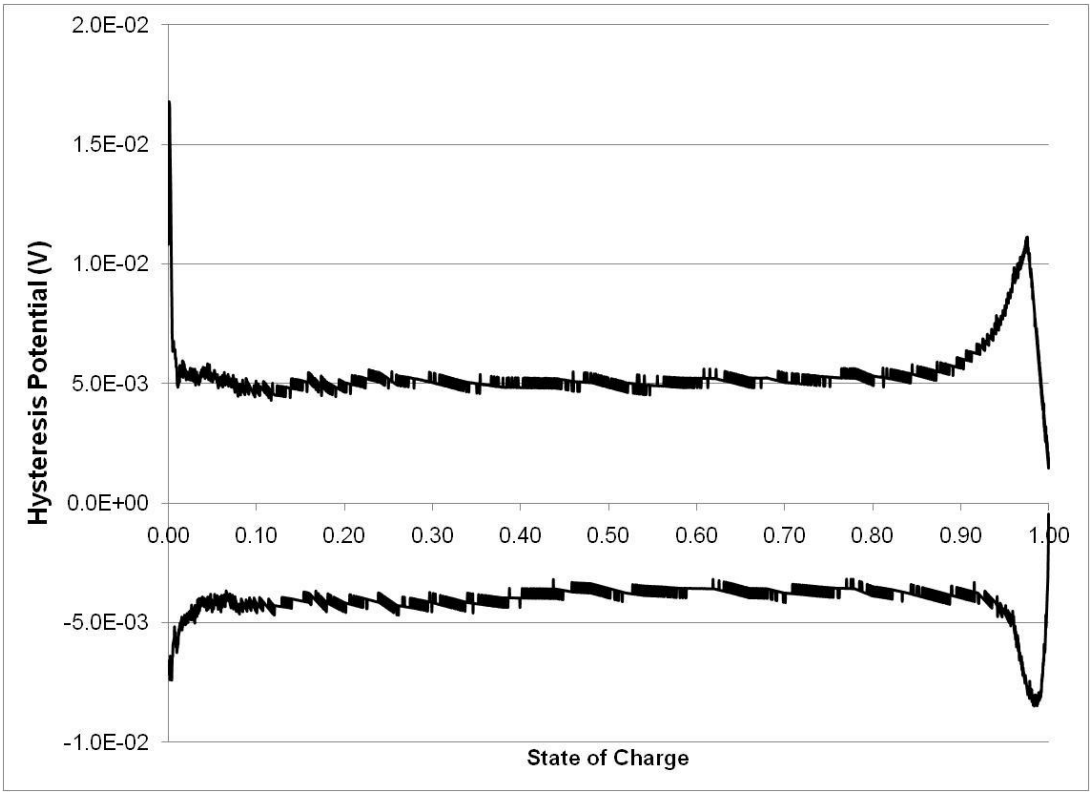

Figure 33: Hysteresis as a Function of SOC and Current.

To determine the constants for the zero state model, the H matrix is augmented as follows:

$$H = \begin{bmatrix} i_1^+ & i_1^- & s_1 \\ i_2^+ & i_2^- & s_2 \\ i_3^+ & i_3^- & s_3 \\ \vdots & \vdots & \vdots \\ i_n^+ & i_n^- & s_n \end{bmatrix} \quad \text{equation 44}$$

Where s_k is the indication of current direction as defined in equation 9. Also, $\hat{R}$ is augmented to include a constant for the major hysteresis loop.

$$\hat{R} = \begin{bmatrix} R^+ \\ R^- \\ M \end{bmatrix} \quad \text{equation 45}$$

Using the same procedure as before, the $\hat{R}$ matrix is calculated, the results of which are below

$$\hat{R} = \begin{bmatrix} 0.0132 \\ 0.0200 \\ 0.0180 \end{bmatrix} \quad \text{equation 46}$$

3.1.2.4 Hysteresis as a Constant or a Function

In the zero state model, the model assumes a constant for the hysteresis loop which is essentially true for all SOC between 0.1-0.9, as seen in Figure 35. This model is quite good for the normal operation of a vehicle as the SOC is rarely utilized outside of those limits. However, since the hysteresis is relatively large at high and low SOC, for the purposes of the battery test stand, which will operate a significant amount of time in the upper and lower SOC ranges, the hysteresis at those points must be taken into account.

3.1.3 Testing the Simple Model and the Zero State Model Parameters

In order to adequately test the parameters of both the zero state and the predicted voltage from the measurement models was analyzed versus the measured voltage of a slow (0.2C) full charge and discharge cycle on the battery test stand.

First the simple model was used to predict the voltage. The results are shown in Figure 34.

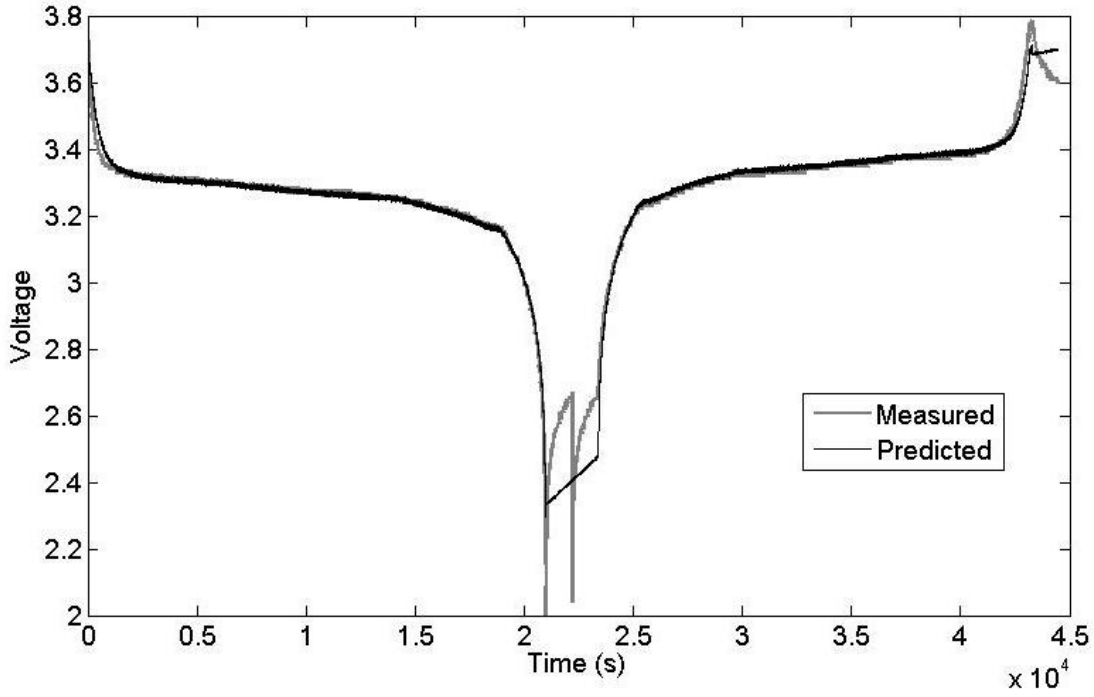

Figure 34: Simple Model Voltage Prediction

The simple model predicts the voltage well, particularly throughout the middle part of each of the charge and discharge cycles. However, at the low voltage point it loses the ability to adequately track the measured voltage. The cycle test was setup to try and stabilize the voltage around 2.2 volts, which is why the measured data shows some dynamics, while the prediction does not try to stabilize the voltage. More importantly, the prediction does not accurately predict the voltage during the constant voltage part of the charge cycle. Since the actual cell is

rebounding from hysteresis due to being charged and the simple model does not include any hysteresis term, it is unable to track the voltage correctly.

Next, the zero state model was tested over the same cycle. The results are shown in Figure 35.

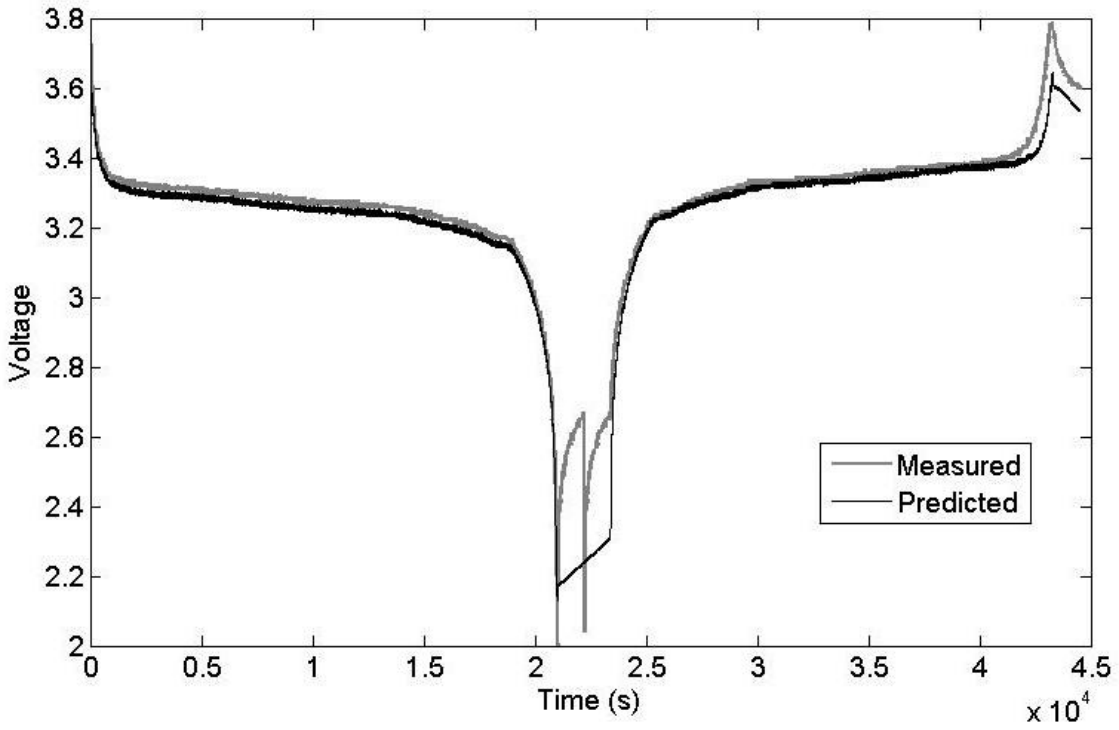

Figure 35: Zero State Hysteresis Model Voltage Prediction

The zero state model accomplishes two major improvements over the simple model. First, the zero state model is able to more accurately predict the voltage at the end of the discharge, although it still has a problem accurately depicting the dynamics. Mainly average voltage that the zero state model predicts is closer than the simple model. Secondly, the zero state model's hysteresis term is able to trend the voltage during the constant voltage part of the charge. Since much of the testing on the stand will include the constant voltage charging, it is important to include that in the SOC algorithm.

4 Results and Discussion

4.1 EKF Implementation

The following process and measurement models were utilized for the implementation of the SOC EKF.

Process Model:

$$SOC_k = SOC_{k-1} + \frac{\eta i_k \Delta t}{C_n} + w_k \qquad \text{equation 47}$$

Measurement Model:

$$y_k = OCV(SOC_k) - Ri_k + M(i_k, SOC_k) + v_k \qquad \text{equation 48}$$

The zero state model has the benefit of not having complex matrix calculations since the process model only has a single state. Therefore, some of the implementation becomes much easier. Specifically, since the second term in the process model is not a function of x_k, A_{k-1} equal to 1.

Therefore, the error covariance time update is a simple step that reduces to:

$$\Sigma^{-}_{\tilde{x},k} = 1 \times \Sigma^{+}_{x,k-1} \times 1 + \Sigma_w \qquad \text{equation 49}$$

Essentially, the error covariance time update just adds the covariance of the process noise estimate each time. Also, since A_k and C_k are both one term matrices, all of the transposes required are just scalars, so the covariances are both relatively easy to compute.

Recall:

$$\hat{C}_k = \left.\frac{\partial g(x_k, u_k)}{\partial x_k}\right|_{x_k = \tilde{x}_k} \qquad \text{equation 50}$$

Since the Ri_k term in $g(x_k, u_k)$ is not a function of SOC, the only terms in C_k are the OCV term and the M(SOC) term.

To determine $C_{k,OCV}$, the OCV lookup table is used and a central differencing is carried out around the current SOC estimation at each time step.

$$\hat{C}_{k,OCV} = \frac{OCV(SOC_{k-1} + \delta) - OCV(SOC_{k-1} - \delta)}{(SOC_{k-1} + \delta) - (SOC_{k-1} - \delta)} \qquad \text{equation 51}$$

For some sufficiently small positive value δ chosen to be 0.001 for this study.

The down side of using a central differencing technique is that the effect of variance of voltage with respect to OCV(SOC) is reduced. However, what will become evident is that the error in the voltage measurement itself is dominant.

To determine the $C_{k,M}$ a hysteresis lookup table is also used. Since the table is based on the current, there are two central difference formulae that apply:

$$\hat{C}_{k,Mpos} = \frac{Mpos(SOC_{k-1} + \delta) - Mpos(SOC_{k-1} - \delta)}{(SOC_{k-1} + \delta) - (SOC_{k-1} - \delta)} \qquad \text{equation 52}$$

When current is positive (discharge) and:

$$\hat{C}_{k,Mneg} = \frac{Mneg(SOC_{k-1} + \delta) - Mneg(SOC_{k-1} - \delta)}{(SOC_{k-1} + \delta) - (SOC_{k-1} - \delta)} \quad \text{equation 53}$$

When current is negative (charge).

The main problem with the hysteresis table is that it is discontinuous based on the direction of current. The discontinuous nature of the table could cause instability at low current draws and will require tuning of the s_k term by decreasing or increasing the ε term from equation 9. Although this is a violation of EKF assumptions, the algorithm still works well.

4.1.1 Determining Variances

In order to implement the EKF, the process variance and measurement variance values must be properly determined.

4.1.1.1 Determining Process Variance

Initially, it is assumed that the process noise is entirely derived from the accuracy of the programmed current set point. The current on the battery test stand is determined using the current measurement from the load (TDI Dynaload) minus the current measurement of the source (ie. the Lambda), since the control algorithm requests negative current from one and positive current from the other. The manufacturer of the load published a specification that the programmed current accuracy is ±0.5% of the current requested and a regulation of ±0.1%. The variance of the current set point for the load is then:

$$\sigma_L^2 = \sigma_{Accuracy}^2 + \sigma_{Regulation}^2 \quad \text{equation 54}$$

Assuming the load manufacturer is quoting accuracy and regulation on a 99% confidence interval, the standard deviation of the accuracy and the regulation would be:

$$\sigma_{Accuracy} = \frac{0.5\%}{2.6} = 0.2\% \qquad \text{equation 55}$$

$$\sigma_{Regulation} = \frac{0.1\%}{2.6} = 3.8 \times 10^{-2}\% \qquad \text{equation 56}$$

Using equation 53 the variance from the load is equal to $4.1X10^{-2}$%.

The manufacturer of the source publishes a specification for the programmed current to be accurate to ±(0.4% + 40 mA). Again, assumed to be a 99% confidence interval, the standard deviation as derived above would be ±(0.2% + 15 mA).

Variance in the SOC due to the variance in current is calculated utilizing the partial derivative of SOC with respect to current.

By definition:

$$\sigma^2_{SOC,Current} = \left(\frac{\partial SOC_k}{\partial i_k}\right)^2 \left(\sigma^2_{Current}\right) \qquad \text{equation 57}$$

And:

$$\sigma^2_{Current} = \sigma^2_{Load} + \sigma^2_{supply} \qquad \text{equation 58}$$

Therefore:

$$\sigma^2_{SOC,Current} = \left(\frac{\partial SOC_k}{\partial i_k}\right)^2 \left(\sigma^2_{Load,Accuracy} + \sigma^2_{Load,Regulation} + \sigma^2_{supply}\right) \quad \text{equation 59}$$

And:

$$\left(\frac{\partial SOC_k}{\partial i_k}\right)^2 = \frac{\eta \Delta t}{C_n} \quad \text{equation 60}$$

Therefore, for example, a current load of 30A and a supply of 5A would yield a variance of:

$$\sigma^2_{SOC,Current} = \left(\frac{1 \times 1s}{8280s}\right)^2 (8.6 \times 10^{-3}) = 1.3 \times 10^{-10} \quad \text{equation 61}$$

Since the overall capacity of the battery is so high compared to the current draw at any one time, the current variance contributes a very small amount to the overall process error. A process variance of this magnitude is likely to drive the model to neglect all measurements. Simon discusses a method of artificially increasing the process noise to better consider the measurements during the final model tuning [53]. There will be more discussion on improving the model by increasing the process noise in a later section.

4.1.1.2 Measurement Variance

For the voltage measurement error, the TDI Dynaload's voltage sensor is utilized. TDI specifications show an accuracy of 1% ±10mV. Therefore, the variance at the nominal 3.3 V would be:

$$v_k = \sigma_y^2 = (3.3 \times 0.001 + 0.01)^2 = 1.8 \times 10^{-4} \quad \text{equation 62}$$

Applying the process and measurement noise completes the system identification of the model. Further model tuning will be discussed during the initial results.

4.1.2 Model Comparison and Tuning

For initial results analysis, the batteries underwent a series of charge/discharge cycles combined with some minimal dynamic behaviour. Figure 36 shows a sample of the first 20000 seconds of a cycle. It should be noted that the cycle discharges and charges to the voltage limits set by the manufacturer. Also, during charge, there is a period of constant current (10 A in this example) followed by a period of constant voltage (3.8 V) to top off the cell to ensure that it reaches 100% SOC. The design of the cycling ensures by manufacturers specification that the cell will be cycling completely between 0 and 100% SOC.

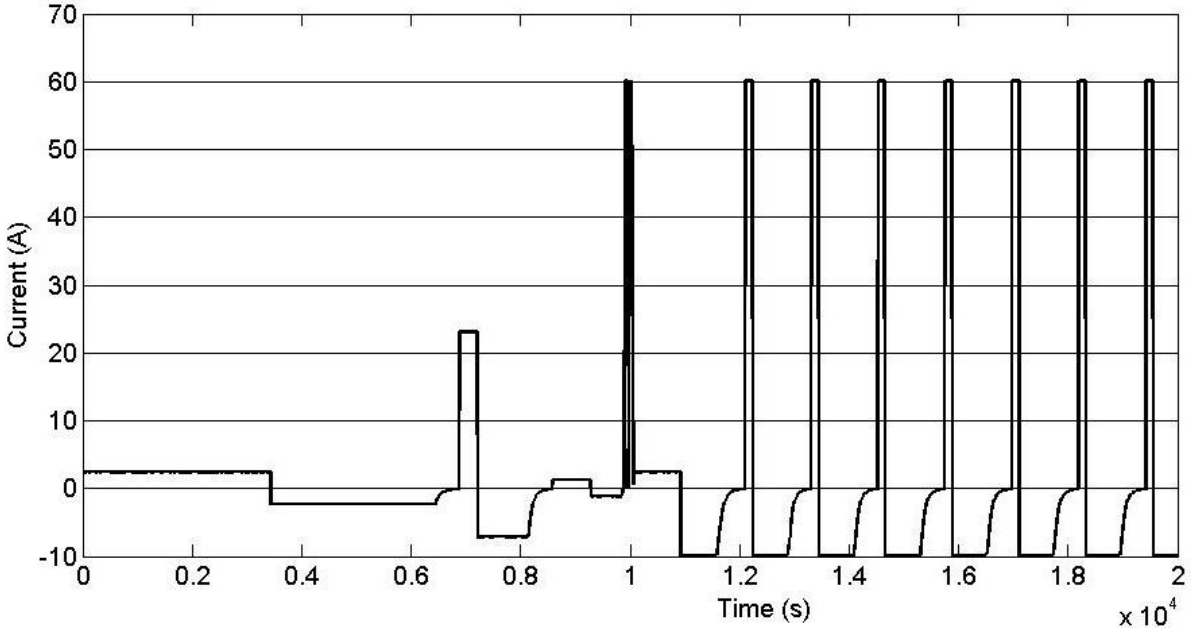

Figure 36: Cycle Testing and Tuning Profile

4.1.3 Comparison of SOC Methods

4.1.3.1 Coulomb Counting

The first test conducted was a test of coulomb counting given the cycle above. The SOC was graphed as a function of time. Initially the tests were carried out to ensure robustness over minimal dynamics. Figure 37 shows the results of the coulomb counting test over the same cycle up to 20000 seconds.

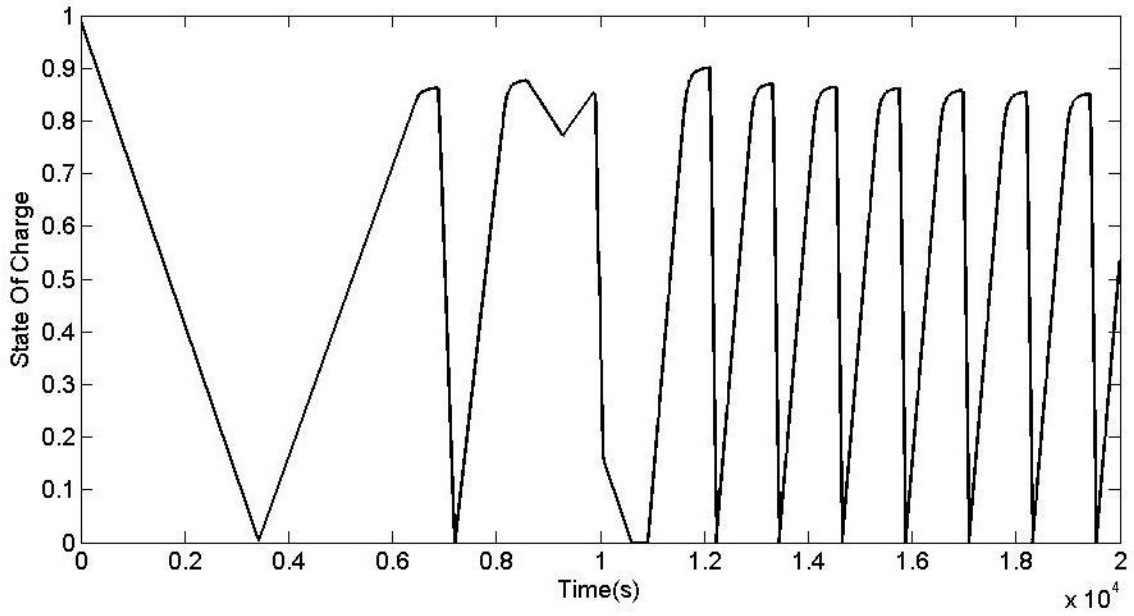

Figure 37: Coulomb Counting Test Sample Data

Immediately it becomes clear that the coulomb counting continuously predicts a lower and lower full state of charge. This is likely due to the fact that the current sensors are of low accuracy and precision. Also, it could be due to the fact that the reporting frequency of both the load and source is not adequate to capture the smaller dynamics of the current measurement. Figure 37 depicts exactly why it is important to update the SOC algorithm with a more robust solution.

4.1.3.2 OCV Estimation

The second test conducted was to determine if OCV estimation was adequate to estimate SOC. Again the same test was utilized to determine the accuracy and robustness of the algorithm. The results are plotted in Figure 38.

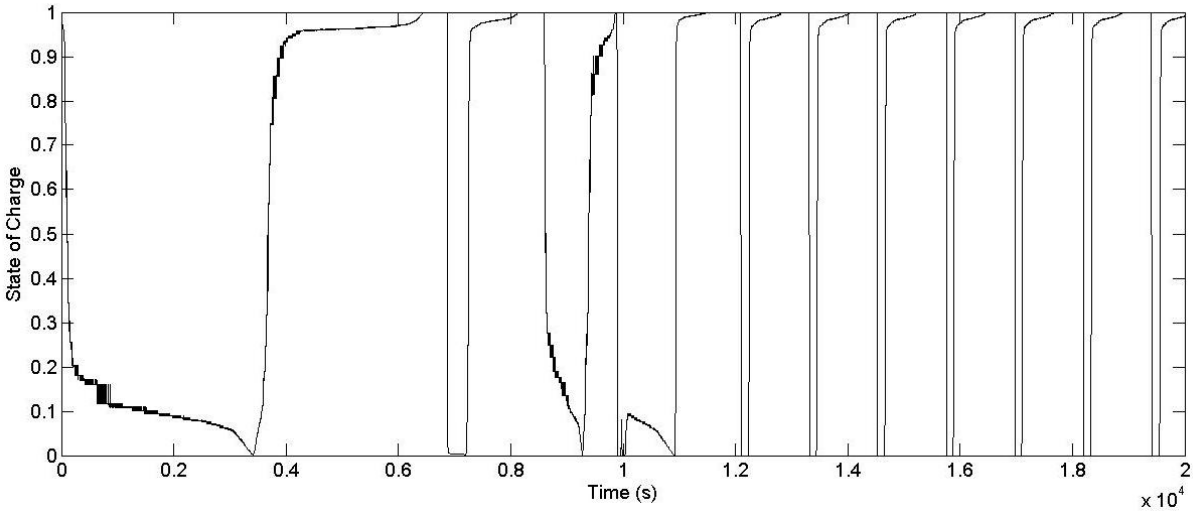

Figure 38: OCV Estimation Test Sample Data

It can be noticed that the OCV improves on the algorithms ability to reach the limits of the SOC reaching zero and one every time, despite the early dynamics. However, on closer inspection, it was realized that the algorithm is predicting a full state of charge, prior to the point that the duty cycle reaches constant voltage. This behaviour is expected since the algorithm will see small changes in voltage and overcompensate for them.

Therefore, it seems that the best result would be a combination of the two, as designed in the EKF.

4.1.3.3 SOC Extended Kalman Filter

The EKF was also tested over the cycle and the results were analyzed. Figure 39 shows the results of the EKF.

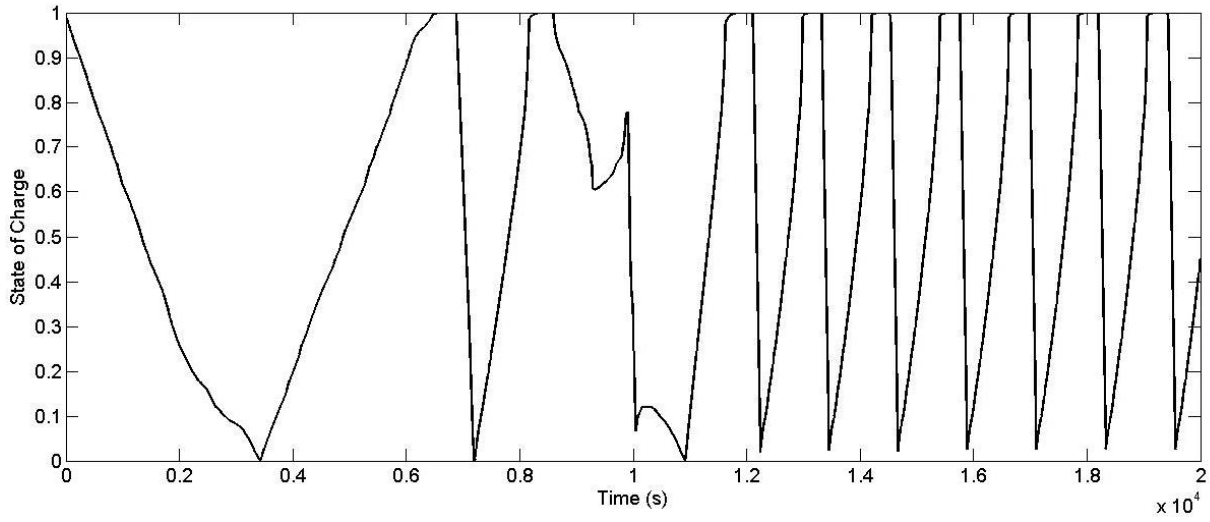

Figure 39: Pre-Tuning EKF Sample Data

As can be seen, the EKF predicts that the SOC is not fully hitting 0% shortly after the first few cycles. The reason for the inaccuracy here is that the process noise was initialized at such a small value that the voltage measurements at lower SOCs were not considered in the EKF. Therefore, to improve the voltage sensing at lower SOCs, the process noise was incrementally adjusted higher until the SOC reached 0 for each of the first 100 cycles. After 100 cycles, the capacity degradation could be the cause of the filter not reaching the lower SOCs. The filter could be artificially set to compensate, if the voltage measurement noise was significantly reduced, however, as the measurement noise is reduced, the filter performs poorly through the middle range of SOCs which is where much of the dynamic cycling will occur, requiring a highly accurate SOC estimation.

The final process noise variance was set to $4.4 \text{ X } 10^{-6}$ and the filter was retested. Figure 40 shows the results with the new process noise variant.

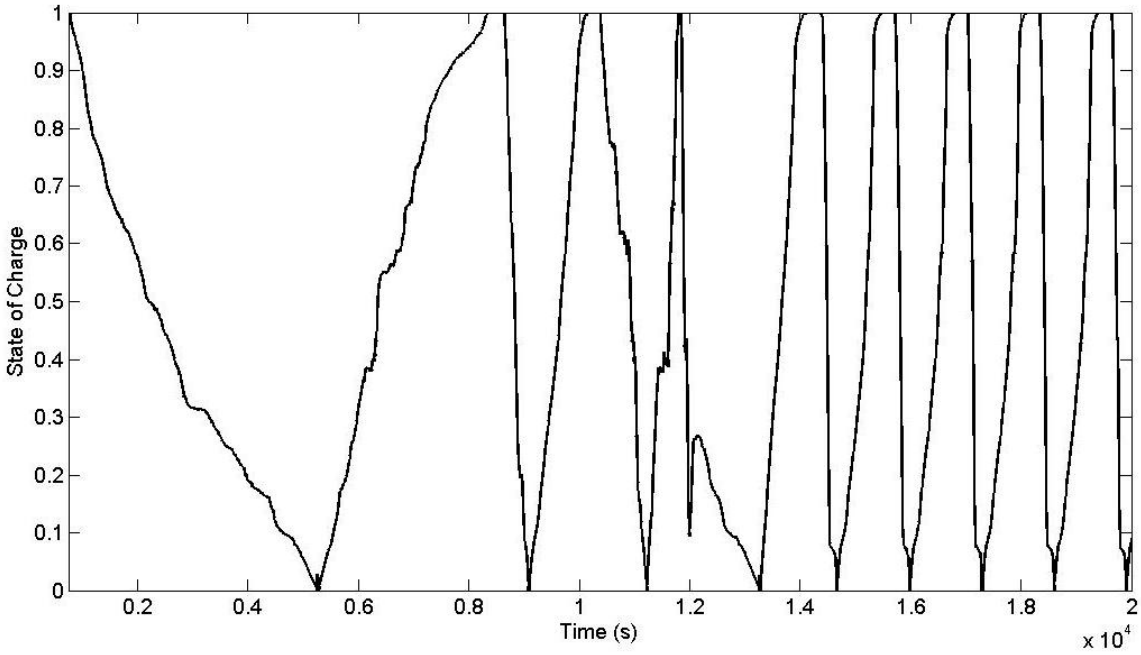

Figure 40: EKF Sample Data After Noise Tuning

Immediately it becomes clear that the EKF does a much better job of predicting the state of charge over the cycles. Combining the three graphs shows a good example of how the EKF is combining the strengths of the two models to better represent the battery SOC.

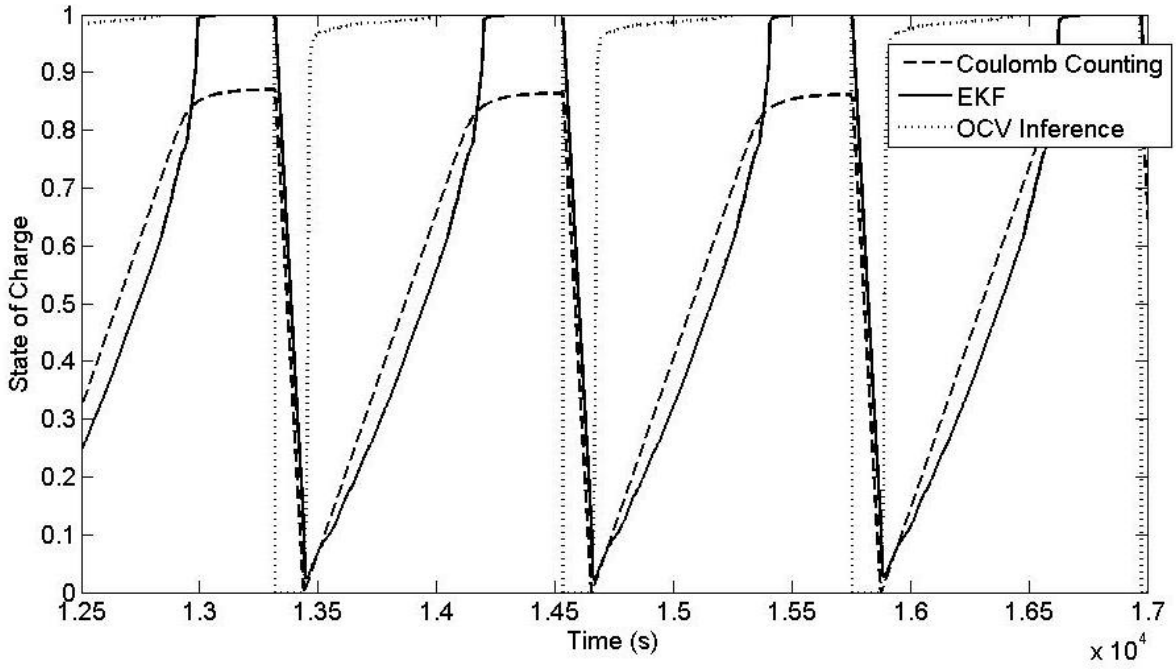

Figure 41: Comparison of SOC Algorithms Sample Data

The EKF was tested over 950000 seconds of data (1000 cycles) to ensure robustness and over several different dynamic cycles and various current draws. It was observed that as more cycles were completed, the EKF tends to lose the ability to correctly estimate SOC. Figure 42 compares the 140^{th} cycle with the 550^{th} cycle.

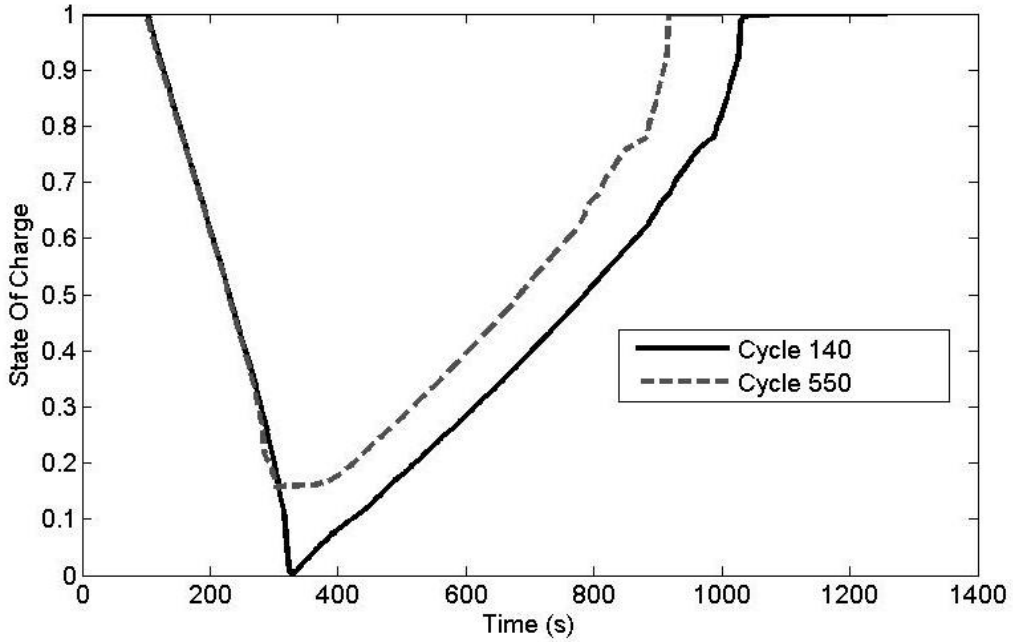

Figure 42: Cycle 550 and Cycle 140 Overlay Showing Effect of Capacity Degradation on SOC Estimation

As the figure shows, the algorithm is no longer reaching zero SOC and quickly reaches full SOC compared to the same cycle from earlier in the testing. This is because the process model utilized is using a constant for battery capacity at the manufacturers rated 8280 As. The problem is of utmost concern since the battery test stand will be used as a test station to test battery degradation over long periods of time and many cycles. Therefore, a dynamic estimate of battery capacity must be included to compensate.

An alternative method could be to increase the dependence on the measurement model; therefore the EKF would use more voltage data during the test. This method was tested and the model did, in fact reach 0% SOC each time. However, the result of artificially decreasing the measurement noise was a less confident (higher error bounds) estimation of SOC during the middle range of SOC (80%-20%). Since most operation occurs in the middle range of SOC, it was decided that the capacity estimate must be included.

4.1.3.4 Hysteresis Stability

Due to the fact that the hysteresis is not a continuous function, care has to be taken during tuning to ensure that as the SOC current reaches very low values that the value of $s_k M(SOC_k)$ does not become unstable. Recall that from equation 7, s_k changes with current based on the value of ε. It is important to ensure stability by using a sufficiently small value of ε. By reducing the value, the model tends to be stable despite the discontinuous nature of the hysteresis function. Figure 43 shows the hysteresis function as the current switches from positive to negative values.

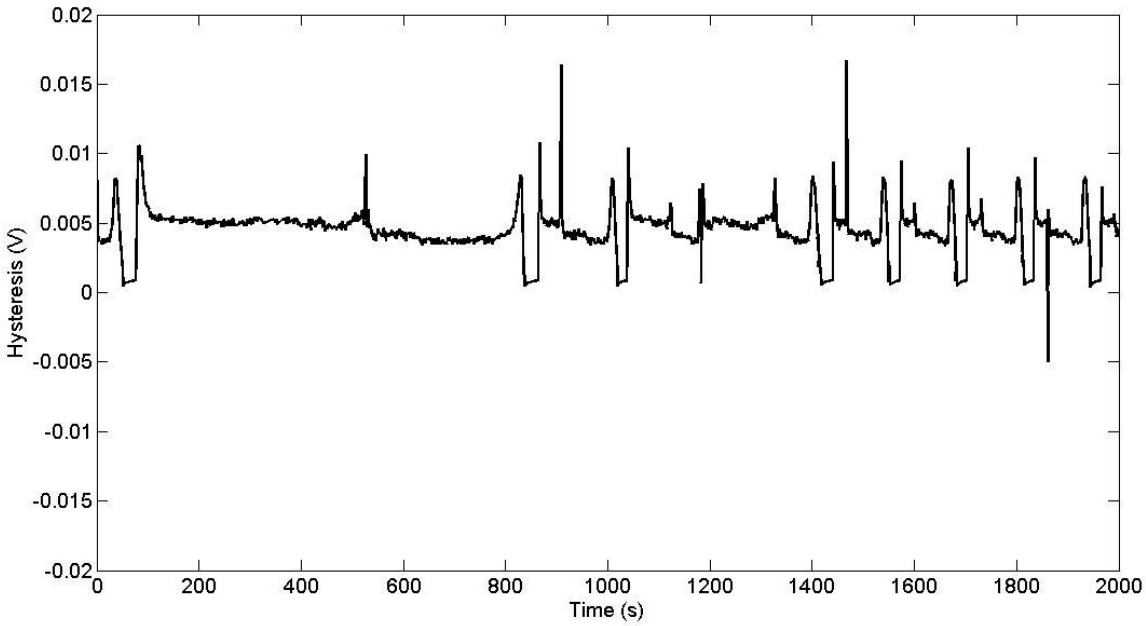

Figure 43: Sample of Hysteresis Voltage During Cycling

4.2 Capacity Considerations

As defined in the background review, battery state of health (SOH) can change rapidly over the life of a battery due to a number of reasons including, but not limited to, calendar life, cycle life, temperature, stored voltage, etc. The main degradation mechanism that is of concern here is the battery's cycle life and trying to estimate it during operation. State of health is broken into two parameters; battery capacity and battery power availability. Capacity fade is of primary concern in $LiFePO_4$ since power availability is generally quite high [44]. Therefore, a capacity estimator is required on-board the battery test stand in order to better approximate state of charge over the life of the batteries being tested.

Ning has proposed a generalized capacity model[40]. The model developed was a 1-D analytical model of capacity fade under light loads (1C and 0.5C). The model was complicated and time intensive to compute, so in 2008 Stevens utilized test data to develop a 0-D empirical model based on the Ning generalized model that includes accelerating factors for temperature and SOC swings while minimizing computing time [44]. The result was a model that could be used with a duty cycle to estimate cycle life. The model developed has the following form:

$$c_s^0|_{N+1} = c_s^0|_N + \frac{Q_s}{F\varepsilon_s} \qquad \text{equation 63}$$

Where:

$c_s^0|_N$ is the concentration of lithium at the anode at time N

Q_s is the volume-average loss of cylable lithium

F is Faraday's number = 96487 $\frac{C}{mol\ e^-}$

and ε_s is the volume fraction of the solid phase in the anode

Steven's model includes accelerating factors for both SOC swings and temperature changes and also a power fade mechanism based on the increase of resistance due to a build up of the

SEI layer. The important mechanism for the purpose of this work is the loss of cyclable lithium due to swings in SOC. It should be noted that temperature will also play a role in the loss of capacity, to a lesser degree, and can be added in for an increase in model fidelity. Note that capacity does change significantly with temperature, but this is not a permanent change in capacity and thus not considered a change in state of health (but still could be accounted for).

Therefore, from Ning

$$Q_s = \left| \int_{t=0}^{t=t_{para}} j_{para} a_{s,n} dt \right| \qquad \text{equation 64}$$

Where:

j_{para} is the flux caused by the parasitic reaction (A/m^2)

$a_{s,n}$ is the specific interfacial area of the porous, negative electrode (m^2/m^3)

The discrete version of the above equation is as follows assuming rectangular integration (zero order hold):

$$Q_{s_n} = \left| j_{para_n} a_{s,n} \Delta t \right| + Q_{s_{n-1}} \qquad \text{equation 65}$$

Stevens work focussed on the j_{para} term in the above equation. j_{para} follows a Tafel relationship as shown in equation 66.

$$j_{para} = j_{para}^0 exp\left(\frac{\alpha_c F}{RT}\varphi\right) \qquad \text{equation 66}$$

Where:

j_{para}^{0} is the base parasitic flux

φ is the overpotential of the cell

The overpotential can be determined by subtracting the OCV at the current SOC from the voltage measurement from the SOC EKF.

Stevens adapted the model to be:

$$j_{para} = \propto_{SOC}^{n,ave} \propto_{Temp}^{n,ave} j_{para}^{0} exp\left(\frac{\alpha_c F}{RT}\varphi\right) \quad \text{equation 67}$$

For the purposes of modeling degradation due to cycling, only the SOC accelerating factor will be utilized. The SOC accelerating factor is defined as follows:

$$\propto_{SOC}^{n,ave} = 0.01 \times (1 + \beta_1 \times \propto_{SOC}^{n})^{z_2} + 0.99 \times \propto_{SOC}^{n-1,ave} \quad \text{equation 68}$$

And:

$$\propto_{SOC}^{n} = exp\left(\frac{-100}{abs(60 - SOC_n)}\right) \quad \text{equation 69}$$

With the model fitting parameters in the following table:

Table 2: Stevens Model Fitting Parameters

Parameter	Value
β_1	2
z_2	4
j^0_{para}	0.00000008
α_c	0.5

Therefore, the Stevens model is undefined when SOC = 60%. In order to ensure that the model is stable, a small value is added to the SOC in the instance that SOC == 60%. The value chosen here was 0.1%. Since the function has such a long time constant, a difference of 0.1% for the one time step will not create a noticeable effect. Figure 44 shows the value of Q_s as the SOC passes through 60%.

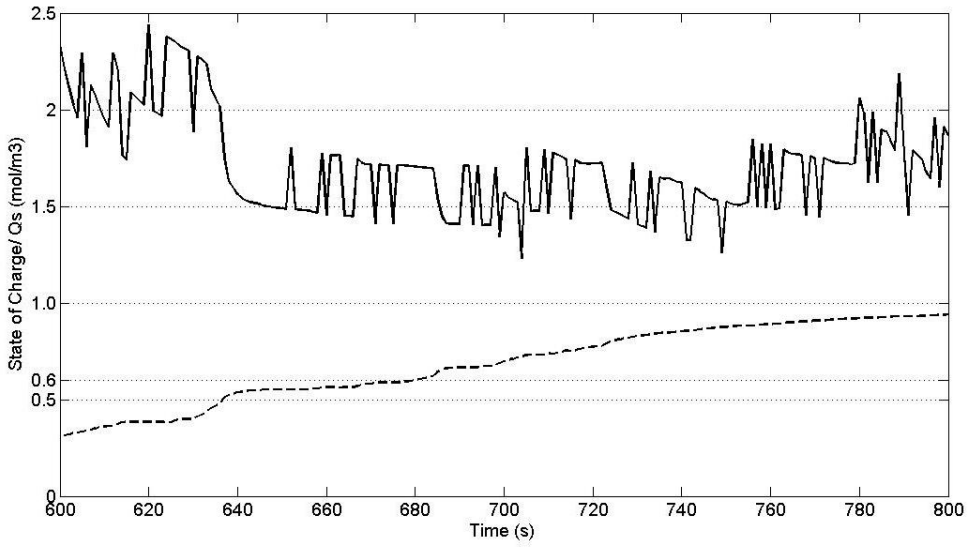

Figure 44: Sample of Volume Average Capacity Loss Through 60% SOC

4.2.1 Dual EKF vs 2 State EKF

Plett suggested in [54] that the capacity EKF be a separate EKF than the SOC EKF to avoid large matrix calculations. Plett's original idea was to utilize the SOC as a measurement in the measurement model for capacity. The idea presented here is that the SOC can be used as a control input for the second EKF and the error estimation is based on the error associated with the SOC estimation and the measurement model is driven by construction to be zero based on the capacity update and SOC estimation. Figure 45 shows a modification of what Plett suggested.

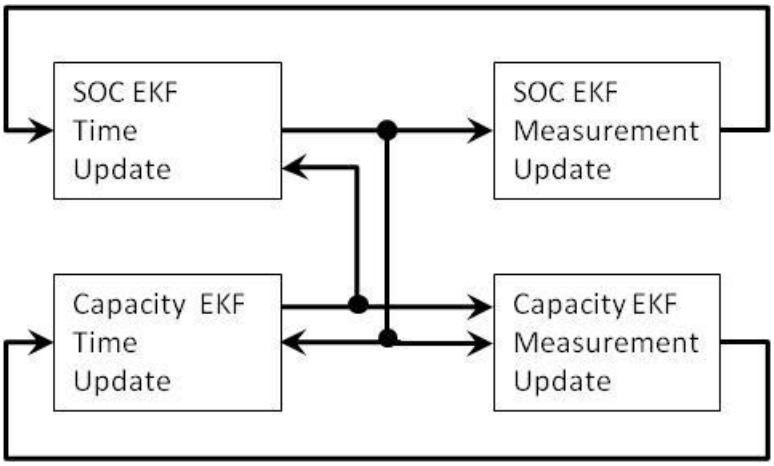

Figure 45: Schematic Representation of Dual Extended Kalman Filter

4.2.2 EKF using Stevens Model

In order to develop an EKF for the Stevens model, the process model and measurement model must be defined.

4.2.2.1 Process Model

The process model of interest here is the reduction in capacity of the cell which is directly related to the loss of lithium due to the parasitic reaction. The process model then is:

$$Capacity_k = Capacity_{k-1} - Q_s V + m_k$$ equation 70

Where

m_k is the process noise, assumed to be zero mean, white noise with a Gaussian distribution.

V is the volume of the solid anode

4.2.2.2 Measurement Model

The measurement model is the same measurement model that Plett used and is a modification of the SOC model, constructed to drive the measurement to zero in order to allow for the slow dynamics of the capacity change.

$$d_k = SOC_k - SOC_{k-1} + \frac{\eta i_k \Delta t}{Capacity_k} + h_k$$ equation 71

Where:

h_k is the measurement noise, assumed to be zero mean, white noise with a Gaussian distribution.

For the EKF implementation, the Stevens model employs just one state, again making the implementation of the EKF relatively straight forward. Specifically, since the process model loss of lithium term is not a function of capacity, A_{k-1} reduces to 1. Therefore, the error covariance time update is a simple step that reduces to:

$$\Sigma^{-}_{\tilde{x},k} = 1 \times \Sigma^{+}_{x,k-1} \times 1 + \Sigma_w$$ equation 72

Essentially, the error covariance time update just adds the covariance of the process noise estimate each time. Also, since A_k and C_k are both one term matrices, all of the transposes required are just scalars, so the covariances are both relatively easy to compute.

Recall:

$$\hat{C}_k = \left.\frac{\partial g(x_k, u_k)}{\partial x_k}\right|_{x_k = \tilde{x}_k} \qquad \text{equation 73}$$

Since the only term that is a function of capacity is the SOC tracking term in the measurement model, C_k reduces to:

$$\hat{C}_k = \frac{-\eta i_{k-1} \Delta t}{Capacity_{k-1}} \qquad \text{equation 74}$$

4.2.3 EKF Using Plett Model

Plett also proposes a model for generic battery capacity estimation. The measurement model for the Plett model is the same as with the Stevens model, however the process model is simply a pass through of the capacity from the time step before. Therefore, all of the change in capacity is due to the white noise estimation, or the error covariance. The general framework from the Stevens model still applies for the Plett model, however, the $Q_s V$ term is removed.

Therefore the Plett process model is:

$$Capacity_k = Capacity_{k-1} + m_k \qquad \text{equation 75}$$

Although the model considers the long time constant of the battery degradation, it considers little regarding the main degradation factor (swings in SOC). The benefit of the Plett model is that it is very easy to implement.

4.2.4 Stevens Model Process Noise Implementation

The variance of the capacity with respect to process noise of the Stevens Model is difficult to determine given the non-linearity of the model. Since there are two sources of process noise in the Steven Model, SOC and the voltage measurement associated with the overvoltage calculation, the variance estimation is quite difficult. The variance would be:

$$\sigma^2_{Capacity} = \left(\frac{\partial Cap}{\partial SOC}\right)^2 (\sigma^2_{SOC}) + \left(\frac{\partial Cap}{\partial y}\right)^2 (\sigma^2_y) \quad \text{equation 76}$$

Looking at the variation due to SOC:

$$\frac{\partial Cap}{\partial SOC} = 0 - V\frac{\partial Q_s}{\partial SOC} \quad \text{equation 77}$$

And:

$$\frac{\partial Q_s}{\partial SOC} = a_{s,n}\Delta t\frac{\partial j_{para}}{\partial SOC} \quad \text{equation 78}$$

$$\frac{\partial j_{para}}{\partial SOC} = j^0_{para}\left[exp\left(\frac{\alpha_c F}{RT}\varphi\right)\frac{\partial \propto^{n,ave}_{SOC}}{\partial SOC} + \propto^{n,ave}_{SOC}\frac{\partial}{\partial SOC}\left(exp\left(\frac{\alpha_c F}{RT}\varphi\right)\right)\right] \quad \text{equation 79}$$

First, the derivative of $\propto_{SOC}^{n,ave}$ with respect to SOC is determined. Since $\propto_{SOC}^{n,ave}$ contains the |60-SOC|, the derivative will be computed twice, once for the case that the SOC>60 and once for the case that the SOC<60.

$$\left.\frac{\partial \propto_{SOC}^{n,ave}}{\partial SOC}\right|_{SOC>60} = \frac{8}{(60-SOC)^2}\left(1+2\exp\left(\frac{-100}{60-SOC}\right)\right)^3 exp\left(\frac{-100}{60-SOC}\right) \quad \text{equation 80}$$

And

$$\left.\frac{\partial \propto_{SOC}^{n,ave}}{\partial SOC}\right|_{SOC<60} = \frac{-8}{(SOC-60)^2}\left(1+2\exp\left(\frac{-100}{SOC-60}\right)\right)^3 exp\left(\frac{-100}{SOC-60}\right) \quad \text{equation 81}$$

For the case that SOC = 60% exactly, the SOC will be incremented by 0.1% so that the derivative will exist. Since this is an estimate of process noise and the time constant is so long, the small error in SOC when it hits 60% can be neglected.

For the derivative of $exp\left(\frac{\alpha_c F}{RT}\varphi\right)$ with respect to SOC, the overpotential equation needs to be substituted into equation 78:

$$\frac{\partial}{\partial SOC}\left(exp\left(\frac{\alpha_c F}{RT}(y-OCV(SOC))\right)\right) = \frac{\partial OCV(SOC)}{\partial SOC}\frac{\alpha_c F}{RT}(y-OCV(SOC))exp\left(\frac{\alpha_c F}{RT}(y-OCV(SOC))\right) \quad \text{equation 82}$$

The derivative of OCV(SOC) can be determined using central differencing.

Determining the $\frac{\partial Cap}{\partial y}$ derivative:

$$\frac{\partial Cap}{\partial y} = -V\frac{\partial Q_s}{\partial y}$$ equation 83

And:

$$\frac{\partial Q_s}{\partial y} = \frac{\partial}{\partial y}\left(j_{para_n}\right) a_{s,n}\Delta t$$ equation 84

$$\frac{\partial}{\partial y}\left(j_{para_n}\right) = \propto_{SOC}^{n,ave} \frac{\alpha_c F}{RT}\left(y - OCV(SOC)\right) exp\left(\frac{\alpha_c F}{RT}\left(y - OCV(SOC)\right)\right)$$ equation 85

With all of the derivatives substituted into equation 84, the final process variance model is completed. Now the process variance can be estimated in real time using data from the SOC EKF. The final process noise will use the above model for estimation and then tune to fit the lifetime data.

The above noise was simulated using data from the SOC EKF testing and the variance was logged. After compiling the data, the variance was averaged as the mean process data. The mean process variance was $9.9 \times 10^{-2} As$. In order to reduce complexity and to improve computational efficiency, the average value was used as a constant in future testing and simulation.

4.2.5 Tuning the Stevens Model Capacity EKF

The capacity EKF tuning process differs slightly from the SOC EKF tuning process, since the measurement model is constructed to always measure zero. Therefore, the process noise will be set to the value determined above, and the measurement noise will be tuned to fit the known capacity degradation rate and to ensure convergence of the model.

4.2.6 Estimating Measurement Noise

The initial measurement noise estimate can be determined by calculating the variance in the SOC estimation from the SOC EKF. As previously discussed, the variance in the SOC was calculated to be 1.5%. Therefore, to determine the variance in the variable d_k can be completed as follows:

$$\sigma_d^2 = \sigma_{SOC,EKF}^2 + \sigma_{SOC,Current}^2 \quad \text{equation 86}$$

Recall:

$$\sigma_{SOC,Current}^2 = 1.3 \times 10^{-10} \quad \text{equation 87}$$

Therefore, the variance becomes:

$$\sigma_d^2 = (0.015)^2 + 1.3 \times 10^{-10} = 2.3 \times 10^{-4} \quad \text{equation 88}$$

This variance was placed in the model and the model was tested to ensure convergence. Results of the testing are shown in the error analysis section.

4.2.7 Tuning the Plett Model Capacity EKF

The Plett model EKF requires a slightly different tuning process. As discussed, the measurement model is the same as the Stevens Model EKF. It is important to understand is that the Plett measurement model will drive most of the degradation since the process model attempts to set the capacity to the previous capacity estimate and is allowed to change due to the noise associated with it. Therefore, the measurement model is initially set the same as the Stevens model and the process noise is increased or decreased to ensure convergence and to fit the model to the measured data.

4.3 Capacity Testing and Tuning

The EKF was tested over 900 cycles of 30A discharges and 10A charges. Figure 46 shows the final capacity degradation curve from the Stevens Model.

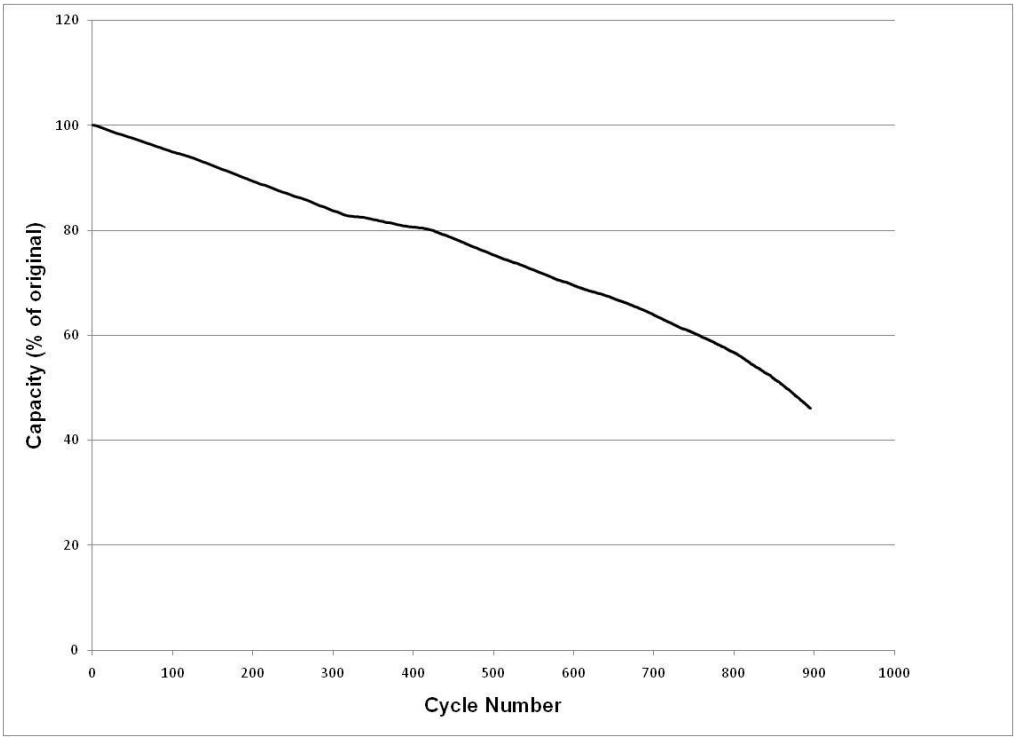

Figure 46: Stevens Model Capacity Test Data

The Plett model was also simulated over the same cycles and the results are shown in Figure 47.

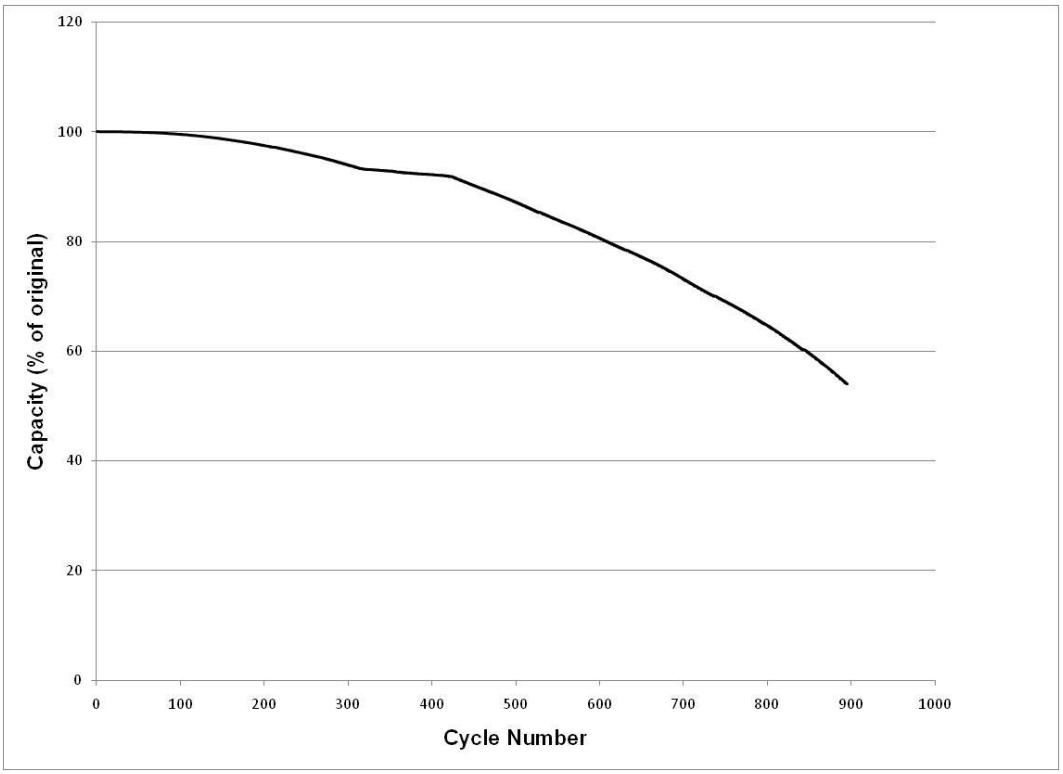

Figure 47: Plett Model Capacity Test Data

The actual capacity tests completed during cycling were analyzed and have been plotted next to both the Plett model and the Stevens model on Figure 48.

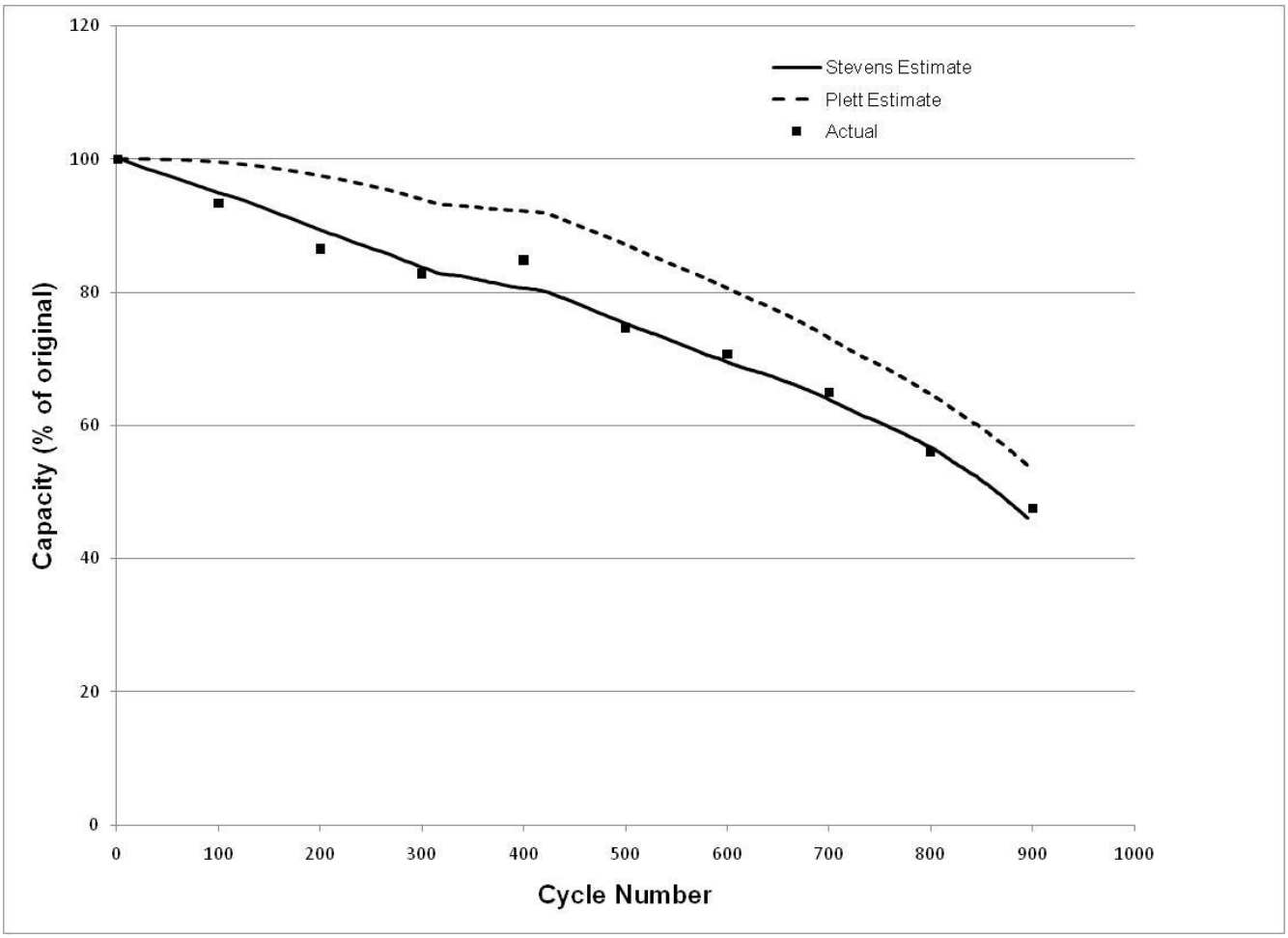

Figure 48: Comparison of Capacity EKF Algorithms

It can be seen that the Stevens model corresponds much more closely to the actual data than the Plett model. This is due to the fact that the Plett model has a much slower response since it is relying completely on the measurement model as opposed to having a predictive process model like the Stevens model.

After the Stevens model was properly tuned, the full dual EKF was tested to ensure that it was properly compensating for the reduced capacity in the SOC EKF. Figure 49 shows how the inclusion of the capacity EKF has strengthened the robustness of the SOC EKF over the lifetime of the cycles.

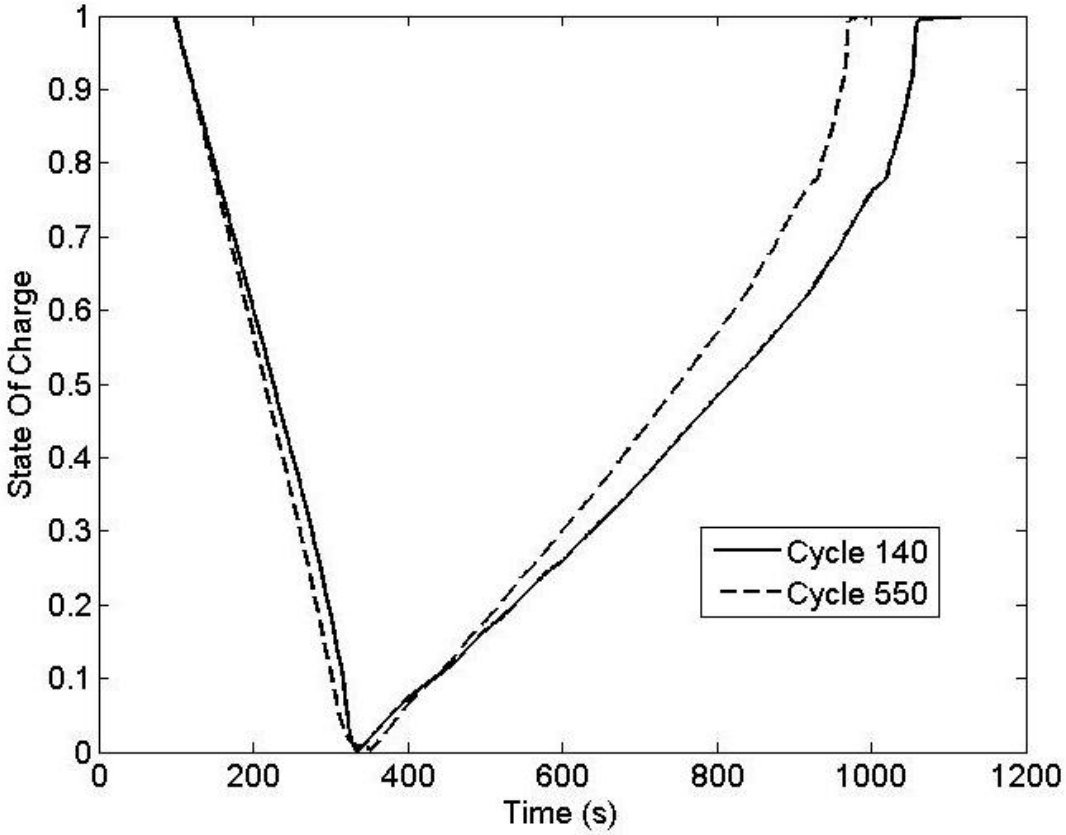

Figure 49: Cycle 550 and Cycle 140 Overlay Showing SOC Estimation with Capacity Adjustment

It can be seen from Figure 49 that although the cycle is shorter due to the capacity degradation, the SOC model now accurately predicts that the high and low SOC.

4.4 Simulation of Certification Drive Cycles

The final EKF algorithm was simulated versus a battery model with introduced Gaussian noise to determine its ability over an FTP cycle to track actual SOC. The simulation enables an understanding of what "true" SOC is for the battery as well as "true" current and voltage measurements.

For the simulations, a battery was sized appropriately for a midsize car and then an electric only FTP was simulated to test for accuracy. The battery was based on the same cells tested and sized by the following procedure:

In general the voltage of motors for vehicles is between 300 V – 400 V. For the purposes of this simulation the voltage was set to 363 V (110 cells in series). A midsize car utilizes approximately 2.4 kWh over an FTP schedule. Each string of 110 series cells would yield 0.835 kWh of energy.

Therefore, the battery pack was designed to have 4 parallel strings of 110 cells each for a total of approx 3.3 kWh. It is important to understand that the battery pack design considerations here are merely an estimate and do not require accuracy to any real battery pack. The purpose is to simply come up with a reasonable estimate of current and voltage measurements on one cell over the course of an FTP cycle. Also a battery management system within an actual pack will be further complicated with cell voltage balancing, and thermal effects of the pack configuration.

A standard road load was used with a 1Hz FTP drive cycle to determine the power required by each parallel string of cells. It is assumed that there is perfect voltage balancing between cells and that each cell sees the exact same current load. A PI model was used and tuned to meet the power requirements. Each time step the model uses the power divided by the voltage from the previous time step to determine a current request based on the PI parameters. The current request is fed into the coulomb counting model to determine the true SOC at the time. The

SOC is then passed to the voltage model and based on the current and SOC, a voltage (including hysteresis) is output for the current calculation from the next time step.

On the output of the current and voltage signals from the model, there is a Gaussian noise generator block that is included in Simulink. The block is set to have the noise calculated in the process and measurement variance above. The Excel sheet model parameters are included in Appendix D and the code for the battery model is included in Appendix E. The current required by the cell for the FTP test is included in Figure 50 showing the actual current.

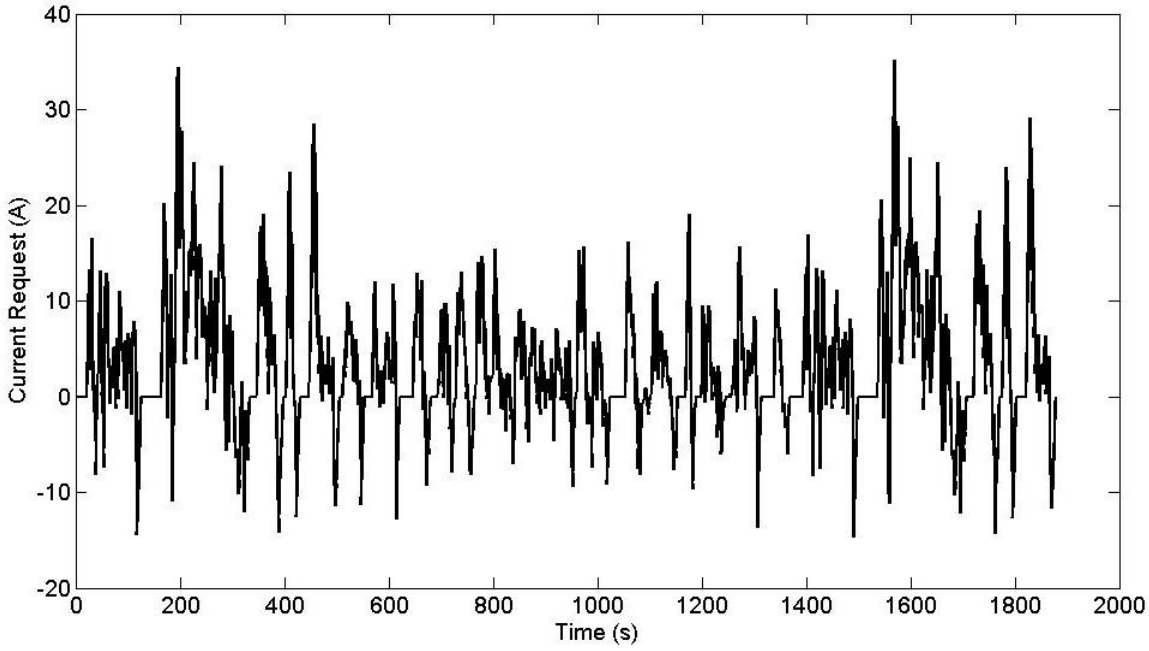

Figure 50: FTP Current Cycle per Battery Cell

Figure 51 shows the results of the FTP test (SOC Actual is derived from the plant model, SOC Estimate is the result of the EKF)

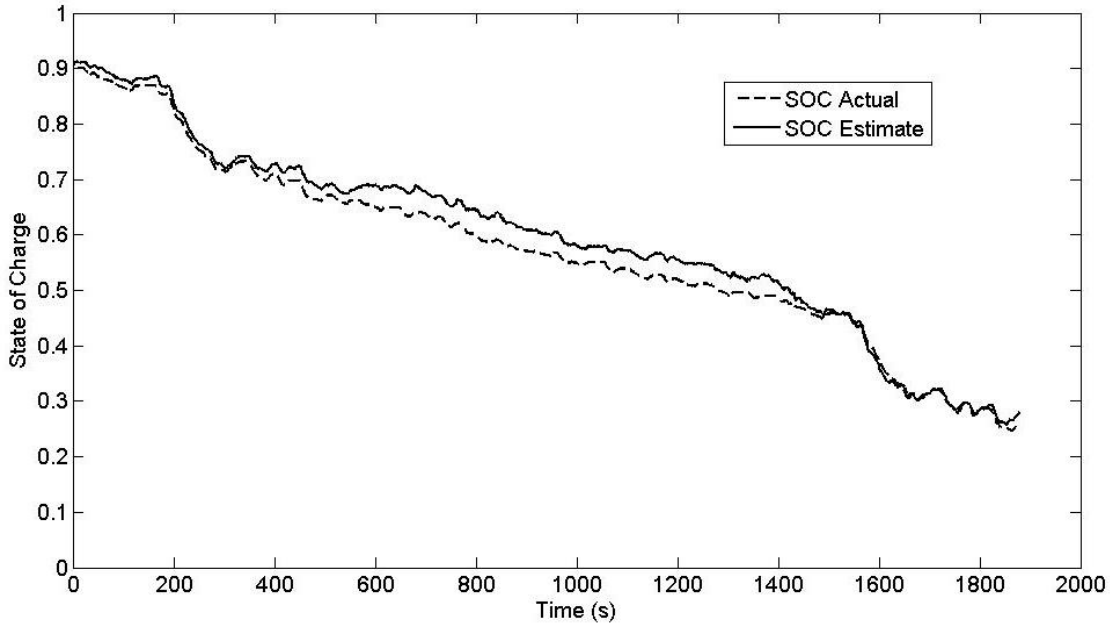

Figure 51: Simulated SOC Tracking During an FTP Cycle

As shown, the model estimates SOC well through the entire dynamic cycle with some error in the middle of the SOC range. Since the process noise was artificially increased in order to stabilize the SOC as discussed previously, it is expected that there would be some error in the mid-range SOC.

4.5 Error Analysis

4.5.1 SOC Error Analysis

One of the benefits of using the EKF is that the error bounds for the model are readily available for analysis. Every iteration of the EKF updates a process covariance, or in the case of only one state, a variance of the system. Therefore, the variance can be used to determine a confidence interval for the EKF itself. Determining the confidence interval is relatively straight forward using the assumption that errors in the state have a Gaussian distribution.

The square root of the process variance is equal to the standard deviation of the process by definition. Therefore, the confidence interval can be setup based on how many standard deviations from the mean (or the estimate in this case) the error bounds are set up for.

For the SOC tracking, a confidence interval of 95% was used, which corresponds to 2.6 standard deviations from the mean. The square root of the variance was taken at each time step and was multiplied by 2.6. Figure 52 shows the estimate of SOC for a 30 discharge and 10A charge cycle graphed with the upper and lower error bounds for the 95% confidence interval.

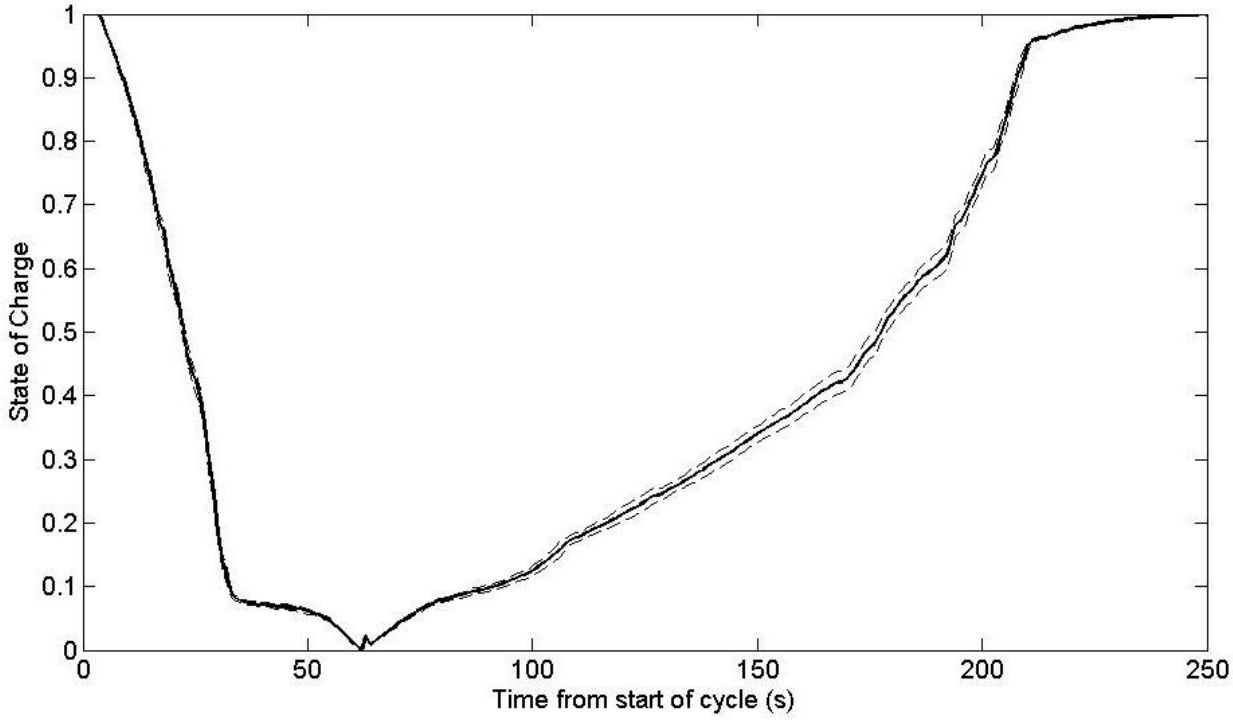

Figure 52: Representative SOC Error Estimation for Constant Current Charge and Discharge

As the figure shows, the error is at a maximum in the range of approximately 30% to 60% SOC. This is due to the fact that the measurement model is so inaccurate during the mid-range SOC since the open circuit voltage curve varies so little with SOC. The error maximum is approximately 1.5% for the entire charge/discharge cycle. This is an acceptable error for the mid-range SOC since there is minimal control impact throughout the middle of the SOC range.

As noted above regarding tuning the measurement noise, the maximum of 1.5% error was sought after as an accuracy goal, which is what made the capacity model necessary.

4.5.2 Dynamic Cycle SOC Error Analysis

Since the hysteresis term used in the model is not a function of the change of SOC with respect to the change in time, of utmost concern is the operation of the filter over dynamic cycling. The constant current charge and discharge are not prone to instability due to the discontinuous

nature of the hysteresis loop. Therefore, the error analysis on the dynamic cycles is very important.

Figure 53 shows the operation of the filter over the FTP cycle with error bounds of a 95% confidence interval.

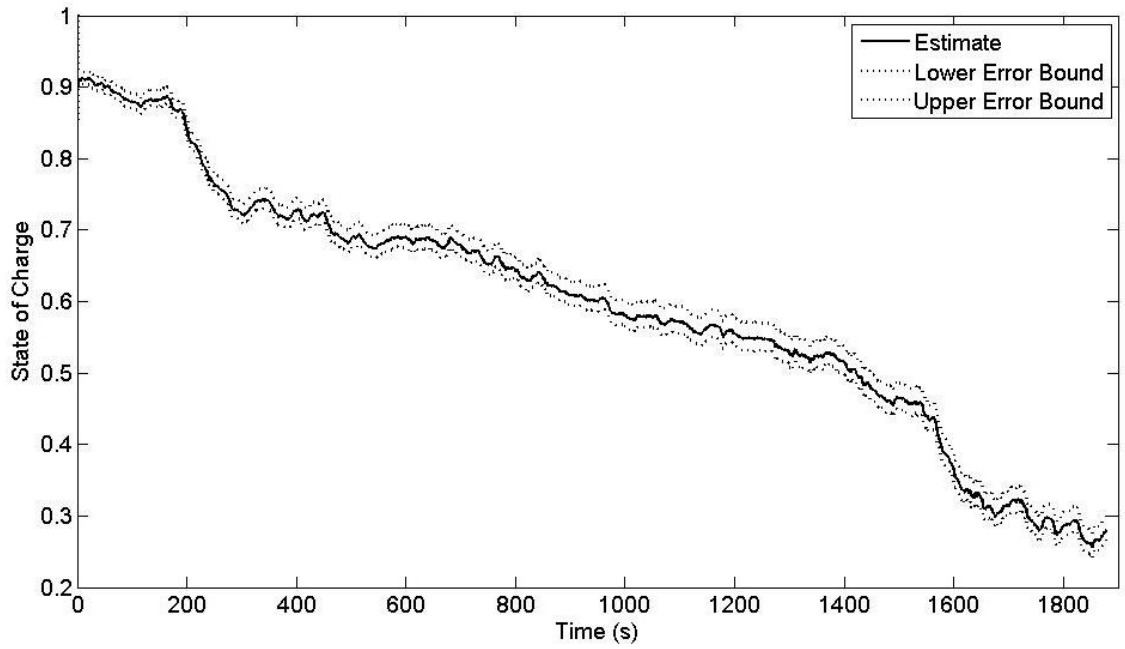

Figure 53: Simulated SOC Error Estimation Over FTP Cycle

The filter shows very good performance through the very dynamic cycle with the biggest errors appearing through the middle of the SOC range and during the most dynamic parts of the cycle, which happen to be the start and the end of the cycle.

Figure 54 shows the first 150 seconds of the cycle where the error bounds quickly converge on the correct SOC.

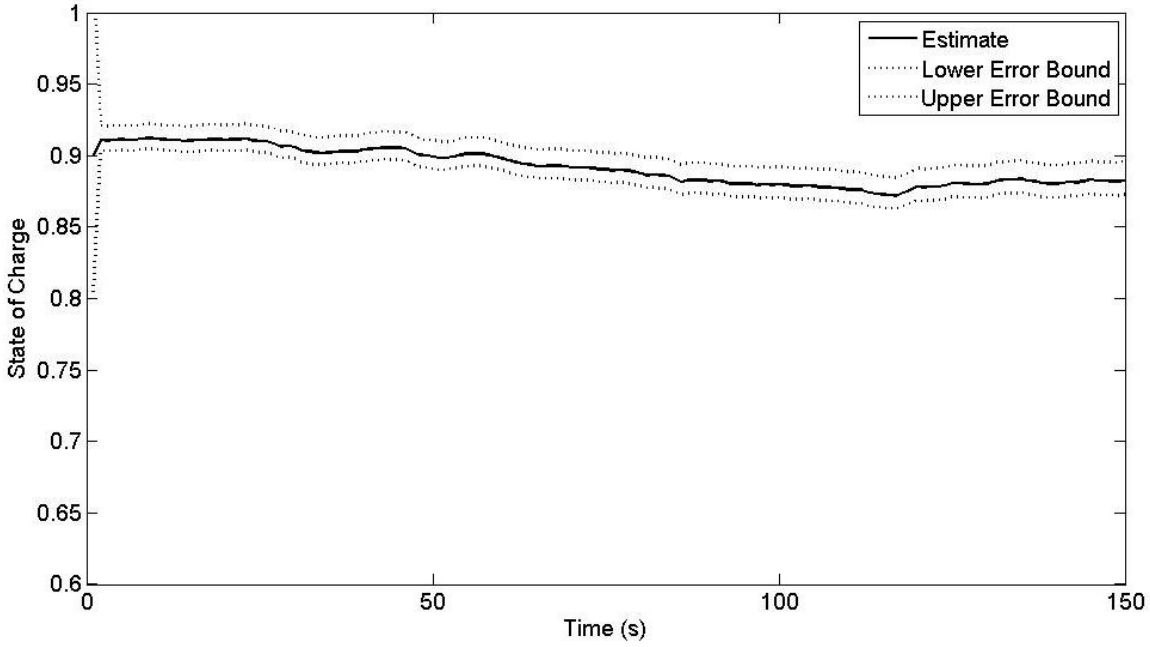

Figure 54: Close Up of Initial Error Convergence

The quick convergence proves that the filter is tuned adequately to handle large initial disturbances. The convergence means that there is rejection of the prior uncertainty in favour of the measured uncertainty, which is much smaller.

4.5.3 Capacity Error Analysis

A similar analysis is done on both capacity models. First, the Plett model shows that the error initially grows quickly since the model does not react well to the initial degradation, due to a lack of process model. The error then converges over a long period of time, however the overall error is quite high. Figure 55 shows the result of the simulation.

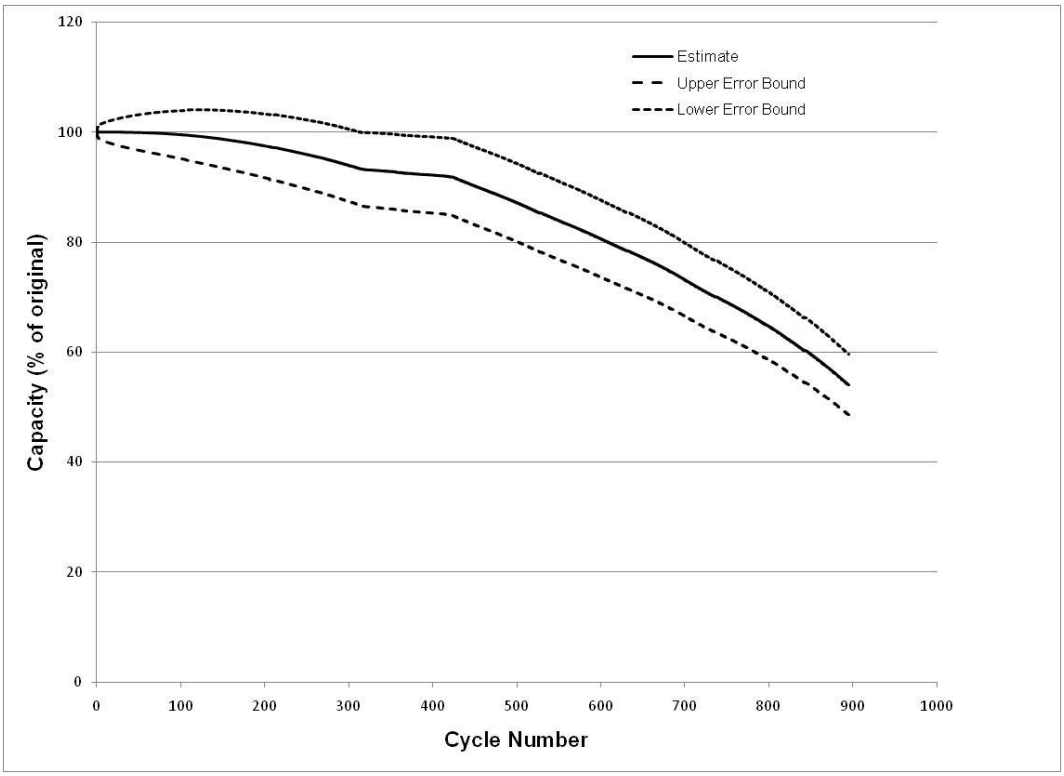

Figure 55: Plett Capacity EKF Error Estimation

It should be noted that Plett also mentions that the SOC needs to be very accurate in order for this model to be used. It is possible that the SOC is not accurate enough to catch the slight changes from cycle to cycle when relying so heavily on the measurement model.

Figure 56 shows the Stevens model with error bounds.

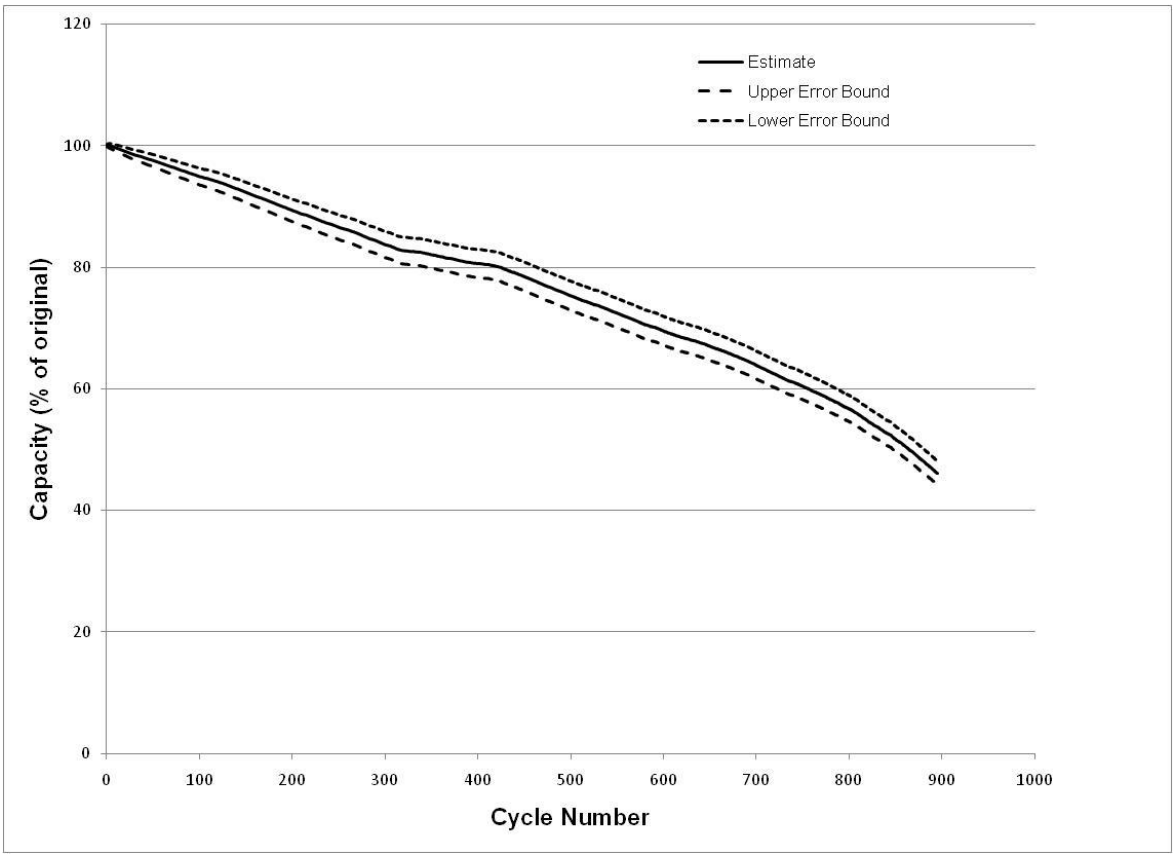

Figure 56: Stevens Model EKF Error Estimation

It is immediately clear the Stevens model error bounds are much smaller than the Plett error bounds.

5 Conclusions

5.1 Conclusions

This thesis describes the development of a dual Extended Kalman Filter for battery state estimation (SOC)of a single $LiFePO_4$ cell load and capacity cycled on a test stand at the University of Waterloo. The ability to track state of charge and capacity over the entire life of a battery enables the University of Waterloo to do dynamic lifetime testing on the battery test stand. The first goal of the state estimator was to provide accurate SOC estimation of the battery cell which was accomplished through the use of the EKF. The estimator tracks through continuous cycling and dynamic goals. The second goal of the estimator was to include error bounds for the SOC and capacity estimation for safety and reliability. The dual EKF estimates maximum and minimum errors at each time step to ensure the reliability of the estimator. Lastly a goal was to be simple enough for fast processing and ease of understanding. Since the state estimator includes just one state for SOC and one state for capacity, along with the description in this thesis, one should be able to understand the estimator and how it works for future tuning purposes, and application in vehicle models.

5.2 Recommendations

For future work, the University of Waterloo should do the following:

- Implement the estimator in the control of the hybrid test stand. The estimator so far has not been utilized for hybrid control on the test bench but in parallel utilizing data from the bench.
- Test the estimator over many urban and highway cycles to demonstrate robustness. Testing over many cycles with full depletion cycles in between will further demonstrate the robustness of the estimator.
- Implement new current and voltage sensors to improve filter errors. The sensor currently on the bench could be replaced with a current shunt and higher accuracy current sensor to improve the measurement noise contribution. The battery model

should be tuned to prismatic cells which have more potential in a vehicle. The battery model could also be improved with better temperature response. Including temperature in the battery model, the capacity of the cell can be tuned with respect to temperature. There is a realization that this may have only a marginal impact in a pack with a well designed thermal management system, as the cells will remain in a narrow range of temperature for most of their operation.

- Improve the voltage model to include an estimation of diffusion capacitance and charge transfer resistance which could potentially allow for a decrease in the voltage measurement noise model and improve the robustness of the model over life.
- In the long term an sigma-point or Unscented Kalman Filter (UKF)could be developed for a more accurate estimate of SOC.

Appendix A: Dual EKF Code for Test Stand Implementation

High Level EKF Algorithm

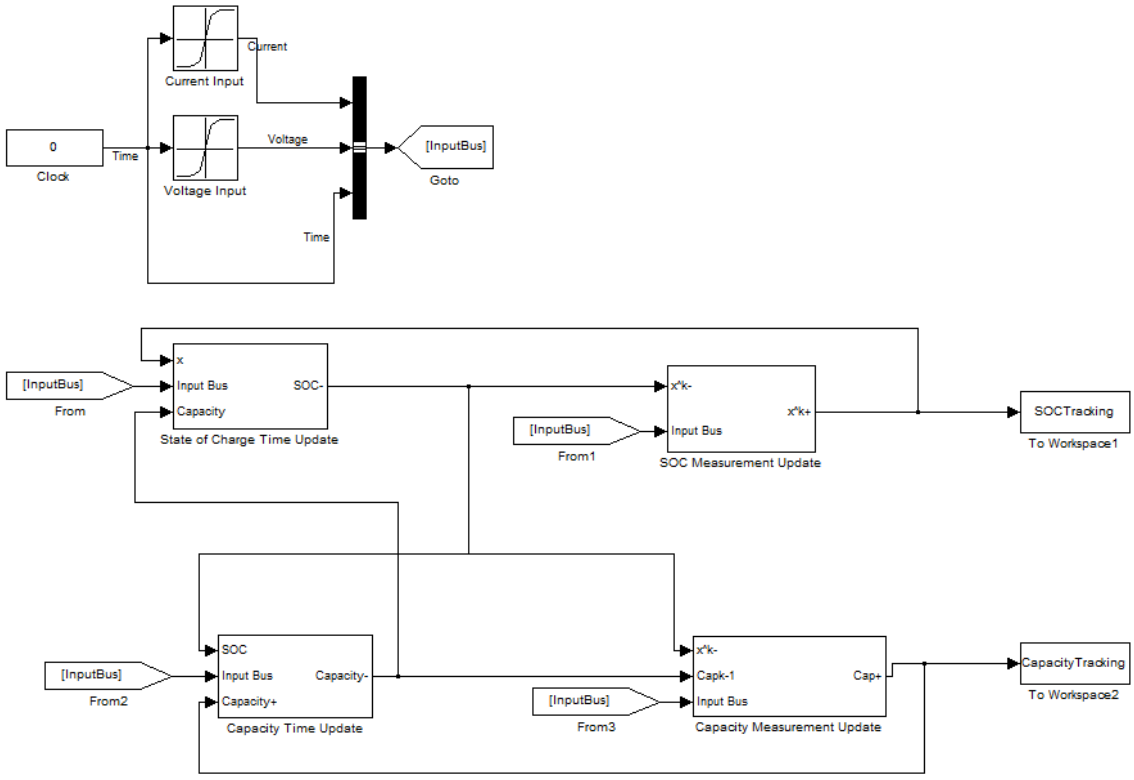

SOC Time Update

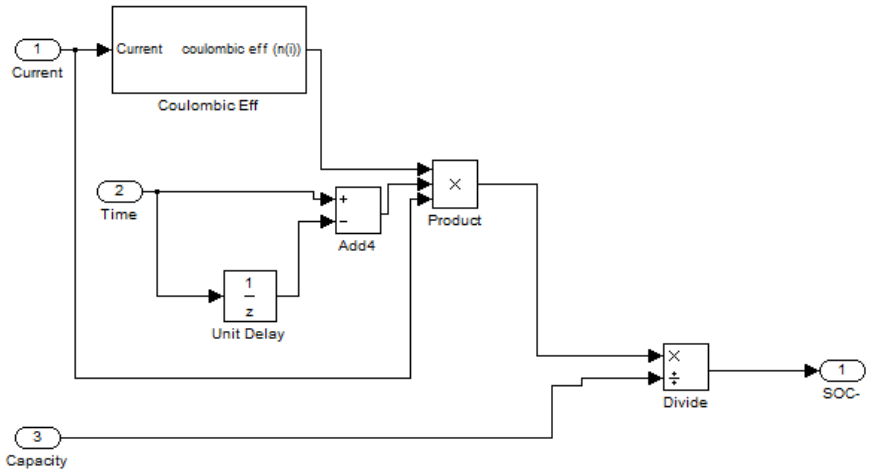

SOC Measurement Update

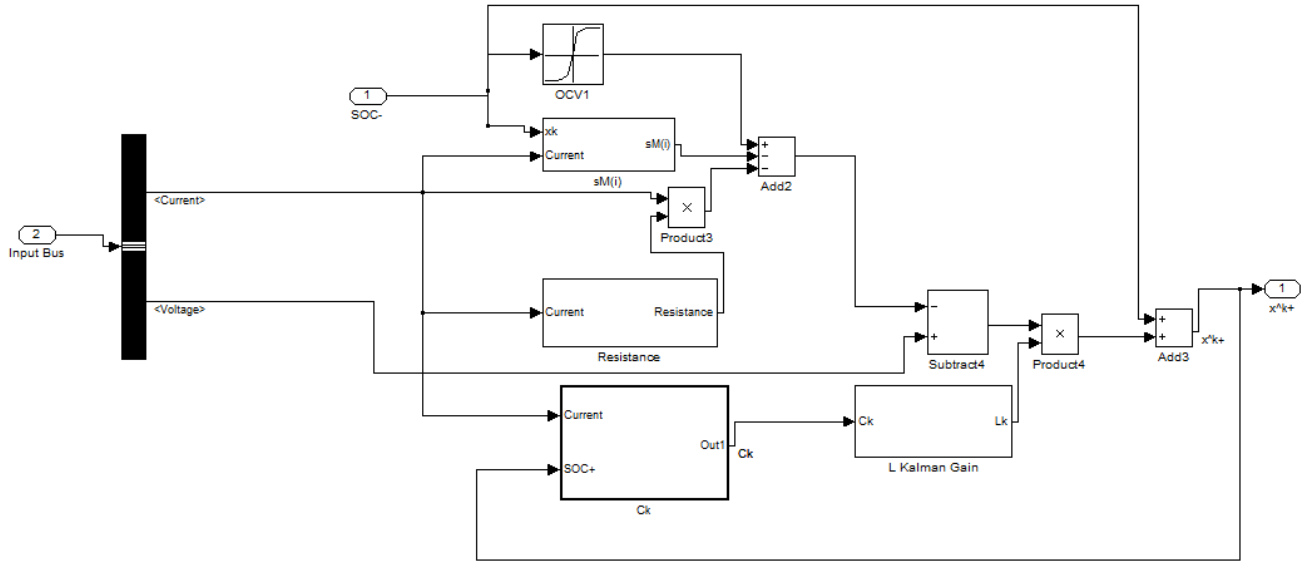

Hysteresis Code

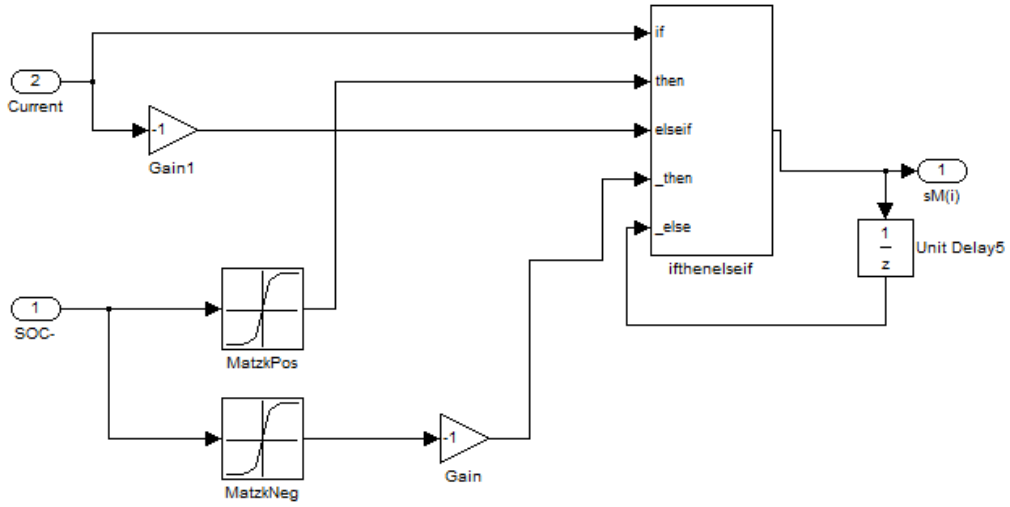
2
Current
-1
Gain1
1
SOC-
MatzkPos
MatzkNeg
-1
Gain
if
then
elseif
_then
_else
ifthenelseif
1
sM(i)
1
z
Unit Delay5

Ck Code

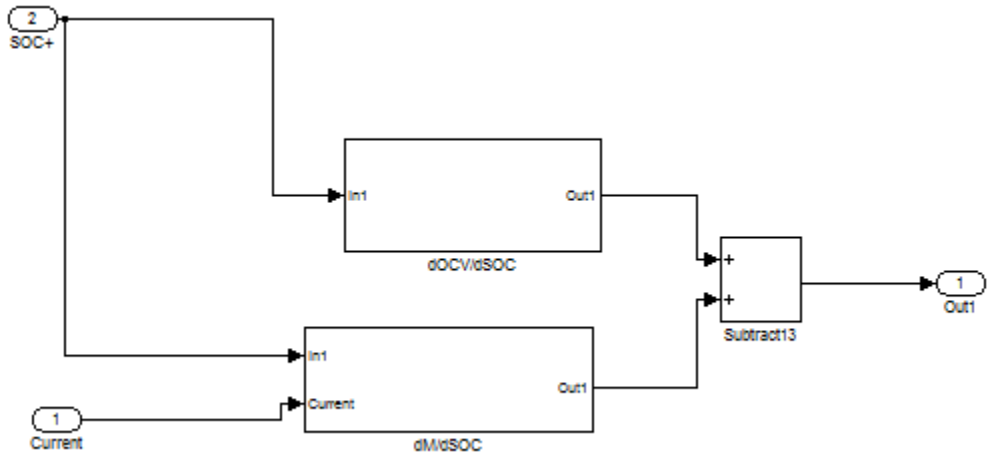
2
SOC+
In1
Out1
dOCV/dSOC
+
+
Subtract13
1
Out1
In1
Current
Out1
dM/dSOC
1
Current

Central Difference For dOCV/dSOC

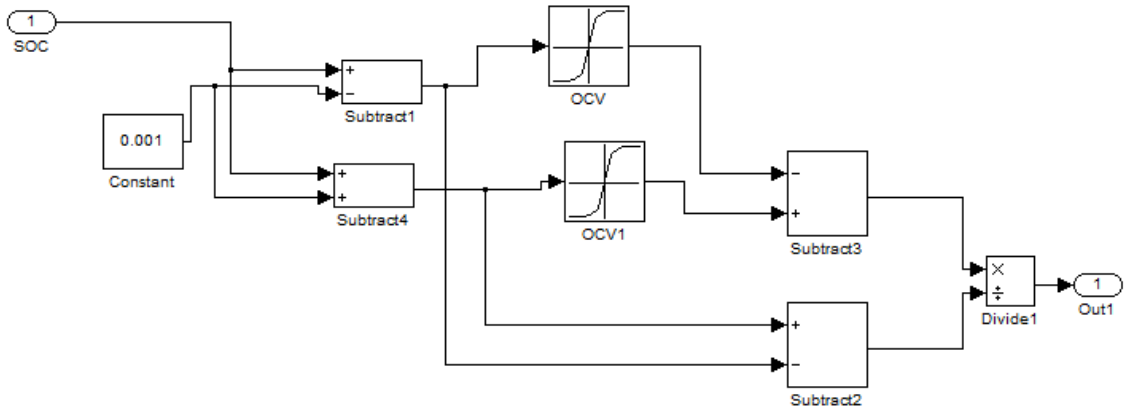

Central Differencing for dM/dSOC

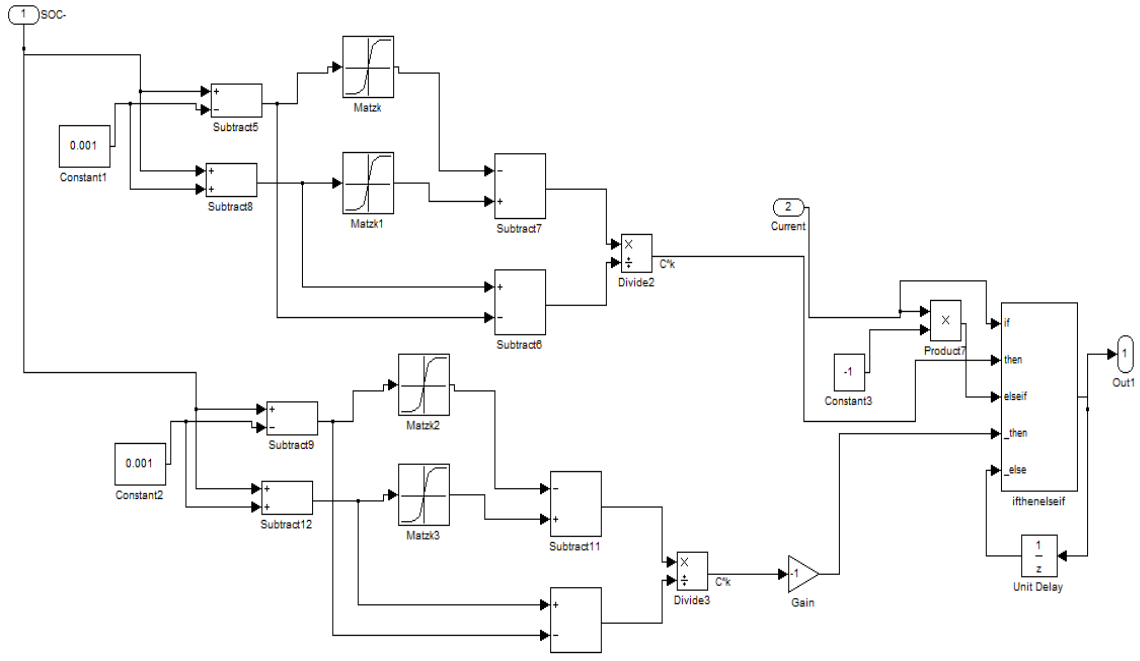

SOC Kalman Gain Code

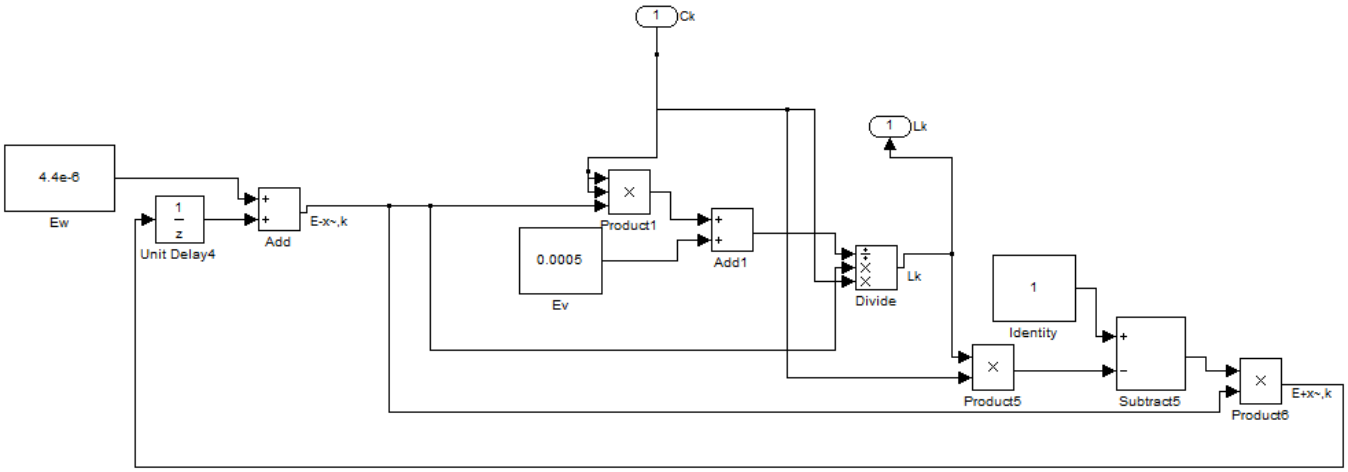

Capacity Time Update Code

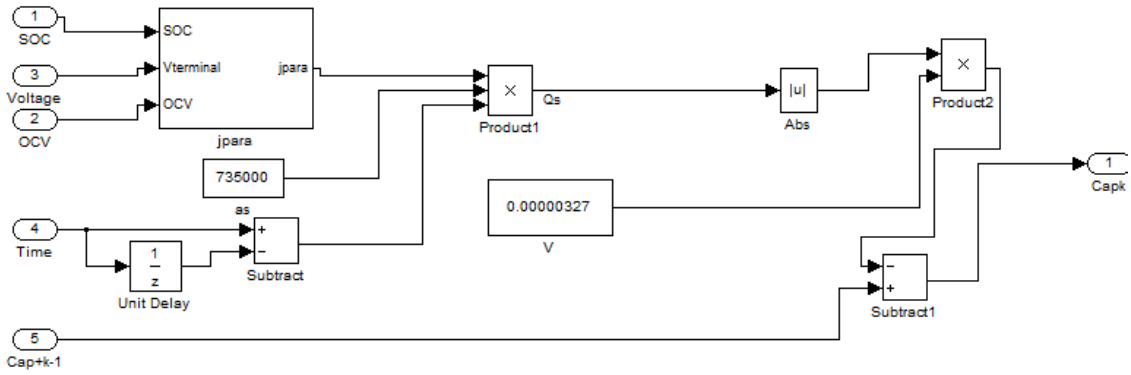

jpara Code

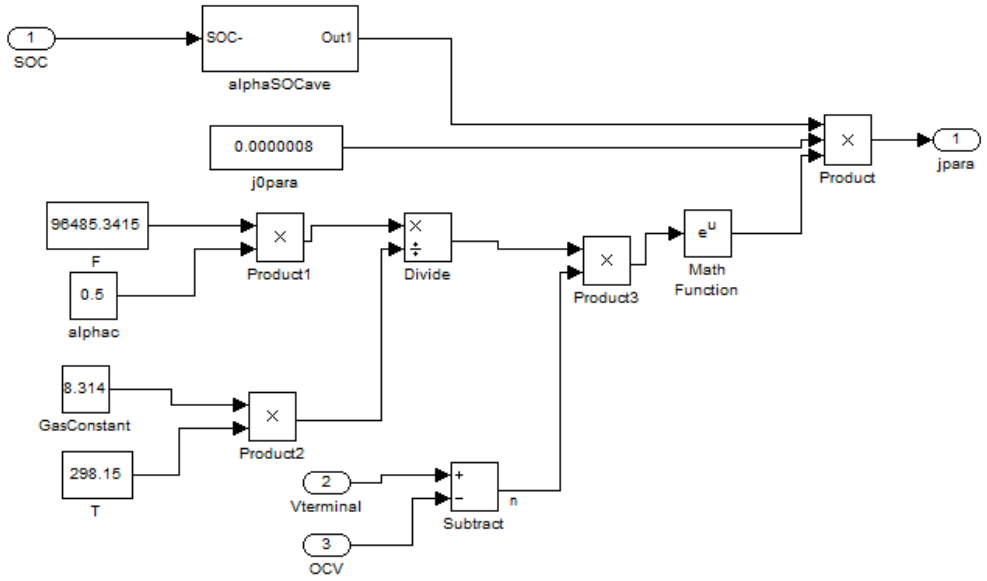

Alpha$_{SOC}$ Code

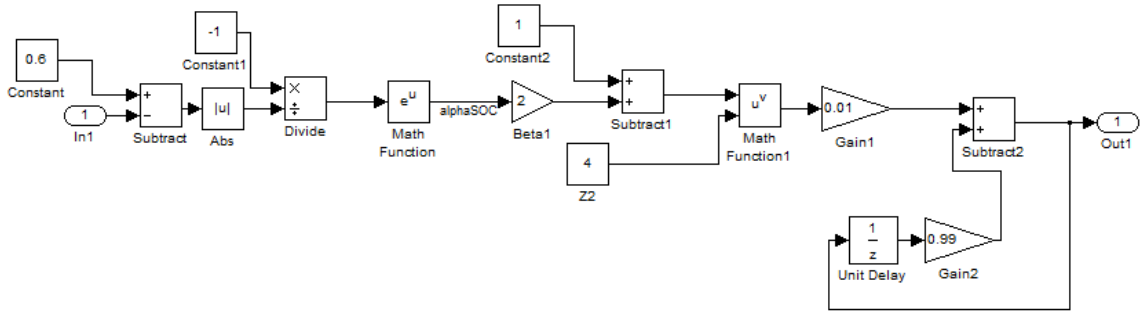

Capacity Measurement Update

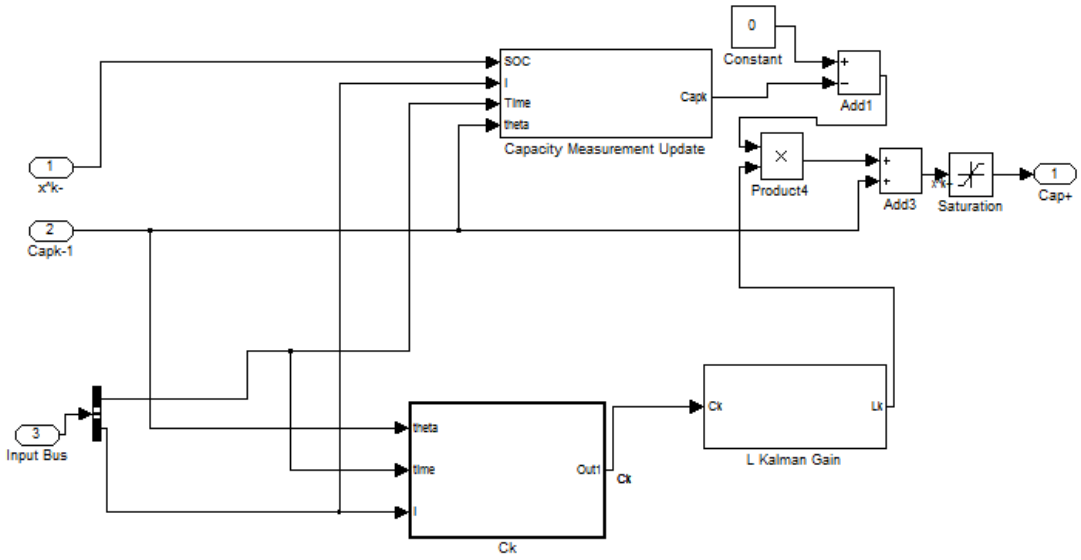

Capacity Measurement Update

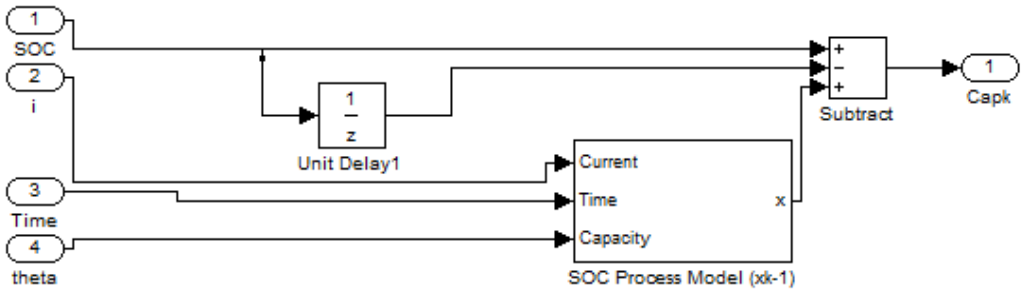

$dd_k/dCap$ for C_k of Capacity Model

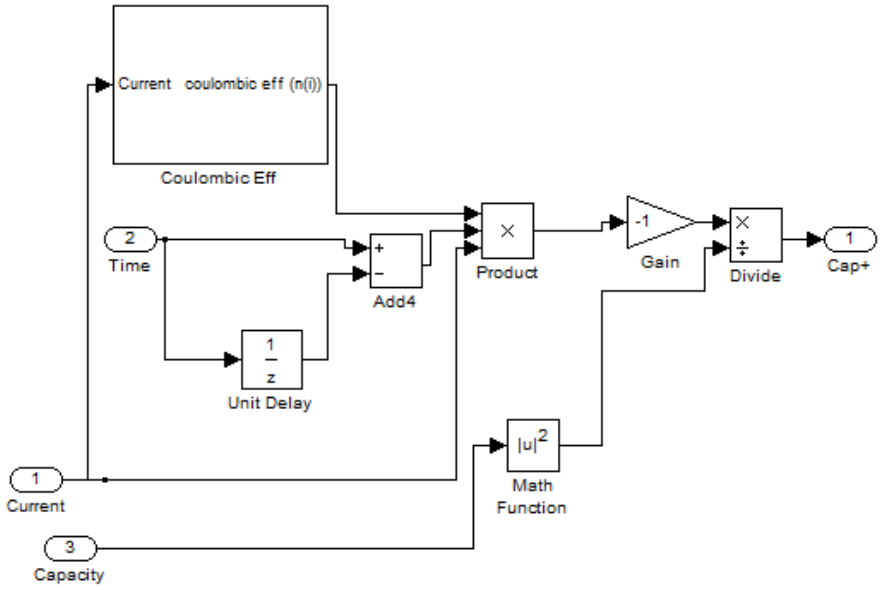

Capacity Kalman Gain Code

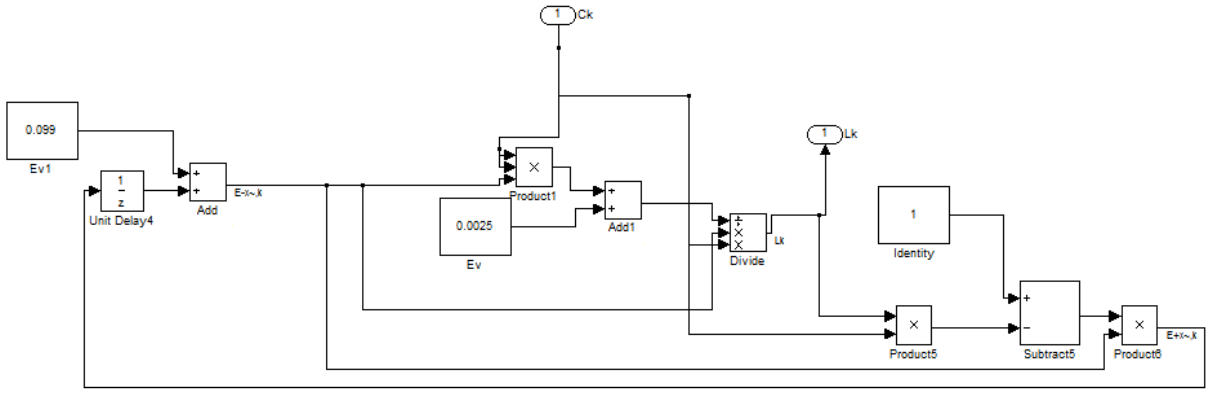

Appendix B: Open Circuit Voltage Curve Data

SOC	Voltage
0.00	2.09
0.00	2.60
0.01	2.78
0.02	2.90
0.03	2.98
0.05	3.08
0.06	3.12
0.07	3.15
0.08	3.19
0.10	3.23
0.12	3.25
0.14	3.26
0.16	3.26
0.18	3.28
0.20	3.29
0.22	3.30
0.24	3.30

SOC	Voltage
0.52	3.35
0.54	3.35
0.56	3.35
0.58	3.36
0.60	3.36
0.62	3.36
0.64	3.36
0.66	3.37
0.68	3.37
0.70	3.37
0.72	3.37
0.74	3.37
0.76	3.38
0.78	3.38
0.80	3.38
0.82	3.39
0.84	3.39

0.26	3.31
0.28	3.32
0.30	3.32
0.32	3.33
0.34	3.33
0.36	3.33
0.38	3.34
0.40	3.34
0.42	3.34
0.44	3.34
0.46	3.34
0.48	3.34
0.50	3.35

0.86	3.40
0.88	3.40
0.90	3.41
0.92	3.41
0.94	3.43
0.96	3.47
0.98	3.61
1.00	3.80

Appendix C: Hysteresis Curve Data

SOC	Hysteresis Voltage
0.000	0.011
0.010	0.005
0.020	0.005
0.030	0.006
0.040	0.006
0.050	0.005
0.060	0.005
0.070	0.005
0.080	0.005
0.090	0.005
0.100	0.005
0.110	0.005
0.120	0.005
0.130	0.005
0.140	0.005
0.150	0.005
0.160	0.005
0.170	0.005

SOC	Hysteresis Voltage
0.310	0.005
0.320	0.005
0.330	0.005
0.340	0.005
0.350	0.005
0.360	0.005
0.370	0.005
0.380	0.005
0.390	0.005
0.400	0.005
0.410	0.005
0.420	0.005
0.430	0.005
0.440	0.005
0.450	0.005
0.460	0.005
0.470	0.005
0.480	0.005

SOC	Hysteresis Voltage
0.640	0.005
0.650	0.005
0.660	0.005
0.670	0.005
0.680	0.005
0.690	0.005
0.700	0.005
0.710	0.005
0.720	0.005
0.730	0.005
0.740	0.005
0.750	0.005
0.760	0.005
0.770	0.005
0.780	0.005
0.790	0.005
0.800	0.005
0.810	0.005

0.180	0.005
0.190	0.004
0.200	0.005
0.210	0.005
0.220	0.005
0.230	0.005
0.240	0.005
0.250	0.005
0.260	0.005
0.270	0.005
0.280	0.005
0.290	0.005
0.300	0.005

0.490	0.005
0.500	0.005
0.510	0.005
0.520	0.005
0.530	0.005
0.540	0.005
0.550	0.005
0.560	0.005
0.570	0.005
0.580	0.005
0.590	0.005
0.600	0.005
0.610	0.005
0.620	0.005
0.630	0.005

0.820	0.005
0.830	0.005
0.840	0.005
0.850	0.005
0.860	0.006
0.870	0.006
0.880	0.005
0.890	0.006
0.900	0.006
0.910	0.006
0.920	0.006
0.930	0.007
0.940	0.007
0.950	0.008
0.960	0.009
0.970	0.010
0.980	0.010
0.990	0.005
1.000	0.017

Appendix D: Vehicle Model

In order to approximate the battery current, a simple vehicle model was utilized to generate a power requirement over the FTP. The vehicle was a simple road load model with the following parameters:

Vehicle Parameters

F0	21	lbf	93.45	N
F1	0.36	lbf/mph	3.583893	N/(m/s)
F2	0.019	lbf/mph2	0.423154	N/(m/s)2
$mass_{veh}$	3750	lb	1704.545	Kg

The road load equation utilized was as follows:

$$F_{NET} = F_0 + F_1 \times v + F_2 v^2 + m_{veh} a$$

A 1Hz FTP was used to provide a speed trace. The tractive power required is then:

$$P = F_{NET} v$$

To model the power required through the one cell, the total tractive power was divided by 0.85, an estimated efficiency of an electric motor, inverter and battery. The final power was divided by 4, due to the 4 parallel strings of cells, in order to determine the final power requirement

Appendix E: Battery Model for Simulation

In order to simulate the current through the FTP, the power is fed into a PI controller that uses a voltage to determine a current. The current is then utilized to determine a voltage of the cell based on a voltage model and SOC from the perfect, coulomb counted battery model. The voltage is then multiplied by current to determine the delta of power.

The embedded Simulink PI controller was utilized and tuned by the embedded PI tuner. Below is the Simulink code for the simulation.

Gaussian Noise Addition Code

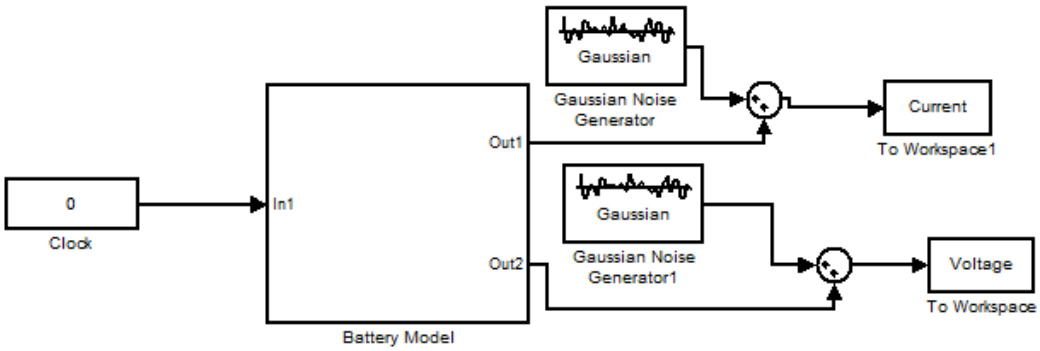

Battery Model

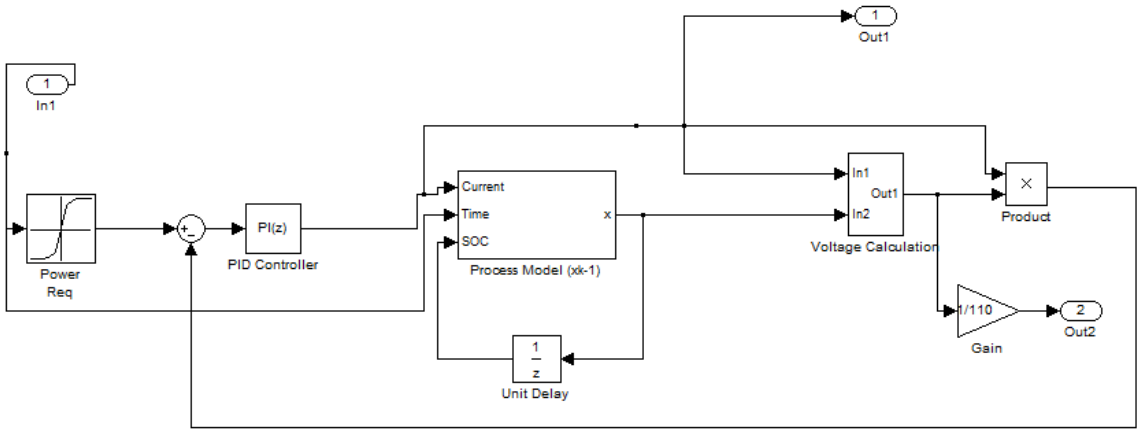
1
Out1
1
In1
Power
Req
PI(z)
PID Controller
Current
Time
SOC
x
Process Model (xk-1)
1
z
Unit Delay
In1
Out1
In2
Voltage Calculation
Product
1/110
Gain
2
Out2

References

[1] **Barusukov, Y.** *"Challenges and Solutions in Battery Fuel Gauging".* s.l. : http://focus.ti.com/lit/ml/slyp086/slyp086.pdf, 2004.

[2] **Plett, G.** *Extended Kalman filtering for battery management systems.* Colorado Springs, CO : Journal of Power Sources, 2004, Vol. 134, (277-292).

[3] **S. Pang, et al.** *Battery State-of-Charge Estimation*Arlington : Proceedings of the American Control Conference, 2001.

[4] **E. Tate, et al.** The Electrification of the Automobile: From Conventional Hybrid, to Plug-in Hybrids,to Extended-Range Electric Vehicles. s.l. : SAE World Congress, 2008. 2008-01-0458.

[5] **T. Markeol, et al.** *Plug-In Hybrid Vehicle Analysis.* Golden, CO : National Renewable Energy Laboratory, 2006. NREL/MP-540-40609.

[6] **P. Albertus, et al.** Experiments on and Modeling of Positive Electrodes with Multiple Active Materials for Lithium-Ion Batteries. *Journal of the Electrochemical Society.* 2009, Vol. 156, (A608-A618).

[7] **M. Alamgir, et al.** *Efficient Batteries for Transportation Applications.* Detroit : Society of Automotive Engineers - Convergence, 2008.

[8] **D. Vutetakis, et al.** *A Comparison of Lithium-Ion and Lead-Acid Aircraft Batteries.* Bellevue : Society of Automotive Engineers - Power Systems Conference, 2008. 2008-01-2875.

[9] **M. Kromer, et al.** *Electric Powertrains: Opportunities and Challenges in the US Light-Duty Vehicle Fleet.* Cambridge, MA : Sloan Automotive Laboratory, 2007. LFEE 2007-03 RP.

[10] **J. Axsen, et al.** *Batteries for Plug-in Hybrid Electric Vehicles (PHEVs): Goals and the State of Technology circa 2008.* Davis, Ca : Institute of Transportation Studies, Univeristy of California, 2008. UCD-ITS-RR-08-14.

[11] **A. Brooker, et al.** *Technology Improvement Pathways to Cost-Effective Vehicle Electrification.* s.l. : National Renewable Energy Laboratory, 2010. NREL/CP-540-47454.

[12] Testing and Measuring Emissions - Dynamometers Driving Aid. [Online] United States Environmental Protection Agency, 2010. http://www.epa.gov/nvfel/testing/dynamometer.htm.

[13] **Bureau of Transportation Statistics - US Department of Transportation** *Journal of Transportation and Statistics.* 2, Vol. 3. ISSN 1094-8848, (2-3).

[14] **Liaw, B.** From driving cycle analysis to understanding battery performance in real-life electric hybrid vehicle operation : Journal of Power Sources, 2007, Vol. 174, (76-88).

[15] **I. El-Shawarby, et al.** Comparative field evaluation of vehicle cruise speed and acceleration level impacts on hot stabilized emissions. Transportation Research Part D, 2005, Vol. 10, (13-30).

[16] **Holmen, B.** *Characterizing the Effects of Driver Variability on Real-World Vehicle Emissions.* s.l. : Institute of Transportation Studies - University of California, Davis, 1998.

[17] **E. Ericcson, et al.** Optimizing route choice for lowest fuel consumption – Potential effects of a new driver support tool. 14, 2006, Vol. Transportation Research Part C, (369-383).

[18] **Brundell-Freij, et al.** Influence of street characteristics, driver category and car performance on urban driving patterns. 10, 2005, Vol. Transportation Research Part D (213-229).

[19] **R. Langari, et al.***Integrated Drive Cycle Analysis for Fuzzy Logic Based Energy Management in Hybrid Vehicles.* s.l. : The IEEE International Conference on Fuzzy Systems, 2003. 0-7803-7810-5.

[20] **G. Sovran, et al.** Quantifying the Potential Impacts of Regenerative Braking on a Vehicle's Tractive-Fuel Consumption for the U.S., European, and Japanese Driving Schedules. Detroit, Mi : Society of Automotive Engineers International - World Congress, 2006. 2006-01-0664.

[21] **G. Sovran, et al.** *A Contribution to Understanding Automotive Fuel Economy and Its Limits.* Washington, DC : Society of Automotive Engineers International - Government/industry Meeting, 2003. 2003-01-2070.

[22] **C. Mendes** *Torque Control Strategies for AWD Electric Vehicles.* Waterloo, ON : University of Waterloo, 2006.

[23] **T. Grewe, et al.** *Defining the General Motors 2-Mode Transmission System.* Detroit : SAE International - World Congress, 2007. 2007-01-0273.

[24] **M. Duoba, et al.** *Test Procedure Development for "Blended Type" Plug-In Hybrid Vehicles.* Detroit, Mi : SAE International - World Congress, 2008. 2008-01-0457.

[25] **SAE International.** Surface Vehicle Recommended Practice for Measuring the Exhaust Emissions and Fuel Economy of Hybrid-Electric Vehicles, Including Plug-In Hybrid Vehicles. s.l. : SAE International, 2010. SAE J1711.

[26] **SAE International.** Utility Factor Definitions for Plug-In Hybrid Electric Vehicles Using 2001 U.S. DOT National Household Travel Survey Data. s.l. : SAE International, 2009. SAE J2841.

[27] **Woodbank Communications.** Battery and Energy Technologies. *Electropaedia.* [Online] 2005. [Cited: 08 20, 2010.] http://www.mpoweruk.com/.

[28] **F. Kalhammer, et al.** Status and Prospects for Zero Emissions Vehicle Technology Report of the ARB Independent Expert Panel 2007. Sacramento, Ca : s.n., 2007.

[29] **L. Le Guenne, et al.** *Life Duration of Ni-MH Cells for High Power Applications.* Bordeuax Cedex, France : Journal of Power Sources, 2002, Vol. 105 (134-138).

[30] **P. Albertus, et al.** *Modeling Side Reactions and Nonisothermal Effects in Nickel Metal-Hydride Batteries.* Berkeley, CA : Journal of the Electrochemical Society, 2008, Vol. 155 (A48-A60).

[31] **Snyder, K.** Hybrid Vehicle Battery Technology - The Transition from NiMH to Li-Ion. Detroit, Mi : SAE International, 2009. 2009-01-1385.

[32] **N. Nanbu, et al.** Electrochemical Properties of Fluoropropylene Carbonate and its Application to Lithium-Ion Batteries. s.l. : Electrochemistry Communications, 2008, Vol. 10, (783-786).

[33] **Wittingham, M.** *Lithium Batteries and Cathode Materials.* Binghampton, NY : Chemical Review, 2004, Vol. 104, (4271-4301).

[34] **S. Muto, et al.** *Capacity-Fading Mechanisms of LiNiO2-Based Lithium-Ion Batteries.* Nagoya, Japan : Journal of the Electrochemical Society, 2009, Vol. 156, (A371-A377).

[35] **J. James, et al.** State of Health Recognition for Aircraft Batteries Dynamic Equivalent Schematics and Prinicples Model Considerations. Bellevue, Washington : SAE International - Power Systems Conference, 2008. 2008-01-2933.

[36] **X. Zhang, et al.** Intercalation-Induced Stress and Heat Generation within Single Lithium-Ion Battery Cathode Particles. Ann Arbor, Mi : Journal of the Electrochemical Society, 2008, Vol. 155, (A542-A552).

[37] **M. Kerlau, et al.**Studies of Local Degradation Phenomena in Composite Cathodes for Lithium-Ion Batteries. Berkeley, CA : Electrochimica Acta, 2007, Vol. 52, (5422-5429).

[38] **Q. Zhang, et al.** *Capacity Fade Analysis of a Lithium Ion Cell.* Columbia, SC : Journal of Power Sources, 2008, Vol. 179, (793-798).

[39] **H. Jin, et al.** A Comparison Study of Capacity Degradation Mechanisms of LiFePO4 -based Lithium Ion Cells. Tianjin, China : Journal of Power Sources, 2009, Vol. 189, (445-448).

[40] **G. Ning, et al.** *A Generalized Cycle Life Model of Rechargeable Li-Ion Batteries.* Columbia, SC : Electrochemical Acta, 2006, Vol. 51 (2012-2022).

[41] **M.Tang, et al.** *Two-Dimensional Modeling of Lithium Deposition During Cell Charging.* Berkeley, CA : Journal of the Electrochemical Society, 2009, Vol. 156, (A390-A399).

[42] **P. Arora, et al.** *Capacity Fade Mechanisms and Side Reactions in Lithium-Ion Batteries.* Columbia, SC : Journal of the Electrochemical Society, 1998, Vol. 145, (3647-3667).

[43] **D. Aurbach, et al.** *An Analysis of Rechargeable Litium-Ion Batteries after Prolonged Cycling.* Ramat - Gan, Israel : Electrochemical Acta, 2002, Vol. 00 (1-13).

[44] **M. Stevens** Hybrid Fuel Cell Powertrain Development Considering Power Source Degradation. Waterloo, On : University of Waterloo, 2008.

[45] **D. Domenico, et al.** Lithium-Ion Battery State of Charge Estimation with a Kalman Filter Based on a Electrochemical Model. San Antonio, TX : 17th IEEE Conference on Control Applications, 2008.

[46] **E. Wilhelm, et al.** *Implementation and Optimization of a Fuel Cell Hybrid Powertrain.* Detroit, Mi : SAE International - World Congress, 2007. 2007-01-1069.

[47] **M.B. Stevens, et al.** *Fuel Cell Hybrid Control Strategy Development.* Detroit, Mi : SAE International - World Congress, 2006. 2006-01-0214.

[48] **S. Pillar, et al.** *Methods for State-of-Charge Determination and Their Applications.* Ulm, Germany : Journal of Power Sources, 2001, Vol. 96, (113-120).

[49] **G. Plett** Extended Kalman Filtering for Battery Management Systems of LiPB-Based HEV Battery Packs Part 2. Modeling and Identification. Colorado Springs, CO : Journal of Power Sources, 2004, Vol. 134, (262-276).

[50] **S. Rodrigues, et al.** A Review of State-of-Charge Indication of Batteries by Means of A.C. Impedance Measurements. s.l. : Journal of Power Sources, 2000, Vol. 87, (12-20).

[51] **N. Mellgren** *Impedance as a Tool for Investigating Aging in Lithium-Ion Porous Electrodes.* Stockholm, Sweden : Journal of the Electrochemical Society, 2008, Vol. 155, (A304-A319).

[52] **S. Lee, et al.** State-of-Charge and Capacity Estimation of Lithium Ion Battery Using a New Open-Circuit Voltage Versus State-of-Charge. s.l. : Journal of Power Sources, 2008, Vol. 185, (1367-1373).

[53] **D. Simon** *Optimal State Estimation.* Hoboken, NJ : John Wiley and Sons, 2006.

[54] **G. Plett** Extended Kalman Filtering for Battery Management Systems of LiPB-Based HEV Battery Packs Part 3. State and Parameter Estiamation. Colorado Springs, CO : Journal of Power Sources, 2004, Vol. 134, (277-292).

[55]**S. Pang, et al.** *Battery State-of-Charge Estimation.* Arlington, VA : American Control Conference, 2001.